Optical Properties of Semiconducting Nanowires

Lambert K. van Vugt PhD thesis 2007 Optical properties of semiconducting nanowires www.phys.uu.nl/~vugt

Cover Photograph: Coherent light emission from the end facets of a zinkoxides nanowire. Photograph taken by the author.

Printed by Universal Press, Veenendaal

CIP-GEGEVENS KONINKLIJKE BIBLIOTHEEK, DEN HAAG

Van Vugt, Lambert Karel
Optical properties of semiconducting nanowires
(Optische eigenschappen van halfgeleidende nanodraden)
Lambert Karel van Vugt, Utrecht: Universiteit Utrecht,
Condensed Matter and Interfaces, Debye Instituut.
Proefschrift Universiteit Utrecht. Met een samenvatting in het Nederlands
ISBN 978-90-9021628-7

Optical Properties of Semiconducting Nanowires

Optische Eigenschappen van Halfgeleidende Nanodraden

(met een samenvatting in het Nederlands)

Proefschrift

ter verkrijging van de graad van doctor aan de Universiteit Utrecht op gezag van de rector magnificus, prof. dr. W. H. Gispen, ingevolge het besluit van het college voor promoties in het openbaar te verdedigen op woensdag 28 maart 2007 des middags te 4.15 uur

door

Lambert Karel van Vugt

geboren op 6 september 1977, te Utrecht

Promotor: Prof. dr. D. Vanmaekelbergh

The work described in this thesis is part of the research programme of the 'Stichting voor Fundamenteel Onderzoek der Materie (FOM)', which is financially supported by the 'Nederlandse Organisatie voor Wetenschappelijk Onderzoek (NWO)'.

Contents

Chapter 1

Introduction

1.1 Nano science and technology

The integrated circuit technology of today is based on a top-down approach where elements such as interconnects and transistors are formed by optical lithography and the removal of material from large semiconductor crystals. The cost and size of the basic transistor switching element still continues to halve each two years as predicted by Moore in 1965.[1] The current transistor size of 65 nm is expected to have shrunk to 22 nm in 2011 just by incremental enhancements of the current technology.[2] It is anticipated that in 10 to 15 years time this production technology cannot be extended to smaller sizes due to basic physical limitations [2] A bottom-up approach of circuit assembly using atomic,[3] single molecule,[4] carbon nanotube,[5] quantum dot,[6] or nanowire [7] building blocks can be useful for complementary opto-electrical functions, but the same physical limitations will arise. For instance, the principle of doping of a semiconductor to alter its electronic properties that is one of the foundations of current semiconductor technology will no longer be applicable if the size of the nanostructure is so small that only a single dopant atom is required. The position of that dopant atom would become highly important as well as the ability to bring it there. In addition, smaller structures are more and more governed by quantum mechanics as opposed to classical mechanics and will behave differently, necessitating a different concept of computation. Another example is the relatively larger surface of smaller objects having a different electronic structure than the bulk material. The higher surface to volume ratio also leads to a higher sensitivity of the nanostructure to its surroundings which can be advantageous (sensors) or disadvantageous (electronic or photonic transport, light generation).

Whereas the ongoing miniaturization of conventional electron charge based circuitry probably does not need a bottom-up approach, new concepts for computation and circuit integration are also explored where a bottom-up approach might be useful. Circuits based on the electron spin (spintronics) as an additional degree of freedom are investigated [8] as well as optical computation [9] and quantum computation.[10] Other developments entail the further integration of optics and electronics. While optical computation still remains a futuristic proposition, optical interconnects are seen as a way to alleviate the heat dissipation problems of electronic interconnects which at the moment forms a bottleneck for higher operation speeds and higher component densities.[2] Aside from computing and routing, structures in the nanometer range are also promising in the fields

of chemical, biological and medical detection. Due to their large surface to volume ratio, the properties of nanostructures can be highly sensitive to changes at its surface. This property combined with nanoelectronics and for instance the use of nanofluidics [11] or nanomechanics (NEMS) [12] as a means of sampling can lead to small devices for the simultaneous detection of minute quantities of numerous compounds or agents. It is in these applications that bottom-up nanotechnology might prove itself competitive.

It is clear that the fields of nano science and technology are intimately related and that often a clear distinction cannot be made. Ample challenges arise which often require a multidisciplinary approach based on molecular or solid state chemistry, materials science and quantum physics.

1.2 Semiconducting nanowires

Semiconducting nanowires with diameters ranging from 1 to 400 nm and lengths of up to hundreds of micrometers are perhaps the most versatile building blocks for optical and (opto-)electronic circuits at the nanoscale. They can be grown on a surface from gas phase molecular precursors using Chemical Vapor Deposition (CVD), Molecular Beam Epitaxy (MBE) or the Vapor Liquid Solid (VLS) method (see chapter 3). In contrast to, for instance atoms, single molecules and nanoparticles, nanowires are easily contacted using standard equipment and compatibility with silicon or germanium technology has been demonstrated. [13-15] Unlike carbon nanotubes which have electronic properties depending on the difficult to control chirality of the tube,[16] the electronic properties of semiconducting nanowires can be controlled by choice of semiconductor,[17] doping,[18, 19] or variation of the diameter.[20] Alternatively, also ferromagnetic semiconducting nanowires could be obtained.[21] The use of semiconducting nanowires in electrical circuits ranges from transistor arrays,[22] single electron tunneling devices,[18] superconductivity[23, 24] and nonvolatile memory.[25] Optoelectrical nanodevices based on semiconducting nanowires include polarization dependent photodetectors,[26] light emitting diodes [27] and solar cells.[28] In addition, semiconductor nanowires can act as nanocavities for light resulting in optically or electrically driven nanolasers [29, 30] and subwavelength waveguiding of light over long distances and through sharp bends.[31, 32] An example of this waveguiding is shown in

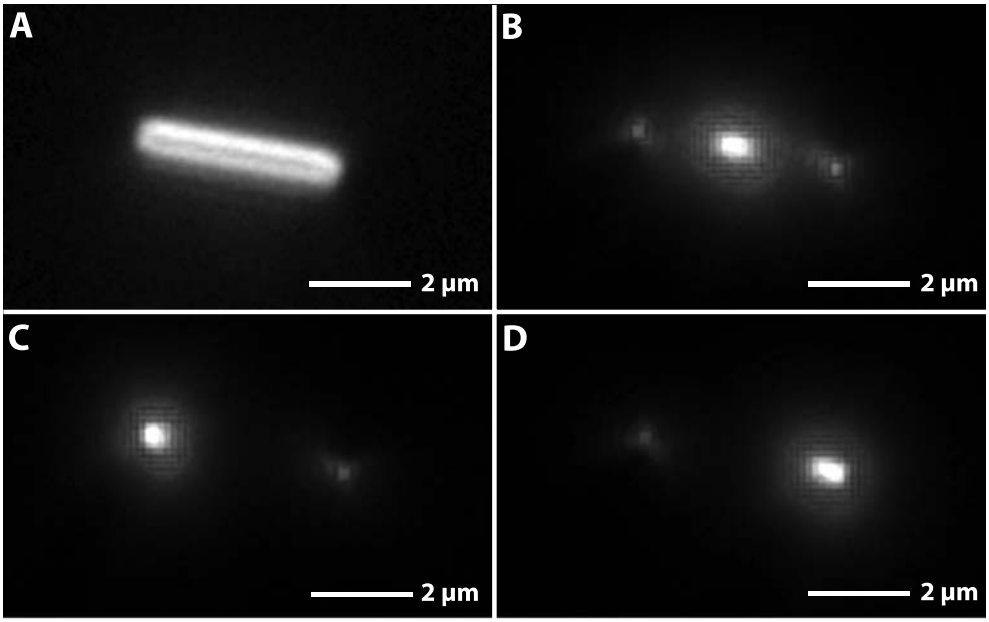

Figure 1.1(A) Darkfield optical microscope image of a 4 µm long ZnO nanowire. (B-D) Photoluminescence images of the same wire showing waveguiding. The exciting laserspot was located at (B) the middle of the wire, (C) the left end and (D) the right end.

figure 1. In figure 1A a darkfield optical microscope image of a ZnO nanowire is shown. This wire was subsequently illuminated by a small laser spot (∅ 800 nm, λ=349 nm) located at either the middle part (B), left end (C) or right end (D) of the wire (the laser light is filtered out). It can be seen that the light travels through the wire and emerges at the ends. Recently semiconducting nanowires could be used as electrical or optical sensors using either a change of conductance or a change of absorption of the evanescent field of light traveling through the wire upon the binding of a substance (single virus) at the nanowire surface.[22, 33, 34]

The devices mentioned above are all "proof of principle" devices which cannot directly compete with the current top-down technology due to excessive production time and cost. The main challenges for the industrial use of semiconducting nanowires in (opto-)electronic circuitry lie in the fields of the manipulation, positioning and processing of large quantities of nanowires as well as the precise control over the diameter and the impurity doping level. Additionally, cheap and reliable methods of individually contacting large numbers of nanowires would have to be developed to gain any benefit from the diminutive size. While

semiconducting nanowires may not be able to directly compete in the relentless reduction of transistor size there may be certain "niches" were semiconducting nanowires due to their specific properties could be utilized, for instance in sensing applications, in optics at the nanoscale and in novel concepts of computing.

1.3 Outline of this thesis

In this thesis the optical properties of nanowires made from the semiconductors InP and ZnO are studied. InP is a small bandgap semiconductor (1.35 eV at room temperature) which due to its high electron mobility is interesting for high speed optoelectrical applications in the near IR wavelength area (920 nm). ZnO is a wide bandgap semiconductor (3.37 eV at room temperature) emitting in the UV (380 nm) and green (535nm) spectral regions and is interesting for lasing in the UV and blue spectral regions as well as for white light applications. Before results are presented in chapters 3-6, chapter 2 will give a theoretical background of light-matter interaction in three dimensionally optically confined systems. Chapter 3 describes the synthesis and characterization of semiconducting nanowires of InP and ZnO. The lengths of the wires are typically 1 to 20 μm with the diameter of the InP wires typically in the 40-80 nm range an the diameter of the ZnO wires typically in the 80-300 nm range. These wire dimensions exclude any measurable electron confinement effects in the wires but rather allow for photon confinement. In addition it is shown that ZnO nanowires can be doped using a simple and generally applicable technique.

The as-grown InP nanowires exhibit a low photoluminescence quantum yield which has to be improved in order to use these wires in devices and fundamental studies. In chapter 4 results are presented on the photoetching and passivation of InP nanowires resulting in polarization sensitive photoetching and increased photoluminescence yields. Chapter 5 presents results of spatially and spectrally resolved measurements on ZnO nanowires. By scanning a photon or electron excitation beam over a wire and recording the spectrally resolved response at each position of the excitation spot, signatures of exciton-polaritons could be detected. These composite particles consist partially of light (photon) and matter (exciton) and should be taken into account for future nanophotonic circuitry. Finally in chapter 6 at higher excitation intensities laser emission as evidenced by sharp peaks at energetic positions determined by length of the nanocavity is

observed. An intricate interference pattern is observed from these lasing ZnO nanowires. It is shown that these patterns are the result of spherical emission of phase correlated light at both ends of the nanowire.

References

1 G. E. Moore, Cramming more components onto integrated circuits, *Electron. Lett.* **38** (1965).
2 C. R. Barret, The digital evolution, *MRS Bulletin* **31** (2006), p. 906-913.
3 H. Sellier, G. P. Lansbergen, J. Caro, S. Rogge, N. Collaert, I. Ferain, M. Jurczak, and S. Biesemans, Transport Spectroscopy of a Single Dopant in a Gated Silicon Nanowire, *Phys. Rev. Lett.* **97** (2006), p. 206805.
4 P. G. Piva, G. A. DiLabio, J. L. Pitters, J. Zikovsky, M. Rezeq, S. Dogel, W. A. Hofer, and R. A. Wolkow, Field regulation of single-molecule conductivity by a charged surface atom, *Nature* **435** (2005), p. 658-661.
5 A. Bachtold, P. Hadley, T. Nakanishi, and C. Dekker, Logic Circuits with Carbon Nanotube Transistors, *Science* **294** (2001), p. 1317-1320.
6 D. L. Klein, R. Roth, A. K. L. Lim, and A. P. A. L. McEuen, A single-electron transistor made from a cadmium selenide nanocrystal, *Nature* **389** (1997), p. 699 - 701.
7 Y. Huang, X. Duan, Y. Cui, L. J. L.-H. Kim, and C. M. Lieber, Logic Gates and Computation from Assembled Nanowire Building Blocks, *Science* **294** (2001), p. 1313-1317.
8 S. A. Wolf, D. D. Awschalom, R. A. Buhrman, J. M. Daughton, S. v. Molnár, M. L. Roukes, A. Y. Chtchelkanova, and D. M. Treger, Spintronics: A Spin-Based Electronics Vision for the Future, *Science* **294** (2001), p. 1488-1495.
9 K.-H. Brenner, Digital Optical Computing, *Aplied Physics B* **46** (1988), p. 111-120.
10 D. P. DiVincenzo, Quantum Computation, *Science* **270** (1995), p. 255-261.
11 D. Mijatovic, J. C. T. Eijkel, and A. v. d. Berg, Technologies for nanofluidic systems: top-down vs. bottom-up - a review, *Lab on a chip* **5** (2005), p. 492-500.
12 R. H. Blick and M. Grifoni, Focus on Nano-electromechanical Systems, *New journal of Physics* **7** (2005).
13 E. P. A. M. Bakkers, J. A. v. Dam, S. D. Franceschi, L. P. Kouwenhoven, M. Kaiser, M. Verheijen, H. Wondergem, and P. V. D. Sluis, Epitaxial growth of InP nanowires on germanium, *Nature Materials* **3** (2004), p. 769-773.
14 A. L. Roest, M. A. Verheijen, O. Wunnicke, S. Serafin, H. Wondergem, and E. P. A. M. Bakkers, Position-controlled epitaxial III–V nanowires on silicon, *Nanotechnology* **17** (2006), p. S271-S275.
15 T. Martensson, C. P. T. Svensson, B. A. Wacaser, M. W. Larsson, W. Seifert, K. Deppert, A. Gustafsson, L. R. Wallenberg, and L. Samuelson, Epitaxial III-V Nanowires on Silicon, *Nanoletters* **4** (2004), p. 1987-1990.
16 D. Appell, Nanotechnology: Wired for success, *Nature* **419** (2002), p. 553-555.
17 X. Duan and C. M. Lieber, General Synthesis of Compound Semiconductor Nanowires, *Adv. Mater.* **12** (2000), p. 298-302.
18 S. D. Franceschi, J. A. v. Dam, E. P. A. M. Bakkers, L. F. Feiner, L. Gurevich, and L. P. Kouwenhoven, Single-electron tunneling in InP nanowires, *Appl. Phys. Lett.* **83** (2003), p. 344-347.
19 X. Duan, Y. Huang, Y. Cui, J. Wang, and C. M. Lieber, Indium phosphide nanowires as building blocks for nanoscaleelectronic and optoelectronic devices, *Nature* **409** (2001), p. 66-69.
20 M. S. Gudiksen, J. Wang, and C. M. Lieber, Size-Dependent Photoluminescence from Single Indium Phosphide Nanowires, *J. Phys. Chem. B* **106** (2002), p. 4036-4039.
21 Y. Q. Chang, D. B. Wang, X. H. Luo, X. Y. Xu, X. H. Chen, L. Li, C. P. Chen, R. M. Wang, J. Xu, and D. P. Yua, Synthesis, optical, and magnetic properties of diluted magnetic semiconductor Zn1À xMnxO nanowires via vapor phase growth, *Appl. Phys. Lett.* **83** (2003), p. 4020-4022.

[22] F. Patolsky, B. P. Timko, G. Yu, Y. Fang, A. B. Greytak, G. Zheng, and C. M. Lieber, Detection, Stimulation, and Inhibition of Neuronal Signals with High-Density Nanowire Transistor Arrays, *Science* **313** (2006), p. 1100-1104.
[23] Y.-J. Doh, J. A. v. Dam, A. L. Roest, E. P. A. M. Bakkers, L. P. Kouwenhoven, and S. D. Franceschi, Tunable Supercurrent Through Semiconductor Nanowires, **309** (2005), p. 272-275.
[24] J. A. v. Dam, Y. V. Nazarov, E. P. A. M. Bakkers, S. D. Franceschi, and L. P. Kouwenhoven, Supercurrent reversal in quantum dots, *Nature* **442** (2006), p. 667-670.
[25] X. Duan, Y. Huang, and C. M. Lieber, Nonvolatile Memory and Programmable Logic from Molecule-Gated Nanowires, *Nanoletters* **2** (2002), p. 487-490.
[26] J. Wang, M. S. Gudiksen, X. Duan, Y. Cui, and C. M. Lieber, Highly Polarized Photoluminescence and Photodetection from Single Indium Phosphide Nanowires, *Science* **293** (2001), p. 1455-1457.
[27] M. S. Gudiksen, L. J. Lauhon, J. Wang, D. C. Smith, and C. M. Lieber, Growth of nanowire superlattice structures for nanoscale photonics and electronics, *Nature* **415** (2002), p. 617-620.
[28] M. Law, L. E. Greene, J. C. Johnson, R. Saykally, and P. Yang, Nanowire dye-sensitized solar cells, *Nature materials* **455-459** (2005), p. 452.
[29] M. H. Huang, S. Mao, H. Feick, H. Yan, Y. Wu, H. Kind, E. Weber, R. Russo, and P. Yang, Room-Temperature Ultraviolet Nanowire Nanolasers, *Science* **292** (2001), p. 1897-1899.
[30] X. Duan, Y. Huang, R. Agarwal, and C. M. Lieber, Single-nanowire electrically driven lasers, *Nature* **421** (2003), p. 241-245.
[31] M. Law, D. J. Sirbuly, J. C. Johnson, J. Goldberger, R. J. Saykally, and P. Yang, Nanoribbon Waveguides for Subwavelength Photonics Integration, *Science* **305** (2004), p. 1269-1273.
[32] C. J. Barrelet, A. B. Greytak, and C. M. Lieber, Nanowire Photonic Circuit Elements, *Nanoletters* **4** (2004), p. 1981-1985.
[33] F. Patolsky, G. Zheng, O. Hayden, M. Lakadamyali, X. Zhuang, and C. M. Lieber, Electrical detection of single viruses, *Proc. Natl. Acad. Sci. U. S. A.* **101** (2004), p. 14017-14022.
[34] D. J. Sirbuly, A. Tao, M. Law, R. Fan, and P. Yang, Multifunctional Nanowire Evanescent Wave Optical Sensors, *Adv. Mater.* **online early view** (2007).

Chapter 2

Theoretical concepts

21 Introduction

In this chapter a theoretical background will be given with the focus on light-matter conversion and interaction since this forms a key aspect to understanding the optical properties of ZnO nanowires discussed in chapters 5 and 6. First, the properties of excitons will be discussed. Then we will proceed with light-matter coupling in unconfined systems (exciton-polaritons) and extend this for systems in which the photons are confined (cavity-polaritons). Finally a section of this chapter will be dedicated to polariton cooling and lasing, phenomena that are anticipated to occur inside microcavities.

22 Excitons in semiconductor crystals

Upon absorption of a light quantum in a semiconductor an electron is promoted from the valence band to the conduction band. These charge carriers with opposite charges experience a coulombic attraction which can keep them together. Thus, the combination of the excited electron and its hole can be considered as a neutral quasiparticle; the exciton. The exciton concept was first put forward by Frenkel in 1931.[1] In most organic materials the exciton is highly localized giving rise to a Frenkel exciton. In semiconductors however, the exciton wave functions can spread over multiple unit cells and the exciton is called a Wannier exciton. Close to the critical points ($(\partial E/\partial \mathbf{K}) = 0$) of the energy bands of a direct semiconductor, the energy of an electron or a hole can be approximated by a quadratic dependence on the wavector. Taking into account the Coulomb interaction between the electron and hole and the exciton dispersion, the energy of an exciton can be written as:

$$E_{ex}(n,\mathbf{K}) = E_g - \frac{e^4\mu}{32\pi^2\hbar^2{\varepsilon_0}^2\varepsilon^2}\cdot\frac{1}{n^2} + \frac{\hbar^2\mathbf{K}^2}{2M} \qquad (1a)$$

$$\frac{1}{\mu} = \frac{1}{m_e} + \frac{1}{m_h} \qquad (1b)$$

$$M = m_e + m_h \qquad (1c)$$

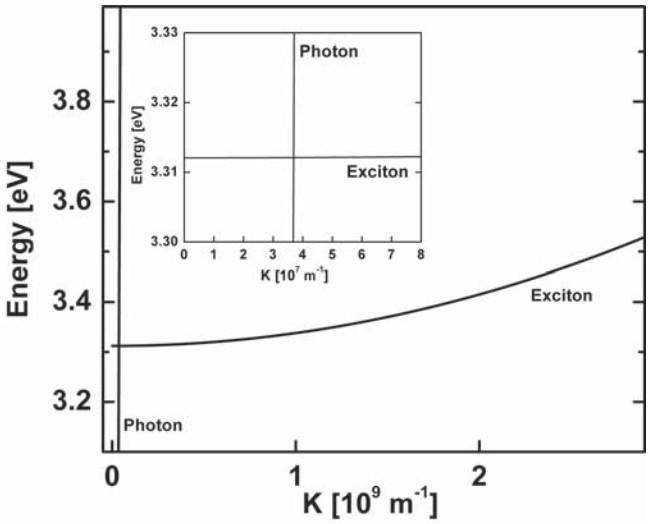

Figure 2.1 Parabolic exciton dispersion for an exciton in ZnO. As a reference the photon dispersion is shown for a material with refractive index 2.2. Inset: In the wavevector region close to the crossing the exciton shows no dispersion.

where μ is the reduced mass, n is the principal quantum number, $\mathbf{K}$ is the combined electron and hole wavevector and M is the sum of the electron (m_e) and hole masses (m_h). The last term of eq. (1a) describes the translational energy of the exciton center of mass while the second term gives the exciton binding energy for the n^{th} excited state. The exciton-binding energy determines at which temperature the exciton is stable. For $k_B T$ comparable or bigger than the exciton binding energy, the exciton dissociates to a free electron and hole. Figure 2.1 shows the parabolic dispersion of an exciton in the semiconductor ZnO with as a reference the light dispersion in a material with an energy independent refractive index of 2.2 (nearly vertical line). In the inset it can be seen that in the range of optical wave vectors, the dispersion of the exciton can be neglected.

23 Exciton-Polaritons

A landmark paper by Hopfield in 1958 predicted that in the interaction of light with matter two regimes should be distinguished[2] : In the weak coupling regime a photon can be absorbed by an electronic transition. Subsequently the excited electron can recombine with a hole and irreversibly emit a photon into the electromagnetic continuum. This photon can then be absorbed by another electronic transition in a different location in the crystal and so on. In this way the photon and the resonance become

coupled but the photon and resonances states themselves remain unchanged. This description is known as the semi-classical theory or pertubative approach of absorption and emission of light and is described by Fermi's golden rule.[3] In the strong coupling regime, however, one cannot make the distinction anymore between a quantum of the electromagnetic wave and the electronic resonance if they are very close in energy. The two states are so strongly coupled that the excited resonance does not irreversibly loose its energy to the electromagnetic continuum. Instead, the energy oscillates back and forth between the photon and the resonance state indefinitely until this coherent state is destroyed by scattering. Only then has an absorption event happened. The composite exciton-photon quasiparticles (or alternatively the coherent state oscillating between the photon and exciton limiting states) were called exciton-polaritons. The original paper was applicable only for isotropic crystals but the theory was later extended to anisotropic crystals [4] and was validated by experiments.[5] Depending on the nature of the interacting excitations also phonon-polaritons in the IR and surface plasmon polaritons in the visible/IR spectral regions exist. The dispersion relation of exciton-polaritons can be calculated by either a microscopic quantum mechanical approach based on the construction of a Hamiltonian for the new composite particles or a classical macroscopic approach using the Maxwell relations.[2] The latter approach will be described here.[3] For simplicity a non-magnetic semiconductor (magnetization density of the medium $\mathbf{M}$=0) with a low carrier density (electrical current density $\mathbf{j}$=0) is assumed. Using the material equations for the electric displacement $\mathbf{D}$ and the magnetic induction $\mathbf{B}$:

$$\mathbf{D} = \varepsilon_0 \mathbf{E} + \mathbf{P} = \varepsilon\varepsilon_0 \mathbf{E} \qquad (2) \qquad \mathbf{B} = \mu_0 \mathbf{H} \qquad (3)$$

Faraday's law of induction and Ampere's-Maxwells law:

$$\nabla \times \mathbf{E} = -\frac{\partial \mathbf{B}}{\partial t} \qquad (4) \qquad \nabla \times \mathbf{H} = \frac{\partial \mathbf{D}}{\partial t} \qquad (5)$$

Can with (2) and (3) be written as:

$$\nabla \times \mathbf{E} = -\mu_0 \frac{\partial \mathbf{H}}{\partial t} \qquad (6) \qquad \nabla \times \mathbf{H} = \varepsilon_0 \frac{\partial \mathbf{E}}{\partial t} + \frac{\partial \mathbf{P}}{\partial t} \qquad (7)$$

Differentiating eq. (6) to x,y and z and differentiating eq. (7) to *t* leads to:

$$\nabla \times (\nabla \times \mathbf{E}) = -\mu_0 \nabla \times \frac{\partial \mathbf{H}}{\partial t} \qquad (8) \qquad \nabla \times \frac{\partial \mathbf{H}}{\partial t} = \varepsilon_0 \frac{\partial^2 \mathbf{E}}{\partial^2 t} + \frac{\partial^2 \mathbf{P}}{\partial^2 t} \qquad (9)$$

Using $\nabla \times (\nabla \times \mathbf{E}) = \nabla(\nabla \mathbf{E}) - \nabla^2 \mathbf{E}$ and $\nabla \mathbf{E} = 0$, combining eqs. (8) and (9) gives:

$$\nabla^2 \mathbf{E} - \mu_0 \varepsilon_0 \frac{\partial^2 \mathbf{E}}{\partial^2 t} = \mu_0 \frac{\partial^2 \mathbf{P}}{\partial^2 t} \qquad (10)$$

Now interaction of light with isotropic matter is introduced with the assumption that the induced polarization is a linear function of the electric field (i.e. linear optics):

$$\mathbf{P} = \varepsilon_0 [\varepsilon(\omega) - 1]\mathbf{E} = \varepsilon_0 \chi^{(1)} \mathbf{E} \quad (\varepsilon(\omega) \neq 1) \qquad (11)$$

Where $\chi^{(1)}$ is the linear susceptibility. Substitution of Eq. 11 into Eq. 10 leads to the wave equation for light in non-magnetic matter with a low carrier density:

$$\nabla^2 \mathbf{E} - \mu_0 \varepsilon_0 \varepsilon(\omega) \frac{\partial^2 \mathbf{E}}{\partial^2 t} = 0 \qquad (12)$$

Just as in the case of light in vacuum, solutions of eq. 12 are harmonic plane waves:

$$\mathbf{E} = \mathbf{E}_0 e^{i(\mathbf{kr} - \omega t)} \qquad (13)$$

Substituting eq. 13 into eq. 12 gives the relation between the wavevector and the frequency for light in a isotropic nonmagnetic, undoped semiconductor with (complex) dielectric function $\varepsilon(\omega, \mathbf{k})$.

$$\frac{c^2 \mathbf{k}^2}{\omega^2} = \varepsilon(\omega, \mathbf{k}) \qquad (14)$$

Equation 14 is also known as the polariton equation.[6] One can see that the relation between the wavector and the frequency for light in matter is

markedly different than the c=(ω/**k**) relation encountered for a photon in vacuum; it is determined by the dielectric function $\varepsilon(\omega)$, to be specified with a physical model. From eq. 14 we can sketch the shape of the polariton dispersion curve but in order to obtain realistic values for **k** and ω we need to know the dielectric function $\varepsilon(\omega)$. It can be shown that in a damped Lorentz oscillator model the dielectric function in the vicinity of a single electronic resonance is given by: [3, 6-8]

$$\varepsilon(\omega) = \varepsilon_b \left(1 + \frac{Ne^2}{\varepsilon_b m_e} \frac{f}{\omega_0^2 - \omega^2 - i\omega\gamma} \right) \qquad (15)$$

with ω_0 the resonance frequency, ε_b the background dielectric constant, γ the damping constant, N the number of atomic oscillators per unit volume and f the oscillator strength. The oscillator strength is a dimensionless quantity ranging from 0 to 1 which gives the intensity of a transition from an initial state i to a final state j relative to the summed intensity of all the possible transitions from that initial state.[9] It is related to the quantum mechanical transition probability (for one such a transition) by: [8, 9]

$$f_{ji} = \frac{2m_e\omega}{\hbar} \left\langle \Psi_j \left| e \cdot \mathbf{r} \right| \Psi_i \right\rangle^2 \qquad (16)$$

with the dipole operator $e\cdot\mathbf{r}$, initial wavefunction i and final wavefunction j. It would however be more convenient to express the oscillator strength in terms of an experimentally accessible quantity. The dielectric function $\varepsilon(\omega)$ in the vicinity of a resonance can be determined from reflection measurements.[10, 11] The transverse resonance frequency is defined as the frequency where the dielectric function asymptotically approaches infinity ($\varepsilon(\omega)\rightarrow\infty$) indicating the resonance frequency ω_0. [3] The longitudinal resonance frequency is defined as the frequency where $\varepsilon(\omega)=0$.[3] Between the transverse and longitudinal frequencies, $\varepsilon(\omega)$ is negative, indicative for absorption. By substituting $\varepsilon(\omega)\rightarrow\infty=\varepsilon(\omega_T)=\varepsilon(\omega_0)$ and $\varepsilon(\omega)=0=\varepsilon(\omega_L)$ into eq. 15 and assuming vanishing damping ($\gamma\rightarrow 0$) an expression of the oscillator strength in terms of the transverse and longitudinal resonance frequencies is obtained:

$$f \frac{Ne^2}{\varepsilon_b m_e} = \omega_L^2 - \omega_T^2 \qquad (17)$$

Despite this direct relation one often ends up with unphysical values of f >1 for measured longitudinal-transverse splittings and known density of oscillators N. Oscillator strength enhancement factors of up to 10^4 have been observed. [12] These "giant" oscillator strengths can be the result of two distinct mechanisms.[13] First, if a large number of n coherent excitons are created by a coherent excitation source such as a laser beam, their oscillator strengths can be added and the radiated power is proportional to n^2 (superradiance) in stead of n. This induced giant oscillator strength is however not expected to influence the observed longitudinal-transverse splitting in reflection measurements, due to the incoherent light source used. In contrast, measurements involving laser or electron beam excitation could very well show oscillator strength enhancement due to this ensemble coherence effect. The second origin of giant oscillator strength is due to the translational periodicity of the crystal lattice which allows a bound exciton to delocalize over an ensemble of atoms. [12, 14] In nanocrystals of semiconductors in the weak confinement regime (i.e. light wavelength>>nanocrystal radius>>exciton Bohr radius) it is frequently observed that the oscillator strength increases with the size of the system up to a diameter of ~60 nm (for ZnO) after which it decreases again [15, 16]. It is thought that the exciton wavefunction coherently fills the nanoparticle until scattering limits the maximum exciton coherence volume. In this way, a single exciton can absorb and radiate light as if it were a coherent array of n atomic sites (radiated power proportional to n^2).

From the above it is clear that for a semiconductor nanostructure the oscillator strength depends, besides on the nature of the semiconductor and the optical transition, also on the nanostructure size and the means of excitation. Furthermore, there is a large uncertainty in the actual number of oscillators in the coherent volume, their individual oscillator strengths and the exciton coherence volume. Therefore we will use for our purposes the experimentally observed longitudinal-transverse splitting as a measure of effective oscillator strength.

Substituting eq. (15) in eq. (14) and using eq. (17), gives the polariton dispersion relation in the vicinity of a single resonance without spatial dispersion:

$$\omega(\mathbf{k}) = \sqrt{\frac{\varepsilon_b\left(1+\frac{\omega_L^2-\omega_T^2}{\omega_T^2-\omega^2-i\omega\gamma}\right)}{c^2\mathbf{k}^2}} \qquad (18)$$

Any dispersion of the exciton resonances is neglected in eq. 18 which is justified by the negligible slope in the crossing region with photons (also see fig. 2.1). Plots of the real and imaginary parts of equation 18 for increasing light-matter coupling ($\hbar(\omega_L-\omega_T)$,see eq. 17) and zero damping can be seen in figure 2.2. With no coupling strength the photon state (black line) remains unperturbed and crosses the exciton dispersion (black dotted line). The imaginary wavevector is a delta function which peaks at the transverse exciton energy, indicating strong absorption only at the transverse exciton energy. With the introduction of a finite oscillator strength (0.5 meV, red line) the exciton and photon dispersions display an avoided crossing: an upper polariton branch (UPB) and an lower polariton branch (LPB) are formed. The UPB exists at the longitudinal exciton and higher energies. The LPB exists for energies lower than the transverse exciton energy. In between the longitudinal and transverse exciton energies there exists a forbidden energy gap in which no propagation is possible. In addition it can be seen from the imaginary wavevector that there is also strong damping and absorption in this energy range. The energy separation between the UPB and the LPB at the crossing wavevector gives the frequency with which energy oscillates back and forth between the photon and exciton states. This frequency is also known as the Rabi frequency. [17, 18] With increasing oscillator strength the avoided crossing widens. The Rabi

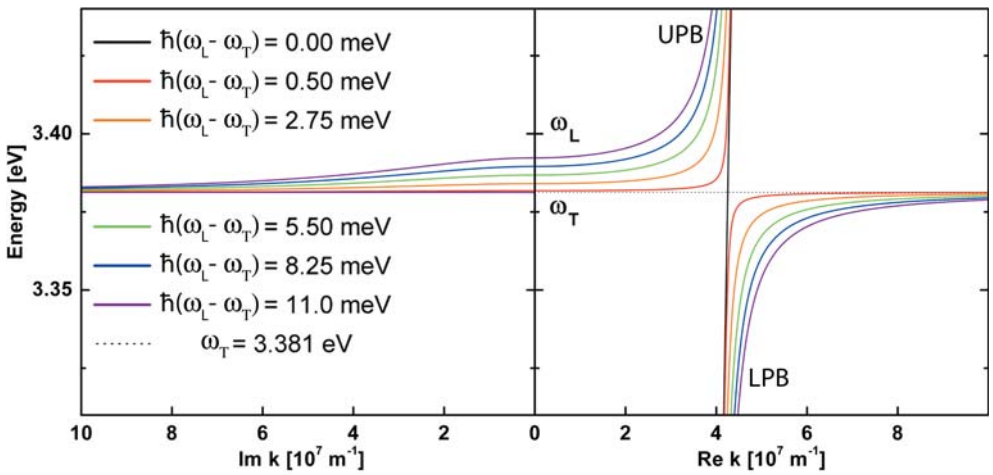

Figure 2.2 Influence of the longitudonal-transverse splitting on the polariton dispersion (eq. 18). With increasing splitting a forbidden energy range between the transverse and longitudonal exciton energies opens in which polaritons do not propagate and are strongly absorbed.

frequency is proportional to the oscillator strength or the oscillator density.[19]

Another important parameter for the polariton dispersion is the damping constant γ. Figure 2.3 illustrates the effect of finite damping on the polariton dispersion. While with zero damping there are no propagating modes between the longitudinal and transverse energies, a finite damping introduces propagating modes in the forbidden energy gap. These modes are however strongly damped due to the large imaginary part of the wavevector. In addition the LPB does not reach to infinite wavevector anymore. With increasing damping the UPB does not reach to **k**=0 anymore and the imaginary part broadens thus damping polaritons in a broader energy range. For the highest damping depicted (γ =10*($\omega_L - \omega_T$) the polariton dispersion resembles the photon dispersion albeit with a different slope.

From the preceding it follows that the ground state energy of the exciton-polariton is at zero energy, zero **k**. An excited exciton-polariton would quickly relax by optical and acoustical phonon emission, polariton scattering and electron-polariton scattering to this ground state without escaping the crystal as light. This quick relaxation however does not happen due to the so-called relaxation (thermalization) bottleneck.[3, 20, 21] It is clear that depending on the wavevector and energy, the exciton-polariton

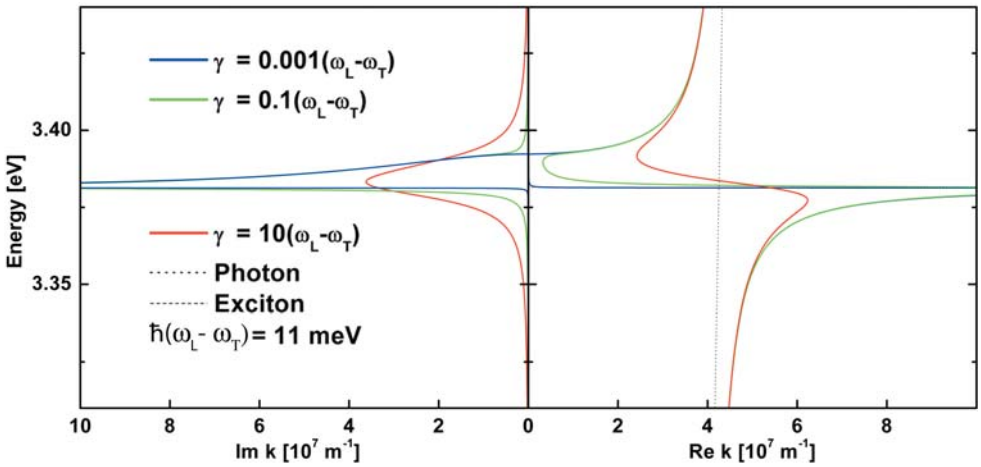

Figure 2.3 Influence of damping on the polariton dispersion (eq. 18). With increasing damping polariton propagation becomes possible in the region between the longitudonal and transverse energies. In addition the polariton dispersion does not reach to k=0 anymore. With increasing damping the imagenary wavevector broadens.

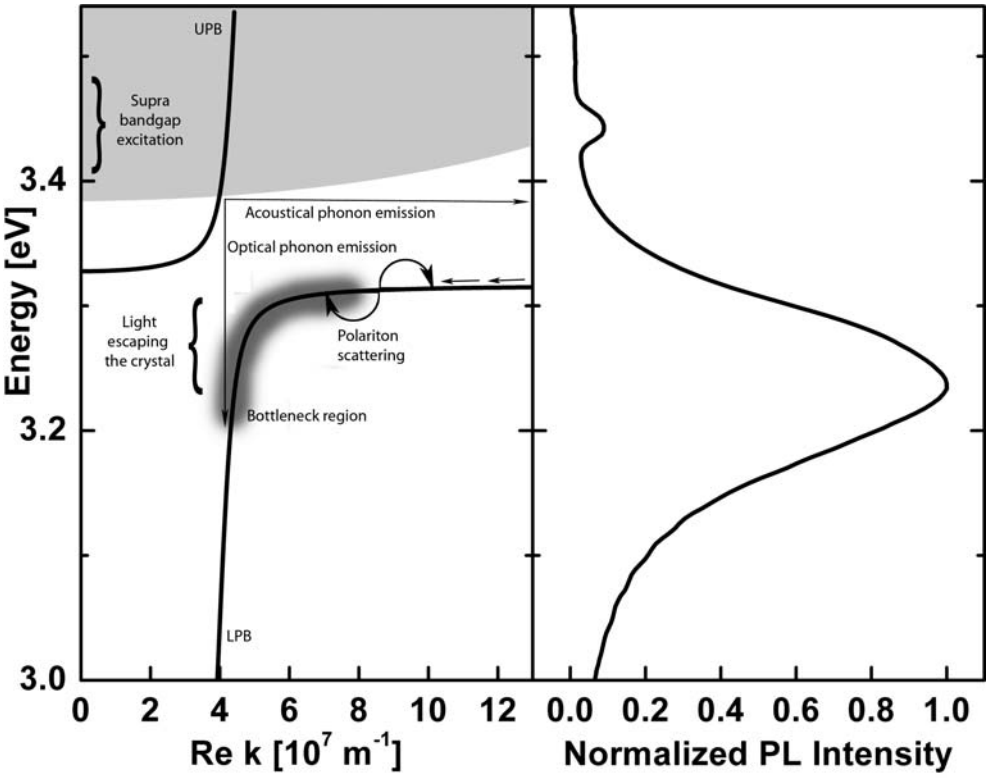

Figure 2.4 (left) Bottleneck in the relaxation of exciton-polaritons. After supra- bandgap excitation, the polaritons can relax by emission of optical or acoustic phonons, scattering amongst themshelves or scattering with electrons. In the shaded region of the lower branch this relaxation becomes slower due to a decrease in the density of states. At the same time the now photonic polaritons can more easily travel to the crystal surface and escape. Hence most polariton emission is to be expected in the indicated energy region. (right) Photoluminescence spectrum of a single ZnO nanowire showing emission at the energies corresponding to the exciton-polariton bottleneck region. The small peak at higher energy is caused by second harmonic generation from the fundamental beam (energy = 1.72 eV). (See chapter 5).

can be more excitonic or more photonic. In the crossover region, the density of states changes from a high exciton density of states to a low photon density of states. This causes an attenuation of the relaxation process. Furthermore, the group velocity and the mean free path of the photonic part of the polariton are much bigger then that of the excitonic part. Thus, the photonic polaritons can escape the crystal much easier. These two effects together are the cause that the majority of emissions take place just below the transverse exciton energy.

2.4 Confined photon modes in nanostructures

The nanowires studied in this thesis typically have diameters which are minimally three times bigger than the exciton Bohr radius (InP 20 nm and ZnO 1.5 nm). Therefore electron and hole confinement in these structures can be neglected at room temperature. In contrast, for photons the structures are smaller than the wavelength emitted by exciton (-polariton) decay allowing for strong optical confinement effects. Figure 2.5 A shows the structure under consideration: a square box of higher refractive index than its surroundings with sides of length L_x=L_y and L_z. Sides L_x and L_y typically have a length of 60-300 nm while the length L_z is typically 1-20μm. The photon confinement arises due to the large refractive index contrast between the semiconductor and its surroundings (air, glass). This structure is very similar to a so-called photonic wire. [22] This is a laterally confined microcavity (Fig 2.5B) where distributed Bragg mirrors (DBR's) confine the optical field in the z-direction and the refractive index contrast in the lateral directions. In the limit of L_z=L_y=$L_x \approx \lambda$ this structure becomes a photonic dot which allows only a single mode to exist. [23] It has been shown that in photonic wires and dots the strongly confined photon modes obey the following dispersion relation: [22-24]

$$E(\mathbf{k}) = \frac{\hbar c}{\sqrt{\varepsilon_b}} \sqrt{\mathbf{k}_x^2 + \mathbf{k}_y^2 + \mathbf{k}_z^2} \qquad (19)$$

The wavevectors are quantized due to the dimensions according to:

$$\mathbf{k}_{x,y,z} = m_{x,y,z} \frac{\pi}{L_{x,y,z}} \qquad (20)$$

where $m_{x,y,z}$=1,2,3, … is the mode number (number of half wavelengths) for the x, y and z directions.

In figure 2.5 B the photonic modes in the optical energy region of interest are shown of a photonic wire with L_x =L_y=270 nm for m_x and m_y <4. As a reference also the dispersion of an unconfined photon is shown (black line). It can be seen that lateral photon confinement causes the photon dispersion to shift to lower wavevector values and causes a lower, non constant, slope. Starting from the m_x =2 m_y=2 mode a cutoff appears below

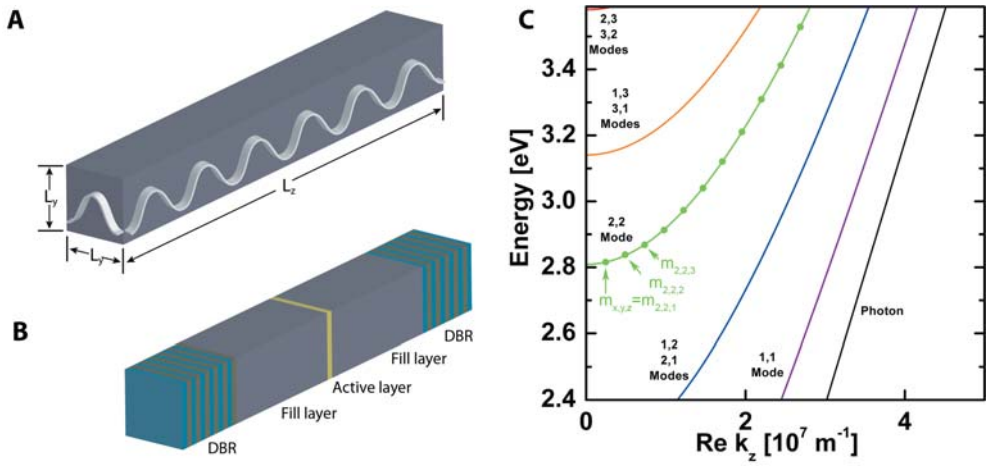

Figure 2.5 (A) Geometry of the considered structure. (B) This structure is reminescent of a laterally confined microcavity in which the lateral confinement is caused by the refractive index contrast with the surroundings and the longitudonal confinement is caused by Distributed Bragg Reflectors (DBR). (C) Dispersion of laterally confined photon modes. The index denotes the modenumber in the x and y directions respectively. The confinement causes an cutoff energy below which the mode is purely imaginairy.

which the mode is purely imaginary. Reducing the lateral sizes has the effect of shifting the modes up in energy until no strongly confined mode exist anymore in the optical energy range. The relatively long length L_z does not cause any curvature in the dispersion. Instead it discretizes the laterally confined modes to equidistant k_z values.

Due to the indistinguishable x and y directions certain modes are twofold degenerate. These modes can be further split in energy due to the distribution of the electromagnetic fields of the modes and boundary conditions resulting from the geometry of the nanostructure. From the Maxwell equations it follows that inside a dielectric cylindrical waveguide there can be Transverse Electric (TE), Transverse Magnetic (TM) and hybrid (HE,EH) modes. In a uniaxial crystal waveguide all the modes are of hybrid nature.[25] The mode with the largest electric field perpendicular to the interface will be the most confined and thus have the highest energy. [22, 26] It is however beyond the scope of this thesis to calculate these field distributions and the resulting energy splittings.

25 Cavity polaritons

If the structures shown in figure 2.5A and B are (partially) filled with an material that possesses electronic resonances such as excitons, the exciton can strongly couple to the confined photon mode and form a confined exciton-polariton, also known as a cavity-polariton. The first experimental observation of strong light-matter coupling in such a structure was made in 1992. [27] The resonance containing material was in that case a quantum well of GaAs which was sandwiched between cavity material devoid of electronic resonances at the specific energy range of the GaAs exciton. This system was sandwiched between distributed Bragg mirrors. In order to obtain a measurable Rabi splitting (5 meV) at low temperature (20K) several choices were made. First, GaAs was selected as the semiconductor due to its relatively large oscillator strength ($\Delta\omega_{L-T}$ =0.08 meV), relatively large exciton binding energy (4 meV) and the ability to grow epitaxial layers. Second, a quantum well was used so that the GaAs oscillator strength and exciton binding energy was enhanced (6-10 meV) by carrier confinement in the 2D layer. Third, the GaAs quantum well was positioned at an anti-node of the photon mode so that the electric field intensity was maximal at the quantum well position.

Further optimization of the system by positioning multiple GaAs quantum wells at the antinodes of a cavity mode, and carefully matching the cavity linewidth with that of the resonance to ensure efficient coupling led to the first observation of room-temperature Rabi-splitting in a microcavity.[19] Technological progress facilitated the fabrication of microcavities in which the photon field is confined in three dimensions. Placing quantum dots in such structures first allowed for the observation of enhanced and inhibited emission rates due the Purcell effect in the pertubative regime [28] similar as was observed in photonic crystals.[29] Later also strong coupling was observed.[30]

Simultaneously there has been a move to the use of so-called bulk microcavities which consist of a semiconductor material sandwiched between distributed Bragg mirrors.[31] In this way the electronic resonance containing material simultaneously forms the optical cavity. It is thought that the increased photon and exciton wave function overlap and the formation of excitons with giant oscillator strength in such cavities favors strong light-matter coupling and could, together with the selection of a suitable semiconductor (ZnO, GaN), result in exceptionally strong light-

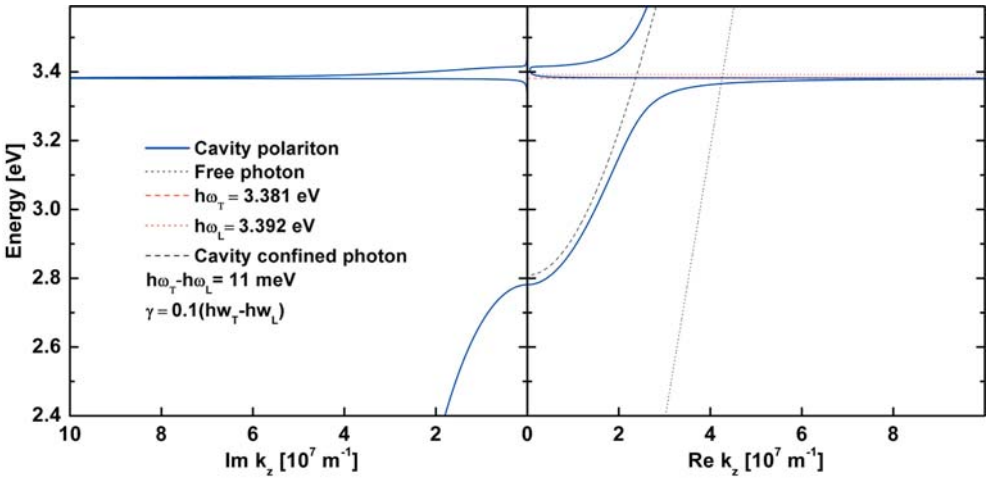

Figure 2.6 Dispersion relation for a laterally confined polariton. The confinement causes the dispersion to reach $k_z = 0$ at finite energy. In addition the upper branch is shifted to higher energy and the anticrossing takes place at lower wavevector compared to an unconfined polariton (see Fig. 2.2).

matter coupling observable at room-temperature. A recent result of a GaN bulk microcavity showed a Rabi splitting of 50 meV. [32] Finally also organic systems should be mentioned. Due to the extremely high oscillator strengths of the highly localized Frenkel excitons in organic systems remarkably large Rabi splittings (160 meV) are possible. [33] The dispersion relation of cavity polaritons can be obtained by inserting equations 19 and 20 into equation 18. Figure 2.6 shows the real and imaginary parts of the dispersion for such a cavity polariton (blue lines). The longitudinal-transverse splitting used was 11 meV and a finite damping ($\gamma = 0.1(\hbar\omega_T - \hbar\omega_L)$) was assumed. The longitudinal and transverse exciton energies are indicated by horizontal dotted and dashed red lines respectively. The confined photon mode is indicated by the black dashed curve. As a reference, the unconfined photon dispersion is also plotted as a black dotted line.

Compared to the unconfined situation (figure 2.3, green line), the confinement of the polariton has several consequences. First, the avoided crossing now occurs at lower wavevectors. Second, for energies lower than the transverse exciton energy, the exciton-photon coupling shifts the cutoff of the LPB to a lower energy. Likewise the UPB is shifted higher in energy and does not start at $\hbar\omega_L$ anymore. Thus in a laterally confined system at a

given oscillator strength, the Rabi splitting is enhanced, indicating stronger light-matter coupling than in the unconfined case. A third difference arises from the cutoff of the photon mode. The polariton dispersion now approaches $\mathbf{k}_z=0$ at finite energy as opposed to at zero energy in the unconfined case. This is an important feature of cavity-polaritons because it holds the promise of solid state Bose-Einstein condensation and polariton lasing at moderate temperatures. The next section will be dedicated to a brief overview of these topics.

26 Cooling and polariton lasing of cavity polaritons

Bose-Einstein condensation (BEC) is the phenomenon of a spontaneous phase transition of integer spin particles (Bosons) to a macroscopic coherent quantum state. It can occur when the de Broglie wavelength of the Bosons becomes comparable to their average separation. This state was predicted by Bose in 1924 [34] and Einstein in 1925. [35] In 1995 the first experimental observation of a Bose condensate of a dilute gas of Rubidium atoms cooled to 170 nanokelvins was reported.[36, 37] Proof of a truly macroscopic coherent state can come from the interference of two condensates.[38] Other demonstrations of macroscopic coherent states are superconductivity (1911),[39] the superfluidity of He^3 and He^4 (1937) [40, 41] and lasers (1958).[42] Excitons and exciton-polaritons in semiconductors are weakly interacting bosons and can be treated as real particles however without that the particle number is conserved. They were first proposed in the 1960's as candidates for Bose-Einstein condensation in the solid state.[43-45] Because of the light mass of excitons compared to atoms they would condense at much higher temperatures than atoms. To this date, no definitive proof of an exciton condensate has been given.[46, 47]

A more recent development has been the move to cavity-polaritons to obtain BEC. Cavity polaritons are advantageous for the observation of solid state BEC for three main reasons. First, the lateral confinement gives rise to a finite energy at $\mathbf{k}_z$ near zero. Second, due to the photonic nature of the polariton and the lateral confinement the effective mass of the polariton is approximately 10^4 times smaller than that of the free electron.[48] This allows cavity polaritons to condense at even higher temperatures then excitons. Third, because the cavity polaritons are mixtures of photons and excitons, light emitted at the far field from the cavity is part of the polariton wavefunction.[49] Thus demonstrating the coherence of the far-field emission

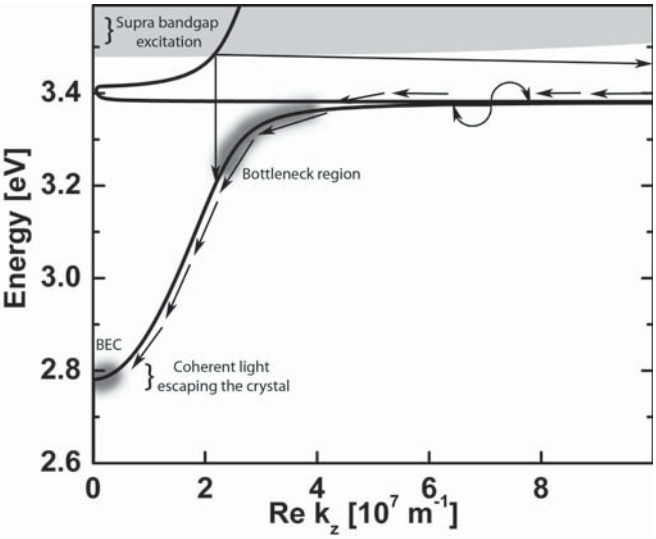

*Figure 2.7 Energy scheme of BEC of cavity polaritons. Due to the lateral confinement the polariton now has a finite energy at **k** near zero. At this energy there is a chance of BEC if this state can be sufficiently populated. This is hindered by the existance of the relaxation bottleneck region. Excitation occurs far off resonance so that the subsequent relaxation scrambles any coherence inherited from the excitation.*

by interference and polarization measurements establishes the coherent state of the condensate. This last point is the origin of the term polariton laser. [10, 48, 50] Lasers usually operate by the population inversion principle: energy is pumped into the system until the excited state acquires a larger population than the ground state so that stimulated emission can take place. In contrast, a BEC or polariton laser would already emit coherent light if the condensate is formed by a few bosons.[51] This concept holds the promise of lasers with a much reduced lasing threshold. Figure 2.7 shows the general energy scheme of BEC and polariton lasing of cavity polaritons.[10, 21, 48, 52] The system is usually excited far off resonance so that relaxation by scattering events scrambles any coherence that might be inherited from the coherent excitation. In this way, any observed coherence is due to the spontaneous phase transition to a BEC and not from the excitation. The BEC forms at the bottom of the LPB near $\mathbf{k}_z = 0$ and coherent quanta can escape from the condensate as light. At the time of writing of this thesis, BEC at 19 K, as evidenced by a large occupation of the ground state, an increase in temporal coherence and the buildup of long range spatial coherence and linear polarization, has been achieved in a cavity containing a CdTe quantum well.[52] Room temperature BEC and macroscopic coherence of cavity-polaritons however has not yet been observed.

In order to be able to observe room temperature BEC and lasing of cavity polaritons several basic material requirements would have to be met.[10] As a starting point the excitons should be stable at room

temperature. Additionally, these excitons should have a considerable oscillator strength so that the cavity operates in the strong coupling regime at room temperature. A further requirement lies in the efficiency of the thermalization.[50] Exciton-polaritons are known to have unusually short lifetimes, in the pico second range.[13] In order to obtain the thermal equilibrium required for BEC the polaritons need to scatter among themselves faster then they decay. Another obstacle might be the bottleneck for relaxation (section 2.3) which could prevent the build-up of a considerable ground state population. Due to their high exciton binding energies and oscillator strengths the semiconductor ZnO, and to a lesser extent GaN, are seen as the prime materials for the observation of room temperature BEC of exciton-polaritons.[10, 52] Whether GaN and ZnO can meet these high expectations however remains to be seen.

References

1 J. Frenkel, On the Transformation of light into Heat in Solids. I, *Phys. Rev.* **37** (1931), p. 17-44.
2 J. J. Hopfield, Theory of the contribution of Excitons to the Complex Dielectric Constant of Crystals, *Phys. Rev.* **112** (1958), p. 1555-1567.
3 C. F. Klingshirn, *Semiconductor Optics* (Springer-Verlag, Berlin-Heidelberg-New York, 1997).
4 J. J. Hopfield and D. G. Thomas, On some observable properties of longitudonal excitons, *J. Phys. Chem. Sol.* **12** (1960), p. 276-284.
5 J. J. Hopfield and D. G. Thomas, Polariton Absorption Lines, *Phys. Rev. Lett.* **15** (1965), p. 22-25.
6 C. Kittel, *Introduction to Solid State Physics* (John Wiley&Sons, New York, 1996).
7 J. Lagois, Dielectric Theory of Interacting excitonic Resonances, *Phys. Rev. B* **16** (1977), p. 1699-1705.
8 D. Meschede, *Optics, Light and Lasers*, Weinheim, 2004).
9 B. H. Bransden and C. J. Joachain, *Quantum mechanics* (Pearson education, Harlow, England, 2000).
10 M. Zamfirescu, A. Kavokin, B. Gil, G. Malpuech, and M. Kaliteevski, ZnO as a material mostly adapted for the realization of room-temperature polariton lasers, *Phys. Rev. B* **65** (2002), p. 161205/1-161205/4.
11 J. Lagois, Depth dependent eigen energies and damping of excitonic polaritons near a semiconductor surface, *Phys. Rev. B* **23** (1981), p. 5511-5520.
12 E. I. Rashba and G. E. Gurgenishvili, *Sov. Phys.-Solid State* **4** (1962), p. 759.
13 J. Wilkinson, K. B. Ucer, and R. T. Williams, The Oscillator Strength of Extended Exciton States and Possibility for Very Fast Scintillators, *Nucl. Instrum. Methods Phys. Res., Sect. A* **537** (2005), p. 66-70.
14 C. H. Henry and K. Nassau, Lifetimes of Bound Excitons in CdS, *Phys. Rev. B* **1** (1970), p. 1628-1634.
15 B. Gil and A. V. Kavokin, Giant exciton-light coupling in ZnO quantum dots, *Appl. Phys. Lett.* **81** (2002), p. 748-750.
16 P. Zu, Z. K. Tang, G. K. L. Wong, M. Kawasaki, A. Ohtomo, H. koinuma, and Y. Segawa, Ultraviolet Spontaneous and Stimulated Emissions from ZnO Microcrystallite Thin Films at Room Temperature, *Sol. Stat. Comm.* **103** (1997), p. 459-463.
17 I. I. Rabi, Space Quantization in a Gyrating Magnetic Field, *Phys. Rev.* **51** (1937), p. 652-654.
18 J. J. Sanchez-Mondragon, N. B. Narozhny, and J. H. Eberly, Theory of Spontaneous-Emission Line Shape in an Ideal Cavity, *Phys. Rev. Lett.* **51** (1983), p. 550-553.
19 R. Houdré, R. P. Stanley, U. Oesterle, M. Ilegems, and C. Weisbuch, Room-temperature cavity polaritons in a semiconductor microcavity, *Phys. Rev. B* **49** (1994), p. 16761-16764.
20 C. B. a. l. Guillaume, A. Bonnot, and J. M. Debever, Luminescnce from Polaritons, *Phys. Rev. Lett.* **24** (1970), p. 1235-1238.
21 F. Tassone, C. Piermarocchi, V. Savona, A. Quattropani, and P. Schwendimann, Bottleneck effects in the relaxation and photoluminescence of microcavity polaritons, *Phys. Rev. B* **56** (1997), p. 7554–7563.
22 A. Kuther, M. Bayer, T. Gutbrod, A. Forchel, P. A. Knipp, T. L. Reinecke, and R. Werner, Confined optical modes in photonic wires, *Phys. Rev. B* **58** (1998), p. 15744-15748.
23 J. P. Reithmaier, M. Röhner, H. Zull, F. Schäfer, A. Forchel, P. A. Knipp, and T. L. Reinecke, Size Dependence of Confined Optical Modes in Photonic Quantum Dots, *Phys. Rev. Lett.* **78** (1997), p. 378-381.
24 A. I. Tartakovskii, V. D. Kulakovski, Y. I. Koval, T. B. Borzenko, A. Forchel, and J. P. Reithmaier Exciton-photon interaction in low-dimensional semiconductor microcavities, *J. Exp. Th. Phys.* **87** (1998), p. 723-730.
25 A. W. Snyder and J. D. Love, *Optical Waveguide Theory* (Chapman and Hall, London, 1983).
26 A. V. Maslov and C. Z. Ning, Reflection of guided modes in a semiconductor nanowire laser, *Appl. Phys. Lett.* **83** (2003), p. 1237-1239.
27 C. Weisbuch, M. Nishioka, A. Ishikawa, and Y. Arakawa, Observation of the coupled exciton-photon mode splitting in a semiconductor quantum microcavity, *Phys. Rev. Lett.* **69** (1992), p. 3314-3317.
28 J. M. Gérard, B. Sermage, B. Gayral, B. Legrand, E. Costard, and V. Thierry-Mieg, Enhanced Spontaneous emission by Quantum Boxes in a Monolithic Optical Microcavity, *Phys. Rev. Lett.* **81** (1998), p. 1110-1113.

[29] P. Lodahl, A. F. v. Driel, I. S. Nikolaev, A. Irman, K. Overgaag, D. Vanmaekelbergh, and W. L. Vos, Controlling the dynamics of spontaneous emission from quantum dots by photonic crystals, *Nature* **430** (2004), p. 654-657.

[30] J. P. Reithmaier, G. Sek, A. Löffler, C. Hofmann, S. Kuhn, S. Reitzenstein, L. V. Keldysh, V. D. Kulakovskii, T. L. Reinecke, and A. Forchel, Strong coupling in a single quantum dot–semiconductor microcavity system, *Nature* **432** (2004), p. 197-200.

[31] A. Tredicucci, Y. Chen, V. Pellegrini, M. Börger, L. Sorba, F. Beltram, and F. Bassani, Controlled Exciton-Photon Interaction in Semiconductor Bulk Microcavities, *Phys. Rev. Lett.* **75** (1995), p. 3906-3909.

[32] I. R. Sellers, F. Semond, M. Leroux, J. Massies, P. Disseix, A.-L. Henneghien, J. Leymarie, and A. Vasson, Strong coupling of light with A and B excitons in GaN microcavities grown on silicon, *Phys. Rev. B* **73** (2006), p. 033304/1-033304/4.

[33] D. G. Lidzey, D. D. C. Bradley, M. S. Skolnick, T. Virgili, S. Walker, and D. M. Whittaker, Strong exciton-photon coupling in an organic semiconductor microcavity, *Nature* **395** (1998), p. 53-55.

[34] S. N. Bose, *Z. Phys. D: At., Mol. Clusters* **26** (1924), p. 178.

[35] A. Einstein, *Sitz. Ber. Preuss. Akad. Wiss. (Berlin)* **1** (1925), p. 3.

[36] M. H. Anderson, J. R. Ensher, M. R. Matthews, C. E. Wieman, and E. A. Cornell, Observation of Bose-Einstein Condensation in a Dilute Atomic Vapor, *Science* **269** (1995), p. 198-201.

[37] K. B. Davis, M.-O. Mewes, M. R. Andrews, N. J. v. Druten, D. S. Durfee, D. M. Kurn, and W. Ketterle, Bose-Einstein Condensation in a Gas of Sodium Atoms, *Phys. Rev. Lett.* **75** (1995), p. 39-69-3973.

[38] M. R. Andrews, C. G. Townsend, H.-J. Miesner, D. S. Durfee, D. M. Kurn, and W. Ketterle, Observation of Interference Between Two Bose Condensates, *Science* **275** (1997), p. 637-641.

[39] H. K. Onnes, *Commun. Phys. Lab* **12** (1911), p. 120.

[40] J. F. Allen and A. D. Misener, *Nature* **141** (1938), p. 75.

[41] P. Kapitsa, *Nature* **141** (1938), p. 74.

[42] A. L. Schawlow and C. H. Townes, Infrared and Optical Masers, *Phys. Rev.* **112** (1958), p. 1940-1949.

[43] S. A. Moskalenko, *Fiz. Tverd. Tela (Leningrad)* **4** (1962), p. 276-284.

[44] J. M. Blatt, K. W. Böer, and W. Brandt, Bose-Einstein Condensation of Excitons, *Phys. Rev.* **126** (1962), p. 1691-1692.

[45] L. V. Keldysh and A. N. Kozlov, *J. Exp. Th. Phys.* **27** (1968), p. 521-528.

[46] D. W. Snoke, Spontaneous Bose Coherence of Excitons and Polaritons, *Science* **298** (2002), p. 1368-1372.

[47] D. W. Snoke, When should we say we have observed Bose condensation of excitons ?, *Phys. Status Solidi B* **238** (2003), p. 389-396.

[48] H. Deng, G. Weihs, D. Snoke, J. Bloch, and Y. Yamamoto, Polariton Lasing vs. Photon Lasing in a Semiconductor Microcavity, *Proc. Natl. Acad. Sci. U. S. A.* **10** (2003), p. 15318-15323.

[49] V. Savona, F. Tassone, C. Piermarocchi, and A. Quattropani, Theory of polariton photoluminescence in arbitrary semiconductor microcavity structures, *Phys. Rev. B* **53** (1996), p. 13051–13062.

[50] D. W. Snoke, Coherent Questions, *Nature* **443** (2006), p. 403-404.

[51] A. Imamolu and R. J. Ram, Quantum dynamics of exciton lasers, *Phys. Lett. A* **214** (1996), p. 193-198.

[52] J. Kasprzak, M. Richard, S. Kundermann, *et al.*, Bose–Einstein condensation of exciton polaritons, *Nature* **443** (2006), p. 409-414.

Chapter 3

Synthesis and characterization of semiconducting nanowires

Semiconductor nanowires are commonly grown via a Vapor-Liquid-Solid (VLS) mechanism in which metal (nano) droplets collect the semiconductor precursors to form a solution which, when saturated, leads to the growth of a wire underneath the droplet. After a brief discussion of this general mechanism, the growth of InP and ZnO nanowires is detailed. The grown InP nanowires have an integrated alloy particle and have on average diameters of 50 nm and lengths of 10 μm. ZnO nanowires grown on silicon oxide covered substrates exhibit an integrated alloy particle, have diameters in the 50-100 nm range and lengths of up to 50 μm. In contrast, under the same growth conditions, ZnO nanowires grown epitaxially on Al_2O_3 substrates do not have an integrated gold particle and exhibit diameters mostly in the 100-300 nm range with lengths of up to 10 μm. Finally it is shown that using a method that is widely applicable for nanostructures, ZnO nanowires can be doped with cobalt ions which is an important step towards room-temperature ferromagnetic semiconducting nanowires.

3.1 Introduction

In this chapter the synthesis, doping and characterization of semiconducting nanowires using a bottom-up approach will be described. First the most widely used mechanism to explain nanowire growth; the Vapor-Liquid-Solid (VLS) mechanism will be discussed. Next, results on InP nanowire growth using laser ablation and ZnO nanowire synthesis using carbothermal reduction of ZnO powder will be presented. It is of considerable interest to obtain large quantities of aligned nanowires; therefore the epitaxial growth of ZnO nanowires on polycrystalline and single crystalline (sapphire) Al_2O_3 will be discussed. Finally a method is presented to introduce foreign atoms into the nanowires in order to modify their properties. In this case cobalt ions were substituted into the ZnO crystal lattice with the objective to obtain a semiconducting nanowire which could exhibit room temperature ferromagnetism.

3.2 VLS mechanism of nanowire growth

Nanowires are commonly grown using vapor, solution or (template directed) electrodeposition methods.[1] High temperature growth from the vapor phase is often preferred due to the high crystal quality that can be obtained and the ability to grow large quantities of wires at once. A key factor in most vapor- and solution-based methods is the presence of small metal droplets during synthesis. Analysis of the growth of silicon whiskers (hairs) from the vapor phase using gold catalyst particles lead to the postulation of the Vapor-Liquid-Solid (VLS) mechanism of growth.[2, 3] The VLS mechanism consists of three stages which are illustrated in figure 3.1A. First, a metal particle absorbs semiconductor material and forms an alloy. In this step the volume of the particle increases and the particle often transitions from a solid to a liquid state. Second, the alloy particle absorbs more semiconductor material until it is saturated. The saturated alloy droplet becomes in equilibrium with the solid phase of the semiconductor and nucleation occurs (i.e solute/solid phase transition). During the final phase, a steady state is formed in which a semiconductor crystal grows at the solid/liquid interface The precipitated semiconductor material grows as a wire because it is energetically more favorable than extension of the solid-liquid interface. that semiconductor material is precipitated at the existing solid/liquid interface as opposed to the formation of a new interface.[4]

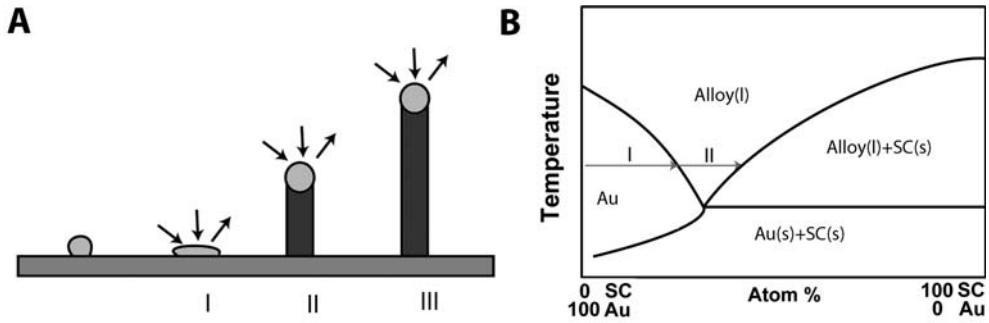

Figure 3.1(A) The stages of (I) alloying, (II) nucleation and (III) growth of nanowire synthesis according to the VLS growth mechanism.(B) Pseudobinary phase diagram of a semiconductor-gold system. The arrows indicate the subsequent phases when a gold droplet absorbes semiconductor material at a constant temperature. (I) At first, the gold particle is in the solid or liquid state. By absorbing semiconductor material, a liquid alloy is formed . (II) Subsequent absorption of more semiconductor material allows the liquid alloy to be in equilibrium with the solid semiconductor. Reproduced from reference (16).

In the VLS mechanism, the wire diameter is determined by the diameter of the alloy particle which is in turn determined by the low temperature size of the metal particle and the temperature. The wire length is determined by the growth rate and time.[5] When the system is cooled, the alloy droplet solidifies at the wire tip. To examine the feasibility of VLS wire growth from a certain semiconductor/metal combination it is essential to study the (pseudo)binary phase diagram (figure 3.1B); the metal should form an alloy with the semiconductor at a temperature that also allows the semiconductor to exist in the solid phase.

The validity of the VLS mechanism of wire growth has been proven for germanium nanowires by in-situ high temperature TEM measurements.[4] Heating neighboring gold and germanium clusters to growth temperatures and selectively evaporating the germanium clusters with an electron beam allowed for the direct imaging of the successive steps of alloying and melting, nucleation and wire growth. A study using colloidal gold catalyst particles showed that using the VLS method, (single)crystalline nanowires with diameters as small as 5 nm could be obtained.[6] Additionally, it has been shown that by increasing the VLS growth rate by modulating the temperature, crystallization only takes place at the surface of the catalyst particle resulting in the growth of nanotubes.[7]

Since the late 1990's semiconductor nanowire growth using the VLS method has enjoyed an increasing popularity with researchers and industry. The objective is the synthesis of nanowires with such diameters that electron

confinement effects can occur (d<10 nm). In addition, photon confinement can occur for diameters between 50 and 500 nm. Nanowires from numerous elemental and binary semiconductors have been synthesized using metal catalyst particles ranging from gold, silver, copper, iron to cobalt.[1] The gas phase precursors can be provided by either laser ablation,[8] metallo-organic precursor decomposition (MOCVD) [9] or a chemical reaction.[10] While VLS nanowire growth is assumed in the majority of nanowire synthesis experiments, reports of III-V nanowire growth below the melting point of the alloy particle [9, 11] or III-V nanowire growth without metal particles but in the presence of silicon oxides is also reported.[12, 13] Indeed, also in this chapter the growth of ZnO nanowires is reported which do not have an embedded gold particle at the nanowire tips. Thus while the VLS mechanism satisfactorily explains the growth of some semiconductor nanowires it could be just one of the mechanisms at play and other, more complicated, growth mechanisms should also be considered.[11, 14, 15]

3.3 Synthesis of InP nanowires

The InP nanowires described in chapter 4 of this thesis were synthesized at Philips Research Laboratories (Eindhoven, The Netherlands) using a laser ablation method.[7, 16] The experimental setup is depicted schematically in figure 3.2. An ArF laser (λ=193nm, 100mJ/pulse, 2.5-10 Hz rep. rate) is focused onto a target consisting of pressed InP powder (density 65%). To obtain n-type or p-type doped nanowires either selenium or zinc powder is mixed into the target in a concentration of typically 0.1 mol%. The target is positioned inside a quartz tube and is located approximately 30 cm upstream of the growth substrate. The growth substrate consists of a 500 nm thermal oxide covered highly doped n-type (100) silicon wafer covered by a 2 Å gold layer. It is placed inside a tube oven on top of an Al_2O_3 sample holder fitted with a thermocouple to monitor the substrate temperature (0.5 mm distance to the substrate surface). Prior to growth the tube was evacuated to a pressure of $1 \cdot 10^{-7}$ mbar and a flow of 210 sccm argon (99.9999%) was established which resulted in a pressure of 140 mbar during growth. The oven was heated to 730-850 °C which equates to a substrate temperature in the range of 425-500 °C. Ablation was conducted for 30 min. after which the substrate was allowed to cool in the argon flow. The formed material was characterized by Scanning Electron beam Microscopy (SEM, Philips XL40FEG) Transmission Electron Microscopy

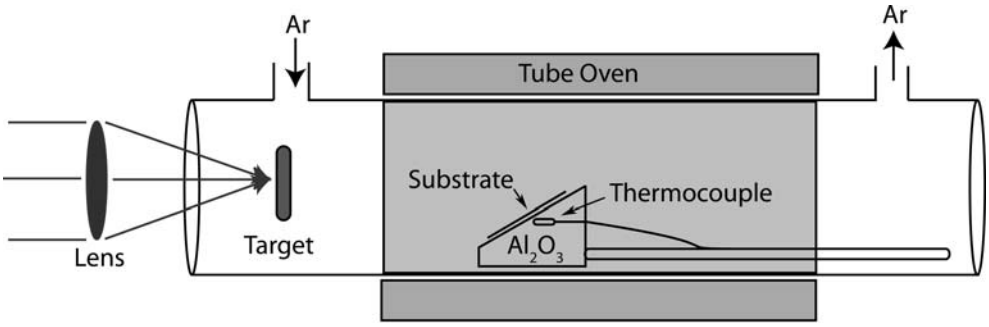

Figure 3.2 Schematic of the laser ablation setup at Philips research used for the growth of InP nanowires.

(TEM, Philips Tecnai 12) and High Resolution Transmission Electron Microscopy (HRTEM, Philips Tecnai TF30ST TEM). An SEM image of the substrate after growth is shown in figure 3.3A. The material formed has almost exclusively a wire shape; the wires have on average a length of 10 μm and a diameter of 50 nm. TEM images of the wires (fig. 3.3 B&C) show that single crystalline wires are formed (B) although also wires displaying a large number of twinning defect in the growth direction (C) are found. A HRTEM image of a single crystalline nanowire is shown in figure 3.3D. The faceted single crystalline catalyst particle can be easily distinguished. Energy Dispersive X-ray (EDX) measurements revealed that this particle consisted of gold with typically 40% dissolved InP while the wire itself consisted of equal amounts of In and P atoms. From the higher magnification HRTEM image shown in the inset it can be seen that the wire is of high crystal quality without obvious crystal defects. From electron diffraction data it was found that 95% of the wires grow along the [111]B (phosphorous terminated) direction with the cell parameters of bulk InP [5] although growth of wires along the [211] direction was also observed.

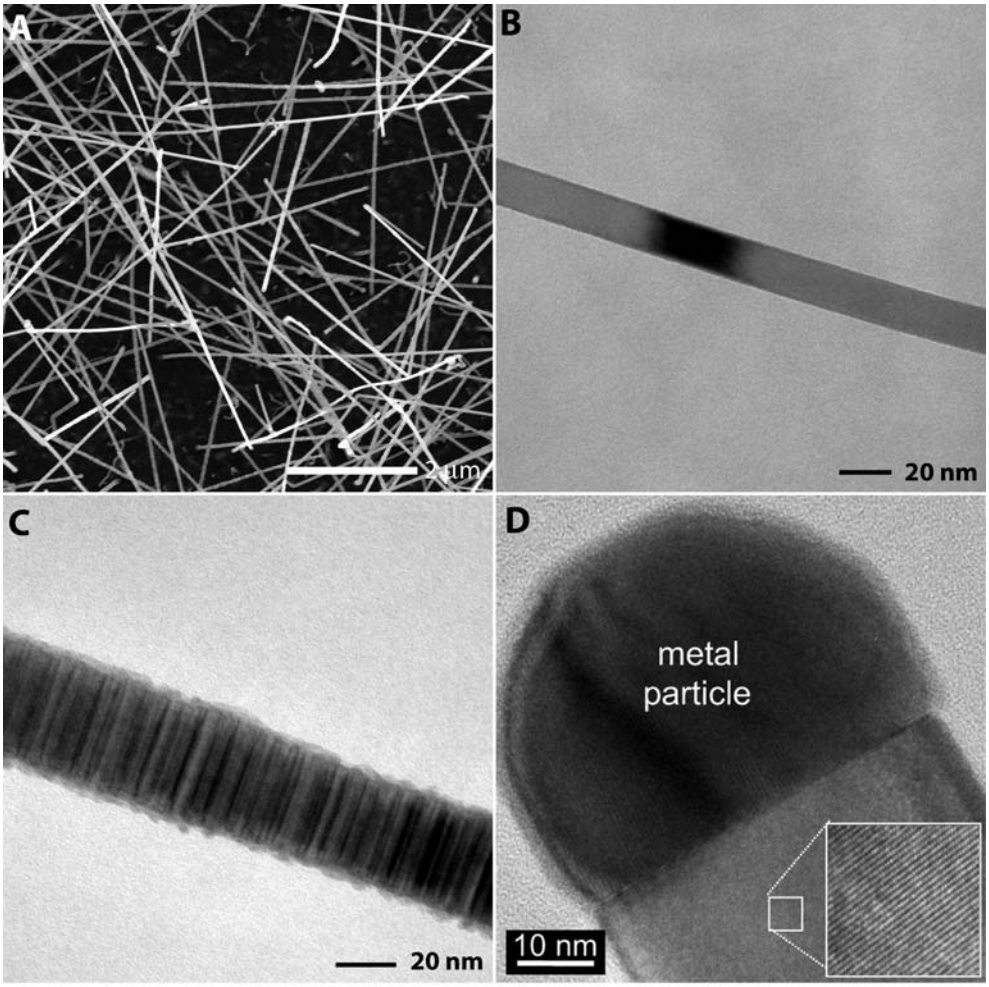

Figure 3.3 (A) SEM image of InP nanowires grown by laser ablation on a 500nm SiO_x covered Si substrate using a 2 Å gold catalyst layer. (B)TEM image of a single crystalline wire. (C) TEM image of a wire with crystal defects in the form of twinning perpendicular to the growth direction.(D) HRTEM image of a single crystalline wire showing the integrated crystalline gold containing catalyst particle. (Inset) HRTEM image of the nanowire showing the high crystalline quality.

3.4 Growth of ZnO nanowires

ZnO is a tremendously versatile, robust and cheap wide bandgap semiconductor and is therefore highly interesting for both researchers and industry. The large exciton binding energy (~60 meV) and large bandgap (3.37 eV at room temperature) make it especially suitable for room temperature optoelectronics in the near UV spectral region. The lack of a centre of symmetry of its hexagonal wurtzite crystal structure is the origin of many of its interesting and useful properties such as piezo and pyroelectricity,[17] optical non-linearities [18] and optical anisotropies.[19] A unit cell of the ZnO wurtzite crystal with lattice parameters a=3.296 Å and c=5.2065 Å [17] is shown schematically in figure 3. The tetrahedral coordination of the Zn^{2+} ions can easily be seen.[17, 20, 21] In the [0001], or c-axis, direction alternating planes of Zn^{2+} and O^{2-} ions are encountered while in the directions perpendicular to the c-axis the planes consist of equal amounts of positive and negative ions. Thus the (000X) planes are either Zn^{2+} or O^{2-} terminated resulting in polar surfaces while the (XXX0) planes are neutral. The polarity of the (000X) planes accounts for the tendency of ZnO to grow along the c-axis, thus minimizing its (high energy) polar surfaces.[17] ZnO nanowires were grown by carbothermal reduction of ZnO powder in the presence of gold catalyst particles.[10, 16] The substrates used were highly doped n-type (100) silicon wafers which had a 500 nm thermal oxide layer. A 7 Å gold layer (Chempur, 99.9999%) was deposited by plasma sputter deposition (Cressington 208HR) to supply the catalyst nanoparticles which act as nucleation sites for the growth of nanowires.

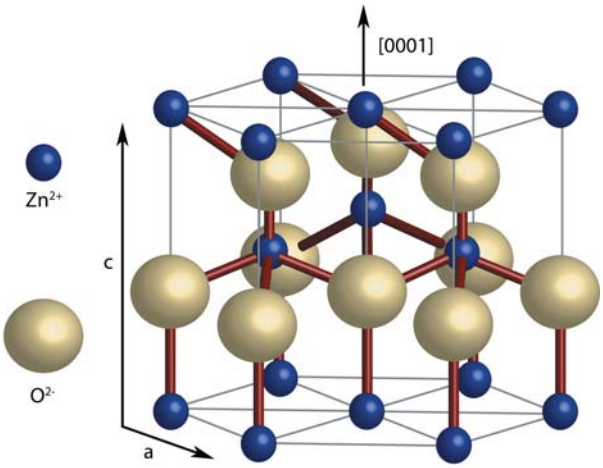

Figure 3.4 The unit cell of the hexagonal wurtzite ZnO crystal structure. The tetrahedral coordination of Zn^{2+} can easily be seen. The planes perperdicular to the [0001] direction are polar and either zinc (top) or oxygen terminated (bottom). The planes paralell to the [0001] direction contain equal amounts of zinc and oxygen ions and are thus nonpolar. [17,20,21]

During gold deposition the top edges of the substrates were masked by Scotch tape so that after growth clear side view images of the wires could be obtained. Two slightly different synthesis setups were used, both giving the same results. In the setup type I (fig. 3.5A) a small quartz tube (∅ 3 cm, length 10 cm) with one open end was placed in the middle of an argon (99.999%) flushed tube oven (Carbolite, ∅ 4 cm) with the open end downstream. In this quartz tube an aluminum oxide boat was placed containing 1 g of an equimolar mixture of zinc oxide (Chempur, 99.9999%) and carbon (Chempur, 99.999%) powders. The gold covered substrate with an area of ~1 cm^2 was placed inside the boat on top of the powder mixture, separated by an aluminum oxide spacer. The other synthesis setup was very similar except for a different shape of the quartz tube which allowed the substrate to have a lower temperature than the vapor source (fig. 3.5B). This quartz tube had a wide open end (∅ 3 cm, 6 cm length) and a narrow open end (∅ 1.5 cm, 30 cm length) and had the boat containing the powder mixture in the upstream wide end while the substrate was placed downstream, held in place by a quartz rod. The distance between the vapor source and the substrate (20 cm) was set so that at a given temperature and argon flow the substrate was located just in front of the zone were ZnO condensation would take place. In order to grow nanowires the argon flow was set to 4 l/m and the oven was ramped to 880 °C in 40 min, held at 880 °C for 30 min, and allowed to cool in ~4 hours. At these high temperatures the ZnO powder is reduced by the carbon and forms Zn vapor, CO and CO_2.

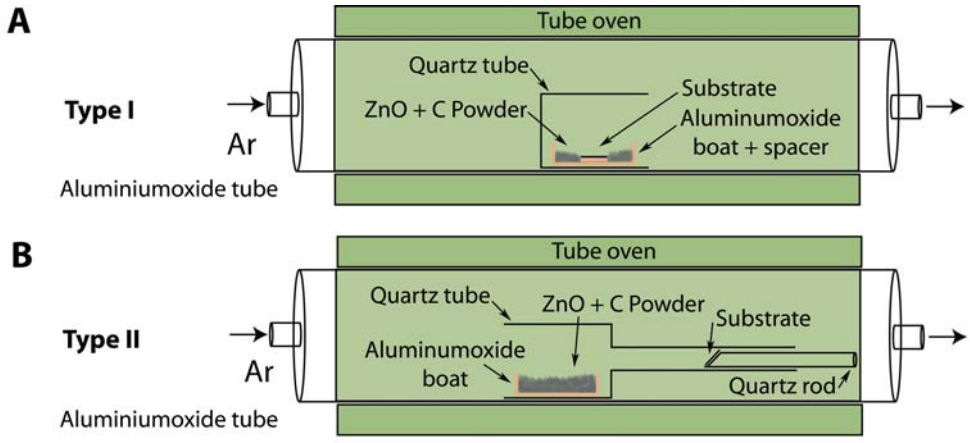

Figure 3.5 The two setups used for the synthesis of ZnO nanowires. In the setup type I (A) the substrate is located inside the vapor source. In the setup type II (B) The substrate is located downstream from the vapor source.

The gold absorbs the Zn vapor and the CO and CO_2 reoxidizes the Zn at the liquid-solid interface to form ZnO.

After synthesis, the area of the substrate which contained gold was covered with a grayish white material. Powder X-ray Diffraction (XRD) data were measured using a Philips PW1729 diffractometer fitted with a CuKα (λ=1.54 Å) X-Ray source. SEM images of the substrates after growth were obtained using a Philips XL30S FEG fitted with a Trough Lens Detector (TLD), a Backscatter Secondary Electron detector (BSE) and a Energy Dispersive X-ray (EDX) detector. The SEM was operated at 20 keV and no sample preparation was necessary. Individual nanowires were examined with a Philips Tecnai 12 TEM. For measurements in the TEM, the wires were transferred to 10 nm thick Si_3N_4 membranes by pressing the membrane onto the growth substrate.

In order to examine the crystal structure of the grown material, powder XRD measurements were done on the as-synthesized samples. Figure 3.6 shows the diffractogram of a sample grown in a type I setup at 880°C for 30 mins. After subtracting the peaks caused by either the silicon substrate, the aluminum sample holder or the tape used to attach the sample to the holder, only peaks remain that can be indexed to the wurtzite ZnO crystal structure with cell parameters a=3.24 Å and c= 5.19 Å (peaks filled in figure 3.6). The relative peak intensities of the ZnO peaks and the dominance of the peak corresponding to diffraction from the (0002) plane, indicate that the crystals are preferentially ordered along the wurtzite crystal c-axis ([0001] direction).

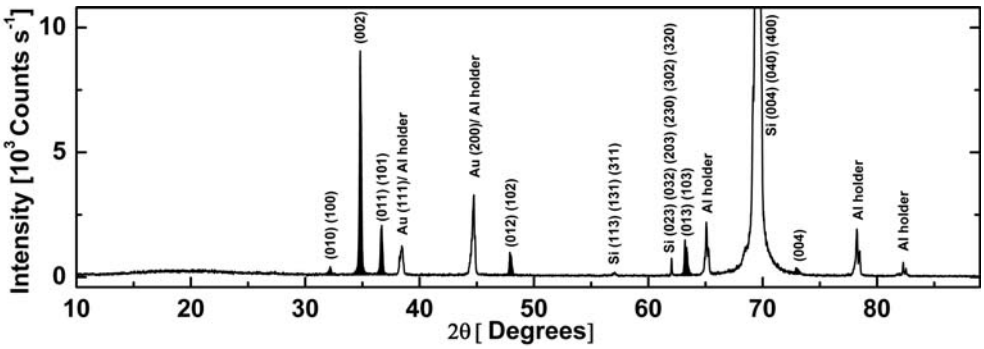

Figure 3.6 X-ray difraction pattern of ZnO nanowires grown on a 500 nm thermal oxide covered silicon substrate for 30 minutes at 880 ^{0}C under an argon atmosphere. The gold catalyst layer was 7 Å thick and was deposited by plasma sputter deposition.

SEM and TEM images of wires grown on Si/SiO_x are shown in figure 3.7. Figures 3.7A and 3.7B show the respective top- and sideview (parallel to the substrate surface) images of a sample grown in a type I setup at 880°C for 30 mins. Growth of long (~50 μm) and relatively thin (50-100nm) disordered nanowires can be seen from the topview image. The absence of nanowire growth in the substrate area that didn't contain gold, as seen in the side view image, clearly illustrates the specificity of the synthesis. A SEM image of wires grown for only ten minutes (fig. 3.7C) reveals the non-wire shaped ZnO layer at the bottom of the substrate. This ZnO "wetting layer" is in fact observed for all ZnO nanowires grown on Si/SiO_x substrates. An image of the same area with the BSE detector (fig. 3.7D) shows that particles of high electron density are located at the tips of the wires as well as in the wetting layer. EDX measurements on these particles indicated a high concentration of gold although the presence of Zn could not be determined due to the large ZnO background. Representative TEM pictures of broken off wires can be seen in figures 3.7E&F. The wires have an integrated faceted gold particle at the wire tips of the same diameter as the wires. Despite the rough surfaces, a hexagonal crossection can still be distinguished, as expected for wurtzite nanowires. It must be remarked that nearly 90% of the samples grown in the manner described above resulted in the growth of useable material (i.e. wire shaped, of sufficient length, without branching or kinks) although identical conditions did not yield identical (i.e. length, diameter) results.

In summery, disordered wurtzite ZnO nanowires of diameters between 50 and 100 nm were grown at 880 °C using Si/SiO_x substrates covered with a 7Å gold layer. The absence of wire growth in areas which were masked during the gold deposition, the presence of integral gold containing particles at the wire tips and the similarity of the wire diameter and the catalyst particle diameter make it highly likely that these wires were grown via the VLS mechanism.

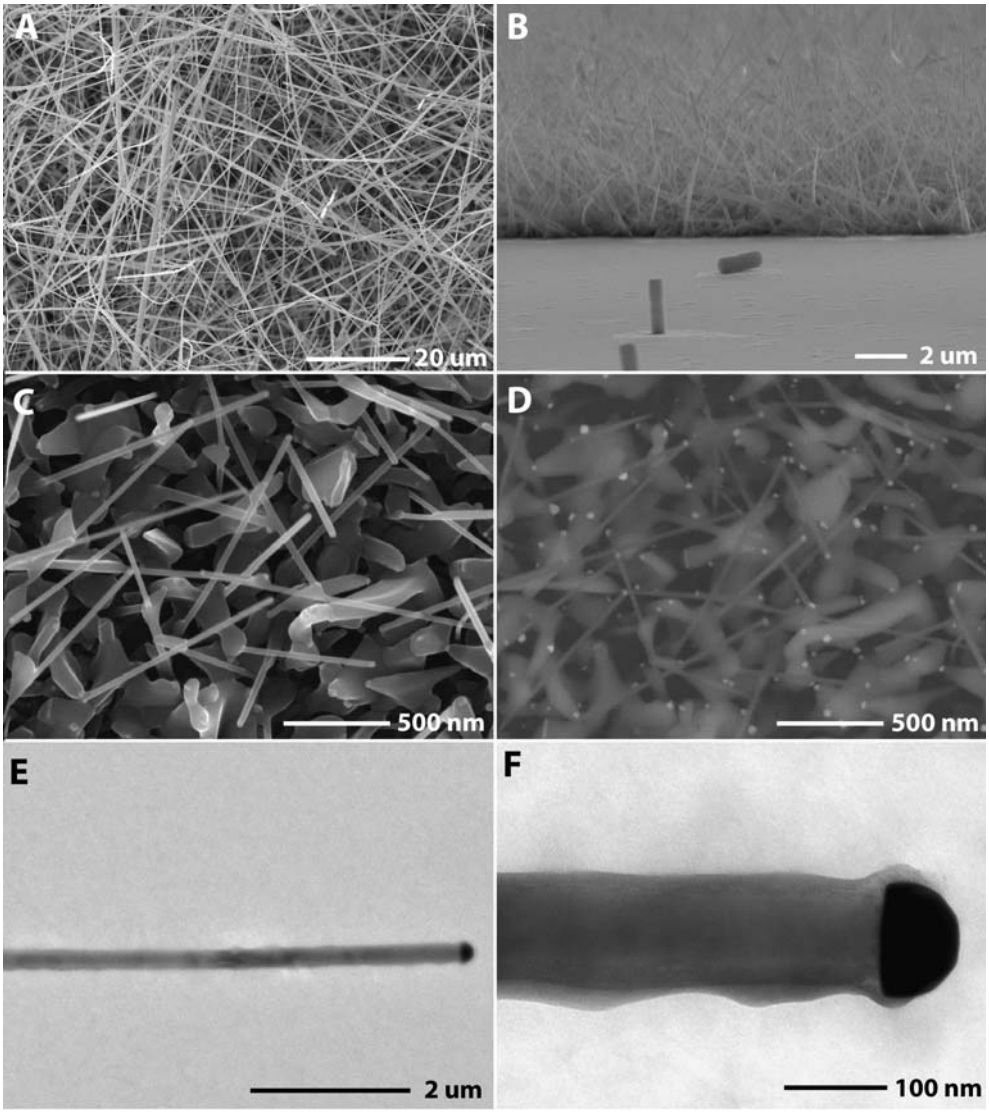

Figure 3.7 (A-D) SEM images of ZnO nanowires grown on a 500 nm siliconoxide covered silicon substrate covered with a 7 Å gold layer, deposited by plasma sputter deposition. (A) topview. (B) Sideview parallel to the surface. (C) Topview of a sample with a growth time of 15 mins. (D) Backscatter image of the same area as in (C) showing the gold catalystparticles at the wire ends. (E) TEM image of a typical ZnO nanowire grown on siliconoxide covered substrates. (F) Higher magnification image.

3.5 Epitaxial growth of ZnO nanowires on Al_2O_3 substrates

It is of considerable interest to obtain large areas of aligned nanowires to exploit the properties arising from the nanowire morphology in macroscopic devices. It is known that [0001] oriented ZnO layers [22] and nanowires [23] can be epitaxially grown on the $(11\bar{2}0)$ plane (a-plane) of single crystalline Al_2O_3 (sapphire). The ZnO unit cell a-axis (3.296 Å) is related to the sapphire unit cell c-axis (12.99 Å) by a factor of four resulting in the configuration of ZnO[0001]||sapphire[$11\bar{2}0$] with a lattice mismatch of only 0.08% at room temperature.[22]

ZnO nanowires were grown on 7 Å gold covered polycrystalline or single crystalline (sapphire) Al_2O_3 substrates in a type I setup at 880°C (see section 3.4 for the experimental details). Figure 3.8 shows the X-Ray Diffractogram of ZnO nanowires grown for 30 minutes on a polycrystalline Al_2O_3 substrate. Aside from the abundance of peaks resulting from the polycrystalline Al_2O_3 substrate or the aluminum sample holder all remaining peaks could be assigned to the ZnO wurtzite crystal structure with cell parameters a=3.24 Å and c= 5.19 Å (five peaks filled in figure 3.8). The large ZnO (0002) peak shows that the majority of growth was in the [0001] direction although also significant ZnO $(10\bar{1}3)(01\bar{1}3)$ and $(11\bar{2}0)$ peaks were found indicating growth in other directions. SEM images of the sample (figure 3.9A&B) show that there are domains in which the orientation of wire growth is uniform. Such a uniform domain is likely grown on a facet of the Al_2O_3 polycrystal. Figure 3.9B shows a higher magnification image of a domain in which the wires grew perpendicular to the substrate.

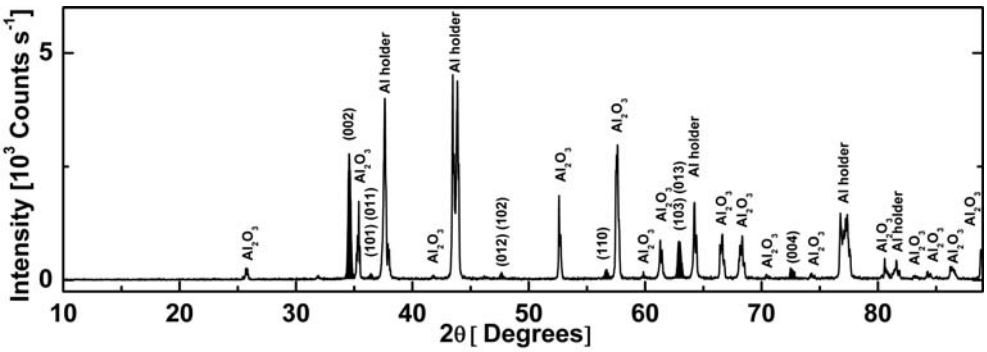

Figure 3.8 X-ray difraction pattern of ZnO nanowires grown on an polycrystalline Al_2O_3 substrate for 30 minutes at 880 ^{0}C under an argon atmosphere. The gold catalyst layer was 7 Å thick and was deposited by plasma sputter deposition.

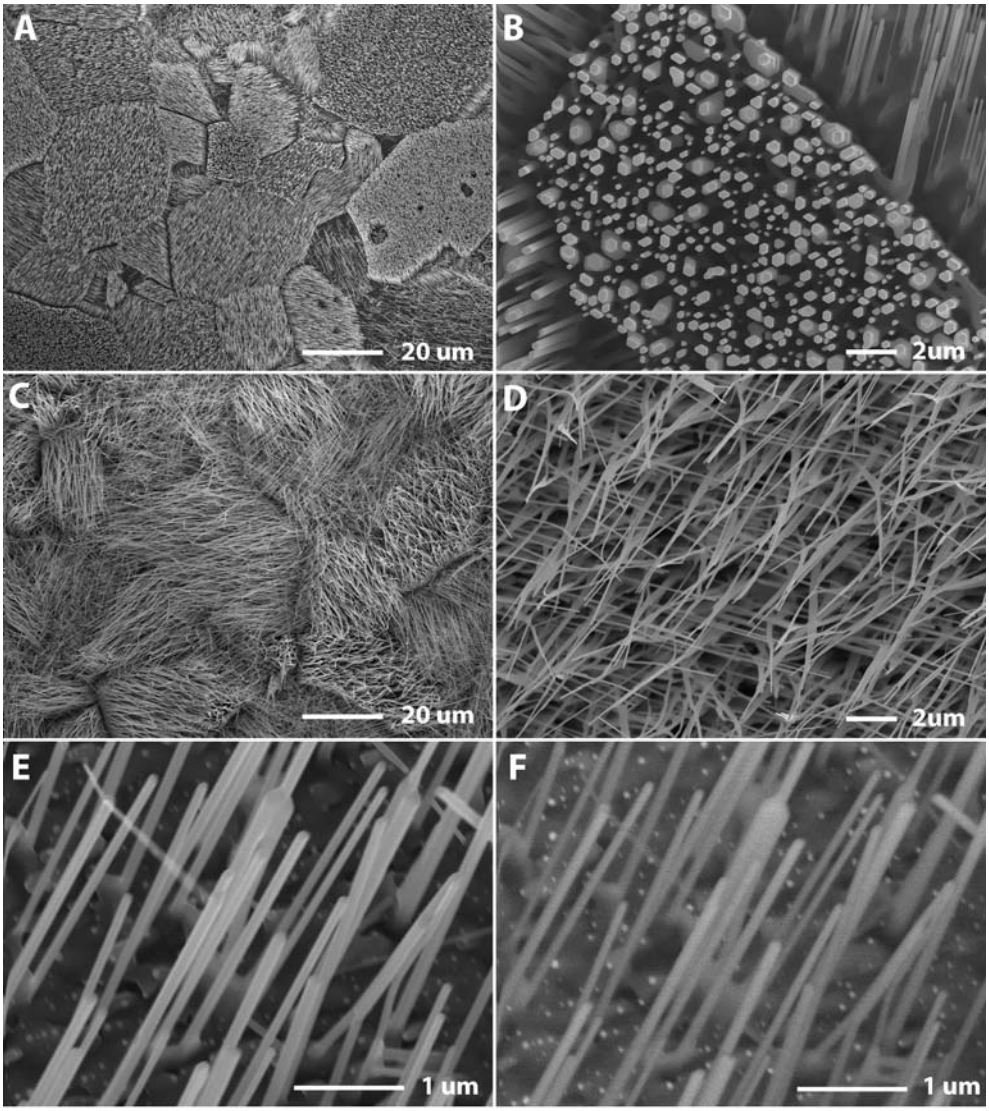

Figure 3.9 ZnO nanowires grown on a polycrystalline Al_2O_3 substrate using a 7Å gold catalyst layer deposited by plasma sputter deposition. The samples were grown at 880^{0}C for 30mins (A&B) and 45 mins (C&D) using a setup type I. (E) Higher magnification image of (A) showing the gold catalyst particles at the bottom of the wires. (F) Same area as (E) but imaged with an backscatter electron detector which is sensitive to atoms mass. The heavy gold particles can be easily seen at the substrate surface. No gold particles are located at the top of the nanowires.

The wires have diameters in the range of 100-300 nm with clear hexagonal crossections.This is consistent with growth of the nanowires in the [0001] direction. Also note that the side facets of the wires are all in the same three directions, demonstrating the epitaxial relation between the wires and the substrate. In figures 3.9C&D SEM images of a sample grown for 45 minutes are shown. The wires are so long that they bend and stick together, although the domain structure can still be distinguished. A high magnification SEM image of the wires grown for 30 minutes is shown in figure 3.9E. A large quantity of high electron density particles can be seen at the surface of the substrate. From the electron backscatter image of the same area (fig.3.9F) it is apparent that these particles are not present at the tips of the nanowires. In addition, the particles at the substrate surface are typically two to ten times smaller than the diameters of the wires. The observations reported above were typical of all samples grown on polycrystalline Al_2O_3 (30).

Next, the growth of ZnO nanowires on the $(11\bar{2}0)$ surface of sapphire was studied. Figure 3.10 shows the X-ray diffractogram of a sample grown from a 7Å gold layer for 30 minutes at 880C° in a type I setup. The diffractogram is highly simplified with respect to that of wires grown on Si/SiO_x (fig.3.6) and poly-Al_2O_3 (fig. 3.8). It shows almost a single peak which could be indexed to the (0002) plane of the ZnO wurtzite crystal structure with cell parameters a=3.24 Å and c= 5.19 Å (threepeaks filled in figure 3.10). A topview SEM image of this sample is shown in figure 3.11A. The wires have a hexagonal crossection and have diameters from 100 nm to 1 μm, with the majority in the 200-300 nm range. The side facets

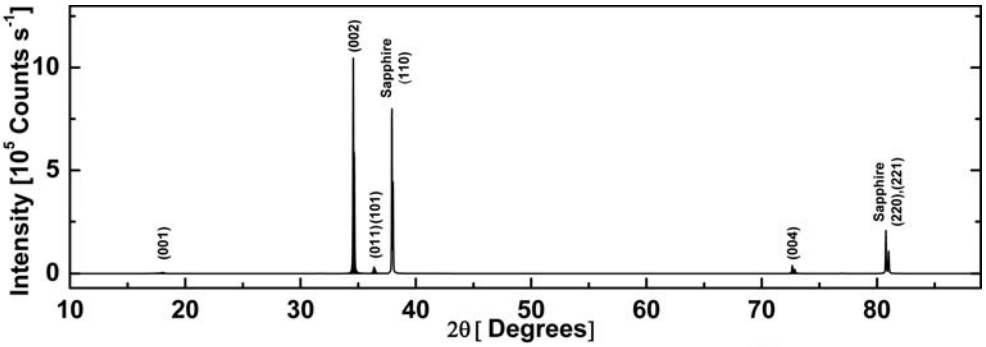

Figure 3.10 X-ray difraction pattern of ZnO nanowires grown on an $11\bar{2}0$ oriented sapphire substrate for 30 minutes at 930 ^{0}C under an argon atmosphere. The gold catalyst layer was 7 Å thick and was deposited by plasma sputter deposition.

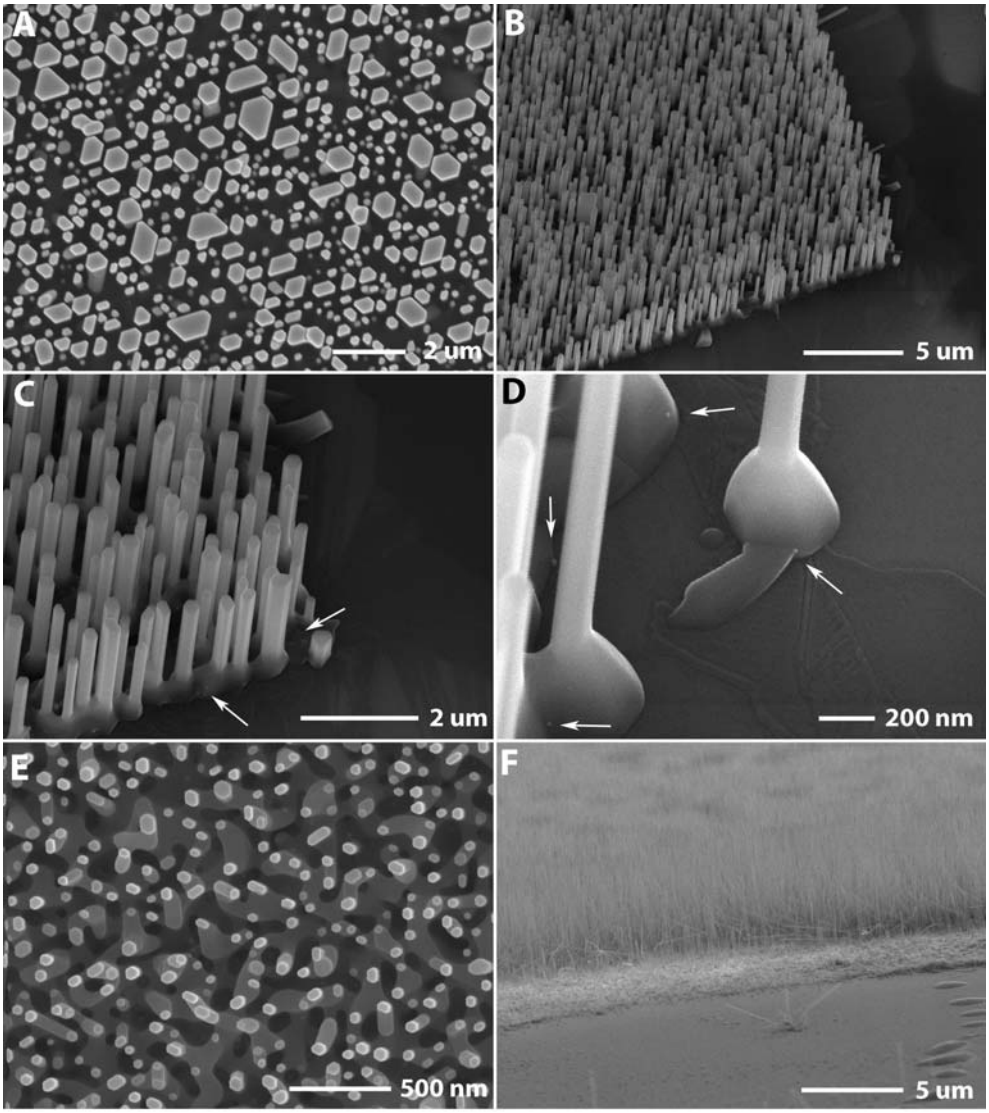

Figure 3.11 (A-D) SEM images of ZnO nanowires grown epitaxially on a-plane sapphire at 880^{0}C in a type I setup. (A) Topview of a sample that was grown for 30 minutes showing the hexagonal crossections and the forced orientation of the nanowire side facets. (B) Sideview image (tilted at 45^0) of a sample grown for 15 minutes showing the difference in wire growth in areas which contained gold particles (left) and areas that contained no gold partcicles (bottom/right). (C) Higher magnification image of the edge of the wire growth area. Arrows indicate gold particles.(D) Higher magnifucation image clearly showing the gold catalyst particles (arrows) which remain at the bases of the nanowires. (E) SEM image of a sample which was grown under the same conditions as (A). (F) Sideview of the sample taken parallel to the surface.

have exclusively three orientations, showing the epitaxial connection with the substrate. SEM pictures taken under an angle of 45° to the surface of a sample that had its edges covered during gold deposition (7 Å) and was grown for 15 minutes at 880°C are shown in figures 3.11B, C and D. Figure 3.11B shows the specificity of the wire growth for the gold covered area. The higher magnification images shown in figure 3.11C&D show that the wires have pedestals which have grown together. The arrows indicate high electron density particles at the bases of the wires. No particles have been found on the wire tips and also no particles corresponding to the wire diameters have been found. The images shown in figure 3.11A-D are representative for approximately 10% of samples grown (60) on $(11\bar{2}0)$ sapphire substrates at the same conditions. The majority of the samples (85%) have the morphology shown in figures 3.11E&F. From the topview image (fig. 3.11E) it can be seen that these wires have hexagonal crossections with diameters in the range of 50-150 nm. The wires are still grown epitaxially as evidenced from the three discrete directions of the side facets. However, also an intricate structure can be observed in between the wires. This "wetting layer" is apparent from the image taken parallel to the substrate surface (fig. 3.11F). While this layer makes bulk measurements of the optical properties of the nanowires difficult it can be advantageous for other applications requiring electrical contacts to the wires. A further 5% of the samples grown under the same conditions displayed growth of ZnO layers.

To examine the crystal structure of the epitaxially grown wires more closely, TEM and HRTEM measurements on individual broken off ZnO nanowires were made. Figures 3.12A-D show TEM images of a representative wire. In the bright-field image (fig. 3.12A) no crystal defects are apparent. The selected Area Electron Diffraction (SAED) image shown in the inset confirms the single crystalline structure of the wire with the lattice parameters of bulk ZnO. The dark-field TEM image shown in figure 3.12B also displays no apparent crystal defects. (the difference in contrast is caused by curvature of the underlying 10 nm thick Si_3N_4 TEM membrane). A higher magnification bright-field image of the top end of the wire (fig. 3.12C) reveals that it is rounded. In the bright-field image of the broken off lower end (fig. 3.12D), the hexagonal crossection can be identified. HRTEM images of a middle part and the top end of an epitaxially grown ZnO nanowire (different wire) are shown in figures 3.12E&F respectively. The lattice planes perpendicular to the wires long axis can clearly be seen. The

distance between these lattice planes is 2.59 Å corresponding reasonable well to the distance between the (0002) planes of wurtzite ZnO (2.60 Å) thus confirming the (0001) nanowire growth direction. Surprisingly, there appears to be a polycrystalline/amorphous surface layer of some nanometers thickness. This layer is more or less observed in all ZnO wires. Likely causes of this surface layer can be zinc hydroxides from reaction with moist in the air or carbon resulting from the synthesis. The wire itself displays no inhomogeneous contrast which could point to the existence of an integrated catalyst particle or crystal defects. This total absence of alloy catalyst particles at the wire ends and the relative diameters of the found catalyst particles in the SEM images to that of the wires make it unlikely that these wires were grown by the VLS mechanism. The experimental results are more inline with a gold catalyzed vapor-solid mechanism in which the gold particle is the initial nucleation centre after which VS growth takes over. This could explain the exclusive growth of wires in areas which were covered with gold together with the absence of gold particles in the wires. Efforts were made to obtain VLS grown wires on sapphire substrates by using a setup type II. In this setup, the substrate is separated from the vapor source by 20 cm so that its temperature could be significantly (~75° C) lower than the vapor source (the carbothermal reduction of ZnO does not take place below 825° C). The results of these synthesis were however very similar to the ones presented above therefore for the remainder of the experiments a setup type I was used.

In conclusion, ZnO nanowires of high crystal quality can be grown epitaxially on aluminum oxide substrates. The yield is almost 100% for growth on polycrystalline substrates, resulting in domain ordered nanowires with diameters in the 100-300nm range. Growth of single domain ordered nanowires oriented perpendicular to the substrate with diameters in the 100nm-1μm range was demonstrated although only with a yield of 10%. The wires grow along the [0001] direction and have the bulk ZnO crystal structure. These wires probably do not grow according to the VLS mechanism but rather a gold catalyzed VS mechanism in which the gold acts as an initial collection center after which VS growth takes over.

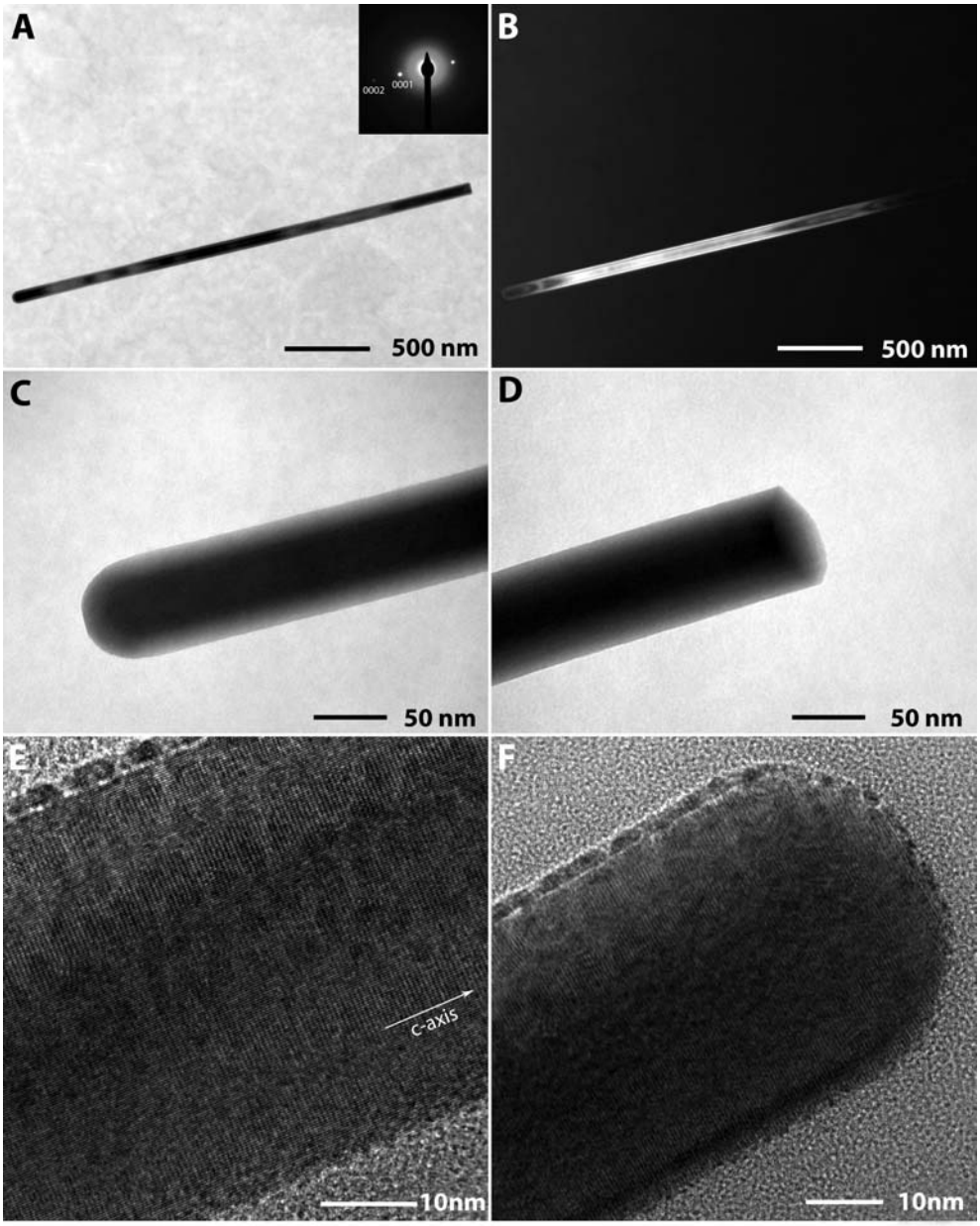

Figure 3.12 TEM images of ZnO nanowires grown epitaxially on Al_2O_3 substrates in a type I setup using a 7 Å gold layer. (A) BF image (Inset) SAED pattern of a 300 nm section of the wire. (B)DF image clearly showing the single crystalline structure of the wire. (C) Higher magnification BF image of the nanowire end located furthest from the substrate. (D) Higher magnification BF image of the base of the nanowire showing the hexagonal crossection. (E&F) HRTEM images of a middle section (E) and top end (F) of a different wire.

3.6 Cobalt doping of ZnO nanowires

3.6.1 Introduction

Currently, efforts are being made towards semiconductor devices that operate not only with the electron charge (electronics) but also utilize the electron spin as an added degree of freedom (spintronics). Therefore materials of combined ferromagnetic and semiconducting nature, preferably at room temperature, are needed. Room temperature ferromagnetic semiconductors have been around for over three decades now but those early materials were very laborious to make and are incompatible with semiconductor technology.[24] A more feasible method to obtain a magnetic semiconductor is by introducing appropriate transition metal or rare earth group elements into III-V, II-VI and oxide crystal lattices.[25, 26] These first so-called Diluted Magnetic Semiconductors (DMS) based on InAs:Mn however displayed only ferromagnetism up to 110K. The prediction of room-temperature ferromagnetism in Mn substituted p-type ZnO and GaN [27, 28] lead to extensive research of DMS based on these materials [29-31] and resulted in the first observations of ferromagnetism at room temperature in thin films of TiO_2:Co,[32] SnO_2:Co[33] and ZnO:Co[34]. Later reports confirmed these observations of room temperature ferromagnetism in cobalt [35-39] or other transition element substituted ZnO.[40-44] However also reports indicating a Curie temperature below room temperature [45-47] or even below 4K [48, 49] appeared. A systematic study of ZnO substituted with 5 % of the period 4 transition metals showed that ZnO:Co has the highest magnetic moment (2.6 μ_B/dopant atom) at room temperature whereas ZnO:Cr, ZnO:Mn, ZnO:Cu and ZnO:Zn had no measureable magnetic moment at room temperature. [50]

Due to these wildly varying results a lot of debate has ensued about the origin of the ferromagnetism in many of the transition metal substituted zinkoxides. An obvious origin, the existence of additional magnetic phases such as metals or oxides, could be rebutted by optical and TEM characterizations showing that the impurity atoms are indeed incorporated in the crystal lattice and are not present as nanoclusters.[34, 45, 51-53] In addition, the measurement of room temperature ferromagnetism in ZnO thin films substituted with the non magnetic ions Sc^{3+} ($3d^0$) and the unlikelihood of electron transfer to scandium rules out the existence of additional phases as the origin of the ferromagnetism.[50] Over the past two years a consensus is beginning to form that the observed ferromagnetism in

ZnO:Co is the result of interaction of the impurity electrons with defect bound carrier electrons introduced by donor defect states, described in a so called spin-split impurity band model.[50, 54-56] More specifically, the room temperature ferromagnetism in ZnO:Co as well as the conductivity can now be turned on and off by introducing and removing interstitial Zn atoms, a known donor defect in ZnO crystals.[54]

Semiconducting nanowires are seen as highly promising building blocks for future (opto-)electronic devices at the nanoscale.[57] One of their key features, making them highly versatile, is the ability to introduce foreign atoms into the crystal lattice to specifically tailor the optical and electrical properties.[58, 59] For instance, doping InP with zinc or selenium results in nanowires displaying p or n type behavior respectively [60] or doping of GaN CdS and ZnS nanowires with Mn results in a modified photoluminescence emission spectrum.[61] It would be highly advantageous to extent the range of applications of nanowires into the field of spintronics.[62] Given the previous results on ZnO:Co powders and thin films, ZnO:Co nanowires are an obvious choice. Previously, ZnO:Co nanowires have been synthesized by low temperature electrodeposition, [63] low temperature solution based synthesis, [64] laser ablation [65] and chemical vapor deposition (CVD) [66] methods. Evidence of (room-temperature) ferromagnetism was given from magnetization measurements on the whole samples in the cases of electrodeposition and CVD. Both in situ doping methods resulted however in nanowires with small aspect ratios of (14:1)[63] and (4:1)[66] and no hexagonal crossections.

It is well known that undoped ZnO nanowires of excellent crystal quality and with large aspect ratios can be grown by a high temperature vapor based synthesis (e.g. see sections 3.4 and 3.5 or references [10, 23]). Therefore, an ex situ procedure, using doping of already grown nanowires, seems appropriate. The following sections will describe an ex situ doping method to obtain high aspect ratio (>150) ZnO:Co nanowires of high crystal quality by means of a dip-doping-annealing method. First, high quality ZnO nanowires are grown which are subsequently dipped into a cobalt salt solution forming a cobalt containing shell around the nanowires. A further annealing step results in the incorporation of the cobalt ions in the ZnO crystal lattice. This method exploits the large surface to volume ratio of nanostructures and can in principle be used to introduce foreign atoms to tailor the properties of any nanostructure.

3.6.2 Experimental

ZnO nanowires where synthesized on SiO_2 covered silicon substrates using a 7 Å gold catalyst layer deposited by plasma sputter deposition as described in section 3.4 of this chapter. In order to dope the wires with cobalt, substrates containing ZnO wires were immersed in an aqueous 3.6 g/l cobalt acetate solution for two hours and left to dry at room temperature. Subsequent annealing took place at 900°C for eight hours in air. Diffuse reflectance spectra were acquired using a Perkin-Elmer UV/VIS spectrometer. Powder X-ray diffraction data were acquired using a Philips PW1729 diffractometer fitted with a CuKα (λ=1.54 Å) X-Ray source. High Resolution Transmission Electron Miscroscopy (HR-TEM) images, Energy Dispersive X-Ray (EDX) data and Scanning Transmission Electron Microscopy – High Angle Annular Darkfield (STEM-HAADF) data were acquired with a Philips Tecnai 12 TEM operating at 120 KeV. For measurements in the TEM, the wires were transferred to 10 nm thick Si_3N_4 membranes by pressing the membrane onto the growth substrate.

3.6.3 Results and Discussion

To check whether any Zn^{2+} ions have been substituted by Co^{2+} ions, diffuse reflectance spectra were taken of the ZnO wires before, during and after the dip-dope-anneal procedure. Fig 3.13 shows the normalized diffuse reflectance spectra of: ZnO powder (blue line), ZnO nanowires grown on a ~300nm SiO_2 covered silicon substrate (red line)(see section 3.3 for the synthesis details), the same nanowires but after additional soaking in a aqueous 3.6 g/l cobaltacetate solution for two hours and subsequent drying at room temperature (green line) and the same nanowires but after additional soaking in an aqueous 3.6 g/l cobaltacetate solution for two hours, drying at room temperature and subsequent annealing at 900°C for eight hours in air (black line). For comparison, diffuse reflectance data of $Zn_{0.994}Co_{0.006}O$ pellets [67] taken from reference [68] has been plotted (dotted line). The ZnO powder reflectance spectrum shows a high reflectance over the whole visible energy range without any structure. At energies higher than the ZnO bandgap of 3.37 at room temperature, the reflectance is diminished due to band to band absorption. The as synthesized ZnO nanowires (red line) also show a high reflectance without any significant structure in the visible range. A marked difference with the ZnO powder data is that the band edge appears steeper and is redshifted by some 65 meV. This energy shift corresponds well to the exciton binding energy in

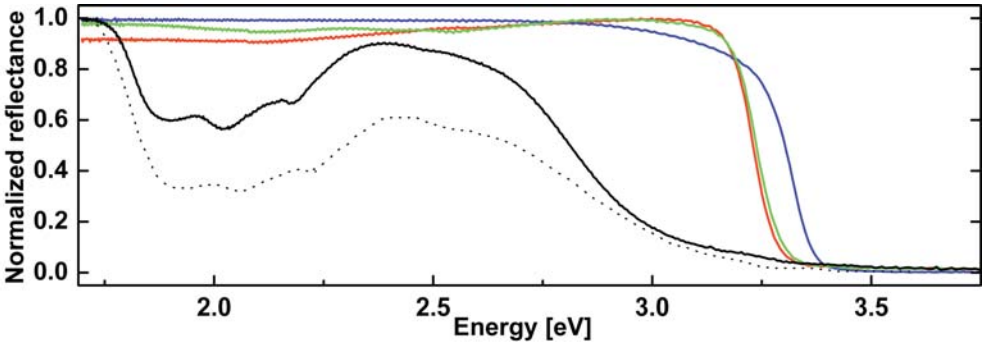

Figure 3.13 Diffuse reflectance spectra of ZnO powder (blue line), ZnO nanowires grown on a ~300nm covered SiO_2 substrate (red line), ZnO nanowires grown on a ~300nm covered SiO_2 substrate after soaking in 3.6 g/l aqueous cobaltacetate solution for two hours and subsequent drying (green line), ZnO nanowires grown on a ~300nm covered SiO_2 substrate after soaking in 3.6 g/l cobalt nitrate solution for two hours and subsequent annealing at 900 ^{0}C for 8 hours (black line). The dotted line indicates reflectance data for $Zn_{0.994}Co_{0.006}O$ powder taken from reference (68).

ZnO of 60 meV (see section 2.1) leading to the conclusion that the recrystallization from low crystal quality powder to high crystal quality nanowires allows excitons to exist in these nanowires. The reflectance spectrum does not markedly change after the wires have been soaked in the cobalt acetate solution and let to dry (green line). Only after subsequent annealing at 900°C for eight hours in air, is a significant change of the reflectance spectrum obtained; the bandgap drastically shifts to lower energy by 410 meV and three dips in the reflectance at 1.88 eV (660nm), 2.02 eV (614nm) and 2.18 eV (569nm) can be seen. The reflectance spectrum looks qualitatively very similar to that obtained from cobalt substituted ZnO pellets (dotted line) taken from reference.[68] These dips in the reflection are due to transitions between the crystal-field and spin-orbit split 3*d* levels of tetrahedral coordinated Co^{2+} ions substituting Zn^{2+} ions in the wurtzite ZnO crystal structure. [52, 68-72] Importantly, these transitions have also been found in ZnO:Co materials that display room temperature ferromagnetism.[34, 45, 50, 51, 53] In addition, by variation of the soak time and concentration of the solution, the intensity of the dips in the reflectance spectrum could be altered (not shown) indicating control over the doping concentration. From the reflection data it can thus be concluded that Co^{2+} is successfully substituted for Zn^{2+} in our ZnO nanowires.

To obtain more information on the crystal structure of the Co^{2+} substituted ZnO nanowires, powder X-ray diffraction measurements were made. Figure 3.14 shows the X-ray diffractogram of ZnO nanowires which

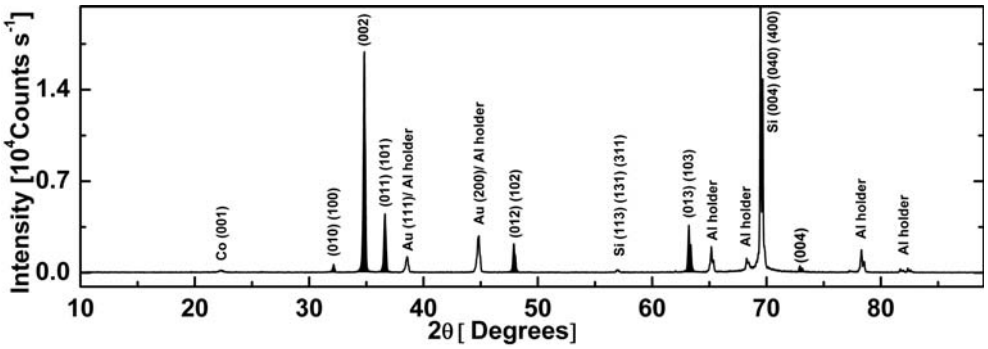

Figure 3.14 X-ray difraction pattern of ZnO nanowires grown on a 300 nm thermal oxide covered silicon substrate for 30 minutes at 880 ^{0}C under an argon atmosphere. The gold catalyst layer was 7 Å thick and was deposited by plasma sputter deposition. After growth, the wires were soaked in 0.36 g/l cobalt acetate solution for two hours and subsequently annealed at 900 ^{0}C for 8 hours.

have been soaked in an aqueous 3.6 g/l cobalt acetate solution for two hours, have been dried at room temperature and are subsequently annealed at 900°C for eight hours in air. Aside from diffraction peaks from the Si/SiO_x substrate and aluminum sample holder the sample shows the diffraction peaks of wurtzite ZnO (filled in fig. 3.14) with lattice peak parameters a=3.24 Å and c= 5.19 Å (also compare with figure 3.6). [10] No other oxidic phases are detected although it must be noted that a small peak attributable to Co metal can also be distinguished.

Because powder X-ray diffraction only measures the average properties of the entire sample, the detected metallic phase is not necessarily located in or on the nanowires but could also be present on the surface and sides of the substrate. Therefore HR-TEM investigations were done on the doped and annealed wires. Figure 3.15 shows HR-TEM images of a wire after soaking in an aqueous 3.6 g/l cobalt acetate solution for two hours, drying at room temperature and subsequent annealing at 900° C for eight hours in air. The images appear no different than those obtained from wires without doping treatment (see fig. 3.12); the two lines along the length of the wire in panel (A) are not caused by a change in material crystal structure (e.g. a core shell nanowires) but are directly caused by the hexagonal cross-section of the wurtzite nanowires. The higher magnification images of the top edge (B), middle section (C) and lower edge (D) confirm that in all three regions the wire has the wurtzite crystal structure and is oriented with the crystal c-axis along the length of the nanowires. The separation between lattice planes is 2.6 ± 0.1 Å in all three regions which corresponds to the distance between the (0002) planes, indicating that the wurtzite crystal c-axis [0001] direction is aligned with the nanowire's long axis. This is also in agreement to the separation between the (0001) lattice planes of 5.19 Å as obtained from the powder X-Ray diffraction data. From this data it can however not be concluded that any shrinkage of the unit cell in the c-direction has occurred upon the incorporation of the smaller Co^{2+} ion. We found no evidence that additional crystalline phases are present although sometimes, for instance in Fig 3.15B, it can be seen that there is an additional polycrystalline/amorphous layer present at the edge of the wire. This layer can often also be seen on untreated ZnO nanowires (see figure 3.12) and is therefore not related to the cobalt doping procedure. Thus, the HR-TEM measurements show that there is no difference in crystal structure between the undoped ZnO wires and the Co^{2+} doped ZnO wires.

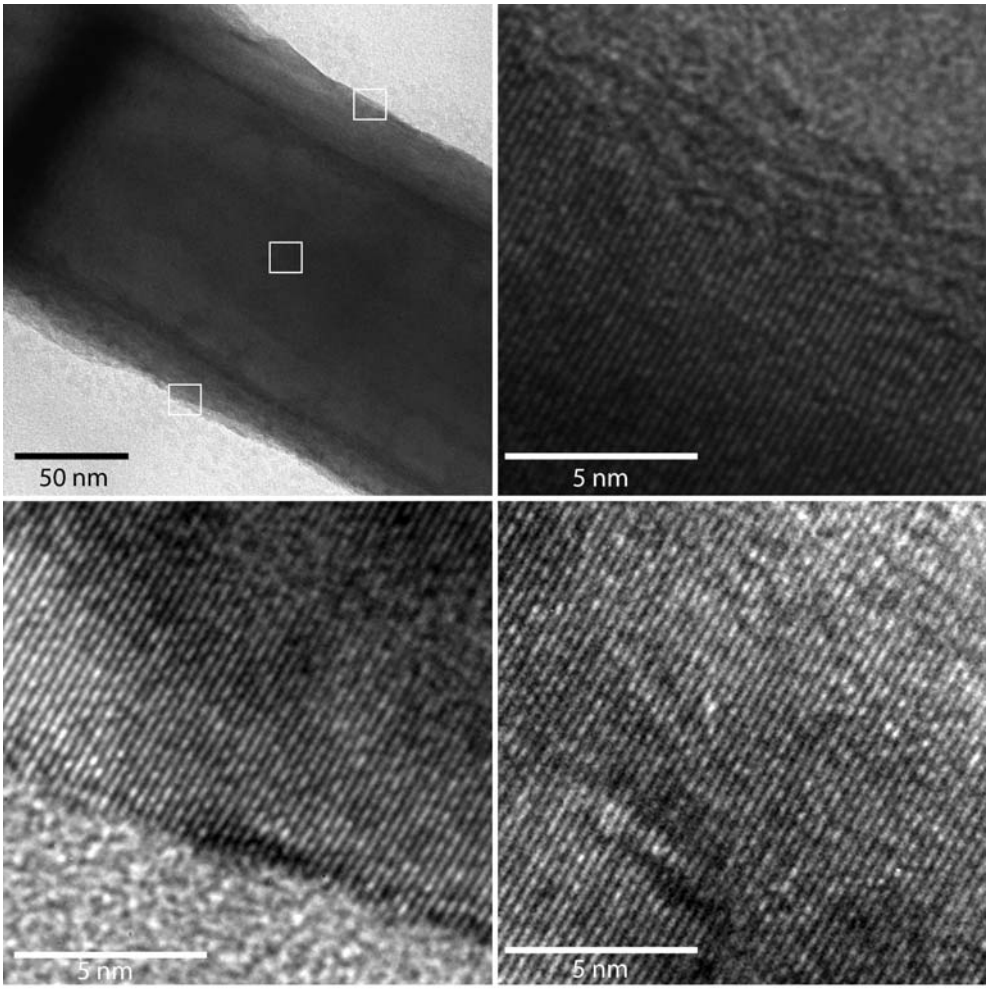

Figure 3.15 (A) TEM image of a ZnO nanowire which has been soaked in a 3.6 g/l aqueous solution of cobalt acetate annealed at 900 ^{0}C for eight hours. (B-D) HR-TEM images of the areas indicated in panel (A) showing the periodicity and orientation of the of the crystal lattice.

In order to examine the cobalt concentration and distribution in the wires, EDX and STEM-HAADF measurements were made. First, untreated ZnO nanowires were examined. Figure 3.16A shows the EDX spectrum obtained from a 300 x 300 nm scan area containing undoped ZnO nanowires. Aside from the obvious zinc and oxygen signals also silicon and copper are detected. The silicon signal can be ascribed to the Si_3N_4 membrane supporting the wires while the copper peak is always present

due to copper components in the TEM. As can be seen in figure 3.16A no cobalt was detected. In order to check for inhomogenities and to determine were in or on the wire the any cobalt is located, EDX line scans across the diameter of the wires have been made (see panel (C)). The integrated peak intensities of the Zn and Co K-shell peaks as a function of spot position are plotted in figure 3.16B. The Zn peak intensity line trace has a shape that is consistent with a hexagonal crossection of the nanowires [61] while the cobalt peak intensity does not rise above the noise level, in agreement with the area measurement shown in panel (A). Figure 3.16C shows the STEM-HAADF image of the nanowires along with an indication of the scan trajectory used in (B).

Next, ZnO nanowires that had been soaked in the cobalt acetate solution and let to dry at room temperature were examined. The EDX spectrum (fig. 3.17A of these wires now clearly shows an additional peak due to transitions of electrons in the cobalt K-shell. The EDX-line traces of the Zn and Co K-shell integrated peak intensities for two different wires are

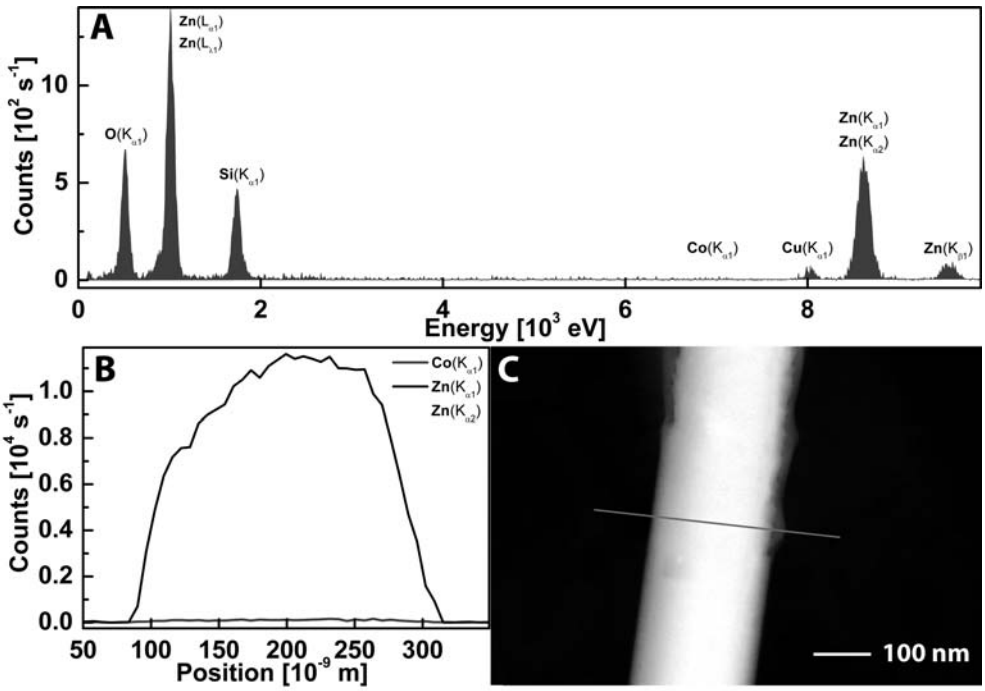

Figure 3.16 (A) EDX spectrum of an as-grown ZnO nanowire aquired with a scan area of ~300x300 nm. (B) Integrated peak intensities as a function of spot position for the Zn(K) and Co(K) peaks. (C) STEM-HAADF image of the nanowire showing the linescan trajectory.

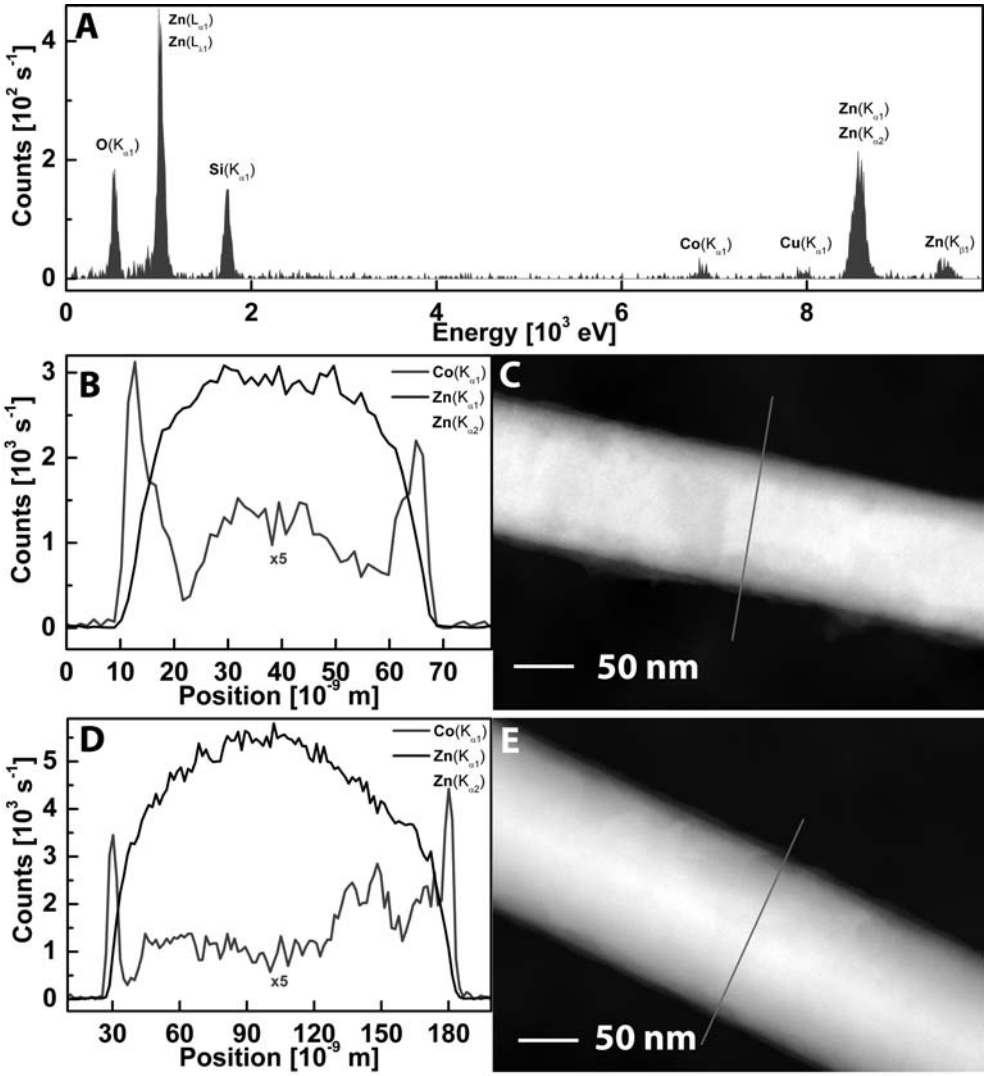

Figure 3.17 (A) EDX spectrum of an ZnO nanowire which has been soaked in a 3.6 g/l aqueousus solution of cobalt acetate. The aquisition area was ~300x300 nm. (B) Integrated peak intensities as a function of spot position for the Zn(K) and Co(K) peaks. (C) STEM-HAADF image of the nanowire showing the linescan trajectory.(D) Integrated peak intensities as a function of spot position for the Zn(K) and Co(K) peaks of a different wire (same treatment). (E) STEM-HAADF image of the nanowire showing the linescan trajectory.

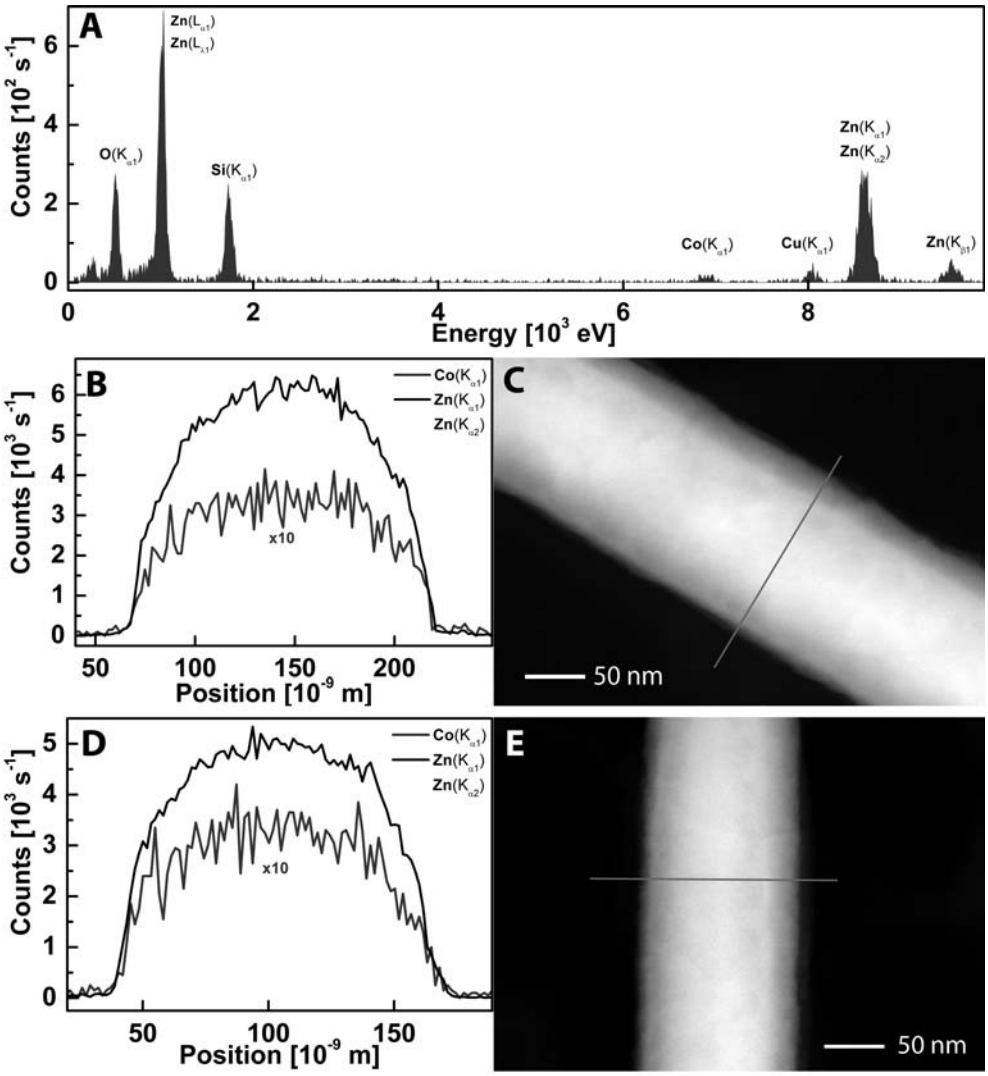

Figure 3.18 (A) EDX spectrum of an ZnO nanowire which has been soaked in a 3.6 g/l aqueous solution of cobalt acetate ans annealed at 900 ^{0}C for eight hours. The aquisition area was ~300x300 nm. (B) Integrated peak intensities as a function of spot position for the Zn(K) and Co(K) peaks. (C) STEM-HAADF image of the nanowire showing the linescan trajectory.(D) Integrated peak intensities as a function of spot position for the Zn(K) and Co(K) peaks of a different wire (same treatment). (E) STEM-HAADF image of the nanowire showing the linescan trajectory.

shown in figure 3.17B&D along with the respective STEM-HAADF images indicating the scan trajectories (fig. 3.17C&E). The integrated Zn peak intensities still follow the expected profile of a nanowire with hexagonal crossection, but the Co peak intensity has a markedly different intensity profile. The highest cobalt concentrations are found at the edges, which indicates that the cobalt is located in a shell around the ZnO nanowire. This is consistent with the results of the reflectance measurements which show that soaking the ZnO nanowires in the cobalt solution does not alter their optical properties so that the ZnO and Co remain in separate phases.

Finally, EDX measurements were performed on ZnO nanowires that have been soaked in the cobalt acetate solution, have been let to dry and have been subsequently annealed at 900°C for eight hours in air. The EDX spectrum of these wires, shown in figure 3.18A, shows that cobalt is still present after the annealing step. An estimation of the Co concentration based on the relative peak intensities of the Co and Zn K lines yields a concentration of 6 %. The EDX-line traces of the Zn and Co K-shell integrated peak intensities for two different wires are shown in figure 3.18B&D along with the respective STEM-HAADF images indicating the scan trajectories (fig. 3.18C&E). From the similarity of the Zn and Co peak intensity line traces it is clear that after the annealing step the cobalt is homogenously distributed inside the wire, in agreement with the reflection data.

3.6.4 Conclusions

In summery, from the presented reflectance data, the X-Ray diffraction data and the EDX line traces it can be concluded that Co^{2+} is successfully substituted into the wurtzite crystal structure of ZnO nanowires. The HR-TEM data shows that the ZnO crystal structure is not changed by the incorporation of Co^{2+} ions. EDX measurements on single wires found that after annealing cobalt is homogeneously distributed through the nanowires with a concentration (~6%) that is in the relevant range for the observation of room temperature ferromagnetism (5%).[50] Moreover, the simplicity and the control over dopant concentration of the dip-dope-anneal procedure allows for the general application of this technique to any structure with a large surface to volume ratio.

References

1 S. Banerjee, A. Dan, and D. Chakravorty, Review Synthesis of conducting nanowires, *J. Mater. Sci.* **37** (2002), p. 4261-4271.
2 R. S. Wagner and W. C. Ellis, VLS mechanism, *Appl. Phys. Lett.* **4** (1964), p. 89-91.
3 Givarzikov, Growth of Whiskers by the Vapor-Liquid-Solid mechanism, *E. Kaldis (Ed.), Current Topics in Materials Science* (1978).
4 Y. Wu and P. Yang, Direct Observation of Vapor-Liquid-Solid Nanowire Growth, *J. Am. Chem. Soc.* **123** (2001), p. 3165-3166.
5 M. S. Gudiksen, J. Wang, and C. M. Lieber, Synthetic Control of the Diameter and Length of Single Crystal Semiconductor Nanowires, *J. Phys. Chem. B* **105** (2001), p. 4062-4064.
6 M. S. Gudiksen and C. M. Lieber, Diameter-Selective Synthesis of Semiconductor Nanowires, *J. Am. Chem. Soc.* **122** (2000), p. 8801-8802.
7 E. P. A. M. Bakkers and M. A. Verheijen, Synthesis of InP Nanotubes, *J. Am. Chem. Soc.* **125** (2003), p. 3440-3441.
8 A. M. Morales and C. M. Lieber, A Laser Ablation Method for the Synthesis of Crystalline Semiconductor Nanowires, *Science* **279** (1998), p. 208-211.
9 K. Hiruma, M. Yazawa, T. Katsuyama, K. Ogawa, K. Haraguchi, M. Koguchi, and H. Kakibayashi, Mocvd, *J. Appl. Phys.* **77** (1995), p. 447.
10 M. H. Huang, Y. Wu, H. Feick, N. Tran, E. Weber, and P. Yang, Catalytic Growth of Zinc Oxide Nanowires by Vapor Transport, *Adv. Mater.* **13** (2001), p. 113-116.
11 K. A. Dick, K. Deppert, T. Mårtensson, B. Mandl, L. Samuelson, and W. Seifert, Failure of the Vapor-Liquid-Solid Mechanism in Au-Assisted MOVPE Growth of InAs Nanowires, *Nanoletters* **5** (2005), p. 761 -764.
12 J. Motohisa, J. Noborisaka, J. Takeda, M. Inari, and T. Fukui, Catalyst-free selective-area MOVPE of semiconductor nanowires on (111)B oriented substrates, *J. Cryst. Growth* **272** (2004), p. 180-185.
13 D. G. Thomas, *Journal de Physique* **15** (1960), p. 86.
14 A. I. Persson, M. W. Larsson, S. Stenstram, B. J. Ohlsson, L. Samuelson, and L. R. Wallenberg, Solid-phase diffusion mechanism for GaAs nanowire growth, *Nature Materials* **3** (2004), p. 677 - 681.
15 K. A. Dick, K. Deppert, L. S. Karlsson, L. R. Wallenberg, L. Samuelson, and W. S. *, A New Understanding of Au-Assisted Growth of III-V Semiconductor Nanowires, *Advanced Functional Materials* **15** (2005), p. 1603-1610.
16 X. Duan and C. M. Lieber, General Synthesis of Compound Semiconductor Nanowires, *Adv. Mater.* **12** (2000), p. 298-302.
17 Z. L. Wang, Zinc oxide nanostructures: growth, properties and applications, *J. Phys.: Condens. Matter* **16** (2004), p. R829–R858.
18 B. F. Levine, A New Contribution to the Nonlinear Optical Susceptibilityi Arising from Unequal Atomic Radii, *Phys. Rev. Lett.* **25** (1970), p. 440 - 443.
19 D. G. Thomas, The exciton spectrum of Zinc Oxide, *J. Phys. Chem. Sol.* **15** (1960), p. 86-96.
20 X. Y. Kong, Y. Ding, R. Yang, and Z. L. Wang, Single-Crystal Nanorings Formed by Epitaxial Self-Coiling of Polar Nanobelts, *Science* **303** (2004), p. 1348-1351.
21 B. Meyer and D. Marx, Density-functional study of the structure and stability of ZnO surfaces, *Phys. Rev. B* **67** (2003), p. 035403.
22 P. Fons, K. Iwata, A. Yamada, K. Matsubara, S. Niki, K. Nakahara, T. Tanabe, and H. Takasu, Uniaxial locked epitaxy of ZnO on the a face of sapphire, *Applied Physical letters* **77** (2004), p. 1801-1803.
23 M. H. Huang, S. Mao, H. Feick, H. Yan, Y. Wu, H. Kind, E. Weber, R. Russo, and P. Yang, Room-Temperature Ultraviolet Nanowire Nanolasers, *Science* **292** (2001), p. 1897-1899.
24 A. Mauger and C. Godart, The magnetic, optical, and transport properties of representatives of a class of magnetic semiconductors: The europium chalcogenides, *Phys. Rep.* **141** (1986), p. 51-176.
25 H. Ohno, Making Nonmagnetic Semiconductors Ferromagnetic, *Science* **281** (1998), p. 951-956.
26 H. Ohno, H. Munekata, T. Penney, S. V. Molnar, and L. L. Chang, Magnetotransport properties of p-type (In,Mn)As diluted magnetic III-V semiconductors, *Phys. Rev. Lett.* **68** (1992), p. 2664-2667.

[27] T. Dietl, H. Ohno, F. Matsukura, J. Cibert, and D. Ferrand, Zener Model Description of Ferromagnitism in Zinc-Blende Magnetic Semiconductors, *Science* **287** (2000), p. 1019-1022.

[28] K. Sato and H. Katayama-Yoshida, Material Design for Transparent Ferromagnets with ZnO-Based Magnetic Semiconductors, *Jpn. J. Appl. Phys., Part 2* **39** (2000), p. L555-L558.

[29] S. J. Pearton, C. R. Abernathy, M. E. Overberg, G. T. Thaler, D. P. Norton, N. Theodoropoulou, A. F. Hebard, Y. D. Park, F. Ren, J. Kim, and L. A. Boatner, Wide band gap ferromagnetic semiconductors and oxides, *J. Appl. Phys.* **93** (2003), p. 1-13.

[30] S. J. Pearton, W. H. Heo, M. Ivill, D. P. Norton, and T. Steiner, Dilute magnetic semiconducting oxides, *Semicond. Sci. Technol.* **R59-R74** (2004), p. R59-R74.

[31] C. Liu, F. Yun, and H. Morkoç, Ferromagnetism of ZnO and GaN: A Review, *Journal of Materials Science: Materials in Electronics* **16** (2005), p. 555-597.

[32] Y. Matsumoto, M. Murakami, T. Shono, T. Hasegawa, T. Fukumura, M. Kawasaki, P. Ahmet, T. Chikyow, S.-y. Koshihara, and H. Koinuma, Room-Temperature Ferromagnetism in Transparent Transition Metal-Doped Titanium Dioxide, *Science* **291** (2001), p. 854-856.

[33] S. B. Ogale, R. J. Choudhary, J. P. Buban*, et al.*, High Temperature Ferromagnetism with a Giant Magnetic Moment in Transparent Co-doped SnO2, *Pyhysical Review Letters* **91** (2003), p. 077205.

[34] K. Ueda, H. Tabata, and T. Kawai, Magnetic and electric properties of transition-metal-doped ZnO films, *Appl. Phys. Lett.* **79** (2001), p. 988-990.

[35] Y. M. Cho, W. K. Choo, H. Kim, D. Kim, and Y. Ihm, Effects of rapid thermal annealing on the ferromagnetic properties of sputtered Zn1–x(Co0.5Fe0.5)xO thin films, *Appl. Phys. Lett.* **80** (2002), p. 3358-3360.

[36] H.-J. Lee, S.-Y. Jeong, C. R. Cho, and C. H. Park, Study of diluted magnetic semiconductor: Co-doped ZnO, **81** (2002), p. 4020-4022.

[37] W. Prellier, A. Fouchet, B. Mercey, C. Simon, and B. Raveau, Laser ablation of Co:ZnO films deposited from Zn and Co metal targets on (0001) Al2O3 substrates, *Appl. Phys. Lett.* **82** (2003), p. 3490-3492.

[38] D. P. Norton, M. E. Overberg, S. J. Pearton, K. Pruessner, J. D. Budai, L. A. Boatner, M. F. Chisholm, J. S. Lee, Z. G. Khim, Y. D. Park, and R. G. Wilson, Ferromagnetism in cobalt-implanted ZnO, *Appl. Phys. Lett.* **83** (2003), p. 5488-5490.

[39] K. Rode, A. Anane, R. Mattana, J.-P. Contour, O. Durand, and R. LeBourgeois, Magnetic semiconductors based on cobalt substituted ZnO, *J. Appl. Phys.* **93** (2003), p. 7676-7678.

[40] Y. W. Heo, M. P. Ivill, D. P. N. K. Ip, S. J. Pearton, J. G. Kelly, R. Rairigh, A. F. Hebard, and T. Steiner, Effects of high-dose Mn implantation into ZnO grown on sapphire, *Appl. Phys. Lett.* **84** (2004), p. 2292-2294.

[41] S.-J. Han, J. W. Song, C.-H. Yang, S. H. Park, J.-H. Park, Y. H. Jeong, and K. W. Rhie, A key to room-temperature ferromagnetism in Fe-doped ZnO: Cu, *Appl. Phys. Lett.* **81** (2002), p. 4212-4214.

[42] P. V. Radovanovic and D. R. Gamelin, High-Temperature Ferromagnetism in Ni2+-Doped ZnO Aggregates Prepared from Colloidal Diluted Magnetic Semiconductor Quantum Dots, *Phys. Rev. Lett.* **91** (2003), p. 157202.

[43] P. Sharma, A. Gupta, K. V. Rao, F. J. Owens, R. Sharma, R. Ahuja, J. M. O. Guillen, B. Johansson, and G. A. Gehring, Ferromagnetism above room temperature in bulk and transparent thin films of Mn-doped ZnO, *Nature Materials* **2** (2003), p. 673 - 677.

[44] H. Saeki, H. Tabata, and T. Kawai, Magnetic and electric properties of vanadium doped ZnO films, *Sol. Stat. Comm.* **120** (2001), p. 439-443.

[45] K. Ando, H. S. Z. Jin, T. Fukumura, M. Kawasaki, Y. Matsumoto, and H. Koinuma, Large magneto-optical effect in an oxide diluted magnetic semiconductor Zn1–xCoxO, *Appl. Phys. Lett.* **78** (2001), p. 2700-2702.

[46] T. Fukumura, Z. Jin, M. Kawasaki, T. Shono, T. Hasegawa, S. Koshihara, and H. Koinuma, Magnetic properties of Mn-doped ZnO, *Appl. Phys. Lett.* **78** (2001), p. 958-960.

[47] S. W. Jung, S.-J. An, G.-C. Yi, C. U. Jung, S.-I. Lee, and S. Cho, Ferromagnetic properties of Zn1–xMnxO epitaxial thin films, *Appl. Phys. Lett.* **80** (2002), p. 4561-4563.

[48] Z. Jin, T. Fukumura, M. Kawasaki, K. Ando, H. Saito, T. Sekiguchi, Y. Z. Yoo, M. Murakami, Y. Matsumoto, T. Hasegawa, and H. Koinuma, High throughput fabrication of transition-metal-doped epitaxial ZnO thin films: A series of oxide-diluted magnetic semiconductors and their properties, *Appl. Phys. Lett.* **78** (2001), p. 3824-3826.

[49] G. Lawes, A. S. Risbud, A. P. Ramirez, and R. Seshadri, Absence of ferromagnetism in Co and Mn substituted polycrystalline ZnO, *Phys. Rev. B* **71** (2005), p. 045201.

[50] M. Venkatesan, C. B. Fitzgerald, J. G. Lunney, and J. M. D. Coey, Anisotropic Ferromagnetism in Substituted Zinc Oxide, *Phys. Rev. Lett.* **93** (2004), p. 177206.

[51] S. Ramachandran, A. Tiwari, and J. Narayan, Zn0.9Co0.1O-based diluted magnetic semiconducting thin films, *Appl. Phys. Lett.* **84** (2004), p. 5255-5257.

[52] K. J. Kim and Y. R. Park, Spectroscopic ellipsometry study of optical transitions in Zn1–xCoxO alloys, *Appl. Phys. Lett.* **81** (2002), p. 1420-1422.

[53] D. A. Schwartz, N. S. Norberg, Q. P. Nguyen, J. M. Parker, and D. R. Gamelin, Magnetic Quantum Dots: Synthesis, Spectroscopy, and Magnetism of Co2+- and Ni2+-Doped ZnO Nanocrystals, *J. Am. Chem. Soc.* **125** (2003), p. 13205 -13218.

[54] K. R. Kittilstved, D. A. Schwartz, A. C. Tuan, S. M. Heald, S. A. Chambers, and D. R. Gamelin, Direct Kinetic Correlation of Carriers and Ferromagnetism in Co2+: ZnO, *Phys. Rev. Lett.* **97** (2006), p. 037203.

[55] K. R. Kittilstved, W. K. Liu, and D. R. Gamelin, Electronic structure origins of polarity-dependent high-TC ferromagnetism in oxide-diluted magnetic semiconductors, *Nature Materials* **5** (2006), p. 291-297.

[56] J. M. D. Coey, M. Venkatesan, and C. B. Fitzgerald, Donor impurity band exchange in dilute ferromagnetic oxides, *Nature Materials* **4** (2005), p. 173-179.

[57] X. Duan, Y. Huang, Y. Cui, J. Wang, and C. M. Lieber, Indium phosphide nanowires as building blocks for nanoscaleelectronic and optoelectronic devices, *Nature* **409** (2001), p. 66-69.

[58] M. S. Gudiksen, L. J. Lauhon, J. Wang, D. C. Smith, and C. M. Lieber, Growth of nanowire superlattice structures for nanoscale photonics and electronics, *Nature* **415** (2002), p. 617-620.

[59] N. Skold, L. S. Karlsson, M. W. Larsson, M.-E. Pistol, W. Seifert, J. Tragardh, and L. Samuelson, Growth and Optical Properties of Strained GaAs-GaxIn1-xP Core-Shell Nanowires, *Nanoletters* **5** (2005), p. 1943-1947.

[60] M. H. M. v. Weert, O. Wunnicke, A. L. Roest, T. J. Eijkemans, A. Y. Silov, J. E. M. Haverkort, G. W. t. Hooft, and E. P. A. M. Bakkers, Large redshift in photoluminescence of p-doped InP nanowires induced by Fermi-level pinning, *Appl. Phys. Lett.* **88** (2006), p. 043109.

[61] P. V. Radovanovic, C. J. Barrelet, S. Gradecak, F. Qian, and C. M. Lieber, General Synthesis of Manganese-Doped II-VI and III-V Semiconductor Nanowires, *Nanoletters* **5** (2005), p. 1407 -1411.

[62] J. S. Kulkarni, O. Kazakova, and J. D. Holmes, Dilute magnetic semiconductor nanowires, *Appl. Phys. A* **85** (2006), p. 277-286.

[63] J. B. Cui and U. J. Gibson, Electrodeposition and room temperature ferromagnetic anisotropy of Co and Ni-doped ZnO nanowire arrays, *Appl. Phys. Lett.* **87** (2005), p. 133108.

[64] B. D. Yuhas, D. O. Zitoun, P. J. Pauzauskie, R. He, and P. Yang, Transition-Metal Doped Zinc Oxide Nanowires, *Angew. Chem.* **45** (2006), p. 420-423.

[65] A. Rahm, E. M. Kaidashev, H. Schmidt, M. Diaconu, A. Poeppl, R. Boettcher, C. Meinecke, T. Butz, M. Lorenz, and M. Grundmann, Growth and characterization of Mn- and Co-doped ZnO nanowires, *Micro chemica acta* **156** (2007), p. 21–25.

[66] J.-J. Wu, S.-C. Liu, and M.-H. Yang, Room-temperature ferromagnetism in well-aligned Zn1- xCoxO nanorods, *Aplied Physics Letters* **85** (2004), p. 1027-1029.

[67] This cobalt concentration seems a factor 10 to 100 to low when compared to other studies.

[68] D. Kouyate, J. C. Ronfard-Haret, P. Valat, J. Kossanyi, U. Mammel, and D. Oelkrug, Quenching of zinc oxide photoluminescence by d- and f-transition metal ions, *J. Lumin.* **46** (1990), p. 329-337.

[69] H. A. Weakliem, Optical Spectra of Ni2 + , Co2 + , and Cu2 + in Tetrahedral Sites in Crystals, *J. Chem. Phys.* **36** (1962), p. 2117-2140.

[70] P. Koidl, Optical absorption of Co2+ in ZnO, *Phys. Rev. B* **15** (1977), p. 2493 - 2499.

[71] H.-J. Schulz and M. Thiede, Optical spectroscopy of 3d7 and 3d8 impurity configurations in a wide-gap semiconductor (ZnO:Co,Ni,Cu), *Phys. Rev. B* **35** (1987), p. 18 - 34.

[72] R. S. Anderson, Lattice-Vibration Effects in the Spectra of ZnO:Ni and ZnO:Co, *Phys. Rev.* **164** (1967), p. 398 - 405.

Chapter 4

Increase of the photoluminescence intensity of InP nanowires by photo-assisted surface passivation

As-grown single crystal InP nanowires, covered with a In_2O_3 surface oxide, show a low photoluminescence efficiency that strongly varies from wire to wire. In this chapter it is shown that the luminescence efficiency of single-crystal InP nanowires can be improved by photo-assisted wet chemical etching in a butanol solution containing HF and the indium-coordinating ligand tri-octyl-phosphineoxide (TOPO). Electron-hole photo generation, electron scavenging and oxidative dissolution combined with surface passivation by the indium-coordinating ligand are essential elements to improve the luminescence efficiency. Time-traces of the luminescence of surface-passivated wires show strong oscillations resembling the on-off blinking observed with single quantum dots. These results reflect the strong influence of a single or a few non-radiative recombination centre(s) on the luminescence properties of an entire wire.

4.1 Introduction

One of the future applications of semiconducting nanowires is the use in miniaturized opto-electronic devices and photonic circuits.[1-3] The large length-to-diameter aspect ratio enables the wires to be contacted by standard lithographic procedures, [4] incorporating them into an electronic or opto-electronic device. For instance, an electroluminescent device, based on a p-n junction formed by two crossed InP nanowires has been reported.[2] Furthermore, nanowires with a built-in p-n junction [3] or a zero-dimensional quantum [5, 6] dot have been synthesized. Such systems are very promising for nanoscale opto-electronic devices with novel functions, such as the emission of polarized photons and single-photon pulses. For such applications it is required that the semiconductor nanowires have a reasonable electron-to-photon or photon-to-photon luminescence quantum yield. Semiconductor nanowires can be grown as (nearly) defect-free single crystals.[7] They, however, possess a relative large surface-to-volume ratio. As a consequence, excitons can decay non-radiatively via electronic surface states, leading to a poor photoluminescence quantum yield. In this respect, III-V semiconductors are much more critical than II-V semiconductors such as ZnO. Non-radiative recombination at the III-V (oxide) surface is very efficient, while the bulk exciton diffusion length is large (100nm-1μm). Hence, photogenerated excitons can easily find a non-radiative recombination centre and, consequently the photoluminescence quantum yield is very low (<1%).

InP, the semiconductor of interest in this chapter, has a direct band gap of 1.38 eV at room-temperature. Light-emitting diodes based on macroscopic p-n junctions of InP (as base material) show a charge carrier-to-photon conversion efficiency of nearly 100 %.[8] In strong contrast, an InP nanowire with an intra wire p-n junction shows an efficiency of only ~0.1%.[3] In principle, non-radiative recombination can occur at the surface or in the bulk. For instance, Au atoms can be incorporated into the lattice during growth of the wire, leading to a trap level located at 0.55 eV below the conduction band.[9] The solubility of Au atoms in InP is however very low ($6*10^{14}/cm^3$) [9] leading to an average of 17 Au atoms per wire which indicates that in the case of wires it cannot be the main origin of non-radiative recombination. The disappointingly low quantum yield is in line with the results obtained with suspensions of spherical InP nanocrystals (so-called quantum dots) where the photoluminescence efficiency of the as-prepared colloidal quantum dots is below 1 %. However, Mičic *et al.*

reported an effective surface passivation procedure based on the use of a solution of butanol / HF / tri-octyl-phosphineoxide (TOPO) which increased the photoluminescence quantum yield up to 40 %.[10] Recently, Talapin *et al.* showed convincingly that the surface passivation of InP nanocrystals is photochemical in nature.[11] The surface passivation requires oxidative dissolution of InP surface molecules, induced by photogenerated valence holes, together with the action of HF and the TOPO capping molecules. Although the molecular mechanism of the surface passivation is not understood in detail, it was reported that the increased photoluminescence is directly related to a decrease of unpassivated P-sites and an increase of In-TOPO sites at the nanocrystal surface. [12]

It is obvious that the photoluminescence and electroluminescence quantum yield of InP nanowires must be considerably increased before study of their fundamental photophysics and their application in opto-electronic devices becomes feasible. In the present study, we have investigated whether the light-stimulated surface passivation procedure, proven to efficiently increase the photoluminescence quantum yield of InP quantum dot suspensions, can also be used for InP nanowires. There are however some differences between wires and colloidal nanocrystals which must be considered here. First, the length of the InP nanowires that we have studied exceeds the exciton Bohr-radius in InP (≈ 20nm) by at least one order of magnitude, while the diameter of the wires is between 30 and 60 nm. Since quantum-confinement effects could only be expected in these wires for diameters below 15 nm, [13] such effects can be neglected here. But importantly, highly polarized photoluminescence has been observed from these one-dimensional structures.[14] In addition, several independent excitonic states can coexist in a single wire, unlike the case of an InP quantum dot. This is important for the photophysics and photochemical surface passivation of the InP nanowires under study. Second, the absolute number of surface atoms of a single-crystal InP wire is much larger than that of an InP quantum dot. Thus, the probability that a surface defect, inducing non-radiative recombination, is present on a wire is considerably larger than on a quantum dot. All excitons located within a distance shorter than the diffusion length (which can be 100 nm or more) from a surface defect will be annihilated non-radiatively. In other words, a single defect site can strongly affect the luminescence properties of a single wire. It is thus an intriguing question as to whether single nanowires can be efficiently passivated against non-radiative recombination. In this respect, the case of a nanowire is similar to that of a quantum-dot solid, where due

to efficient energy transfer, a single non-radiative center can quench the luminescence. [15]

Here, a study of the light-stimulated surface passivation and photoetching of InP nanowires is presented. We have studied the photoluminescence spectra of individual InP nanowires deposited on Si/SiO_2 substrates and APTES (3-aminopropyl-triethoxysilane) covered substrates before and after photoetching in butanol solutions of HF/TOPO. In addition, we have imaged individual InP nanowires and recorded the evolution of the photoluminescence during the process of photoetching (at high HF concentration) or photo-stimulated surface passivation (at low HF concentration) using non-polarized and linearly polarized excitation light.

4.2 Experimental

Materials. Chlorobenzene (99.9%; HPLC grade), tri-octyl-phosphineoxide (TOPO; 99%), butanol (99.8%; HPLC grade) and 3-aminopropyl-triethoxysilane (APTES; 99%) were purchased from Aldrich. Hydrofluoric acid (40% in water) was purchased from Riedel-Dehaen. Hydrogen peroxide (30% in water) was purchased from Merck.

Nanowire synthesis and substrate preparation. The synthesis of n-type InP nanowires is described in section 3.3. The-as grown nanowires were dispersed in chlorobenzene by ultra-sonification and deposited onto bare or APTES-functionalized Si/SiO_2 substrates. Markers on the substrates, defined by e-beam lithography, allowed repeated identification of individual nanowires. For in situ micro-luminescence measurements a drop of the etching solution (5 g/l TOPO, 0.01%-20% HF in butanol) [16] was placed on top of the nanowire containing substrate, which was located inside a Teflon holder fitted with a sapphire window.

Micro-luminescence setup. Single-wire photoluminescence measurements were performed using a linearly polarized 200 mW 457nm DPSS laser (Melles Griot) directly coupled into a Leica DM/LM upright microscope equipped with 5x-100x dry BF/DF objectives to have a resulting magnification of 50-1000x. A $\lambda/2$ wave retardation plate was placed directly after the laser to enable rotation of the light polarization in the specimen plane of the microscope. The photoluminescence signal of the nanowires was split-off using a long-pass dichroic mirror and blocking filter. This signal was then coupled into an optical fiber, dispersed by a grating and recorded by a CCD array spectrometer. Images were acquired

by placing a CCD camera (Nikon DM12) directly on top of the microscope. A schematic of the micro-luminescence setup is shown in figure 4.1.

Ex-situ photoetch setup. White light from a 300W Hg/Xe lamp (Oriel) was focused by a lens and deflected downward by a mirror into an open 50 ml polypropylene vial which was placed on top of a magnetic stirrer.

TEM. Nanowires were deposited on a 10 nm thick Si_3N_4 membrane, such that specific wires could be studied before and after the etching experiment. TEM images were obtained with a Philips Tecnai 12 operating at 120 kV.

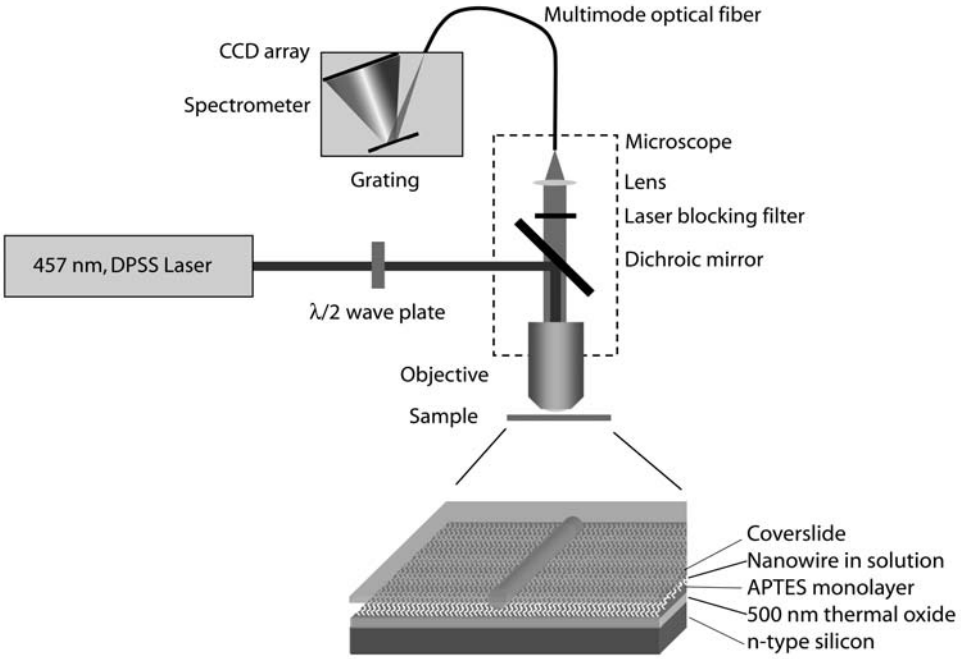

Figure 4.1 Experimental setup used for the photo-etching and passivation of InP nanowires.

4.3 Results and discussion

4.3.1 Photoluminescence spectra of as-grown and surface-passivated InP nanowires

Figure 4.2A shows typical PL spectra of an as-grown InP wire and of the same wire after 25 minutes of etching in a 0.1% HF/ 5 g/l TOPO/butanol solution using defocused laser light (442 W/cm^2). Photo-stimulated passivation of this wire resulted in a tenfold increase of the PL intensity (see below). Figures 4.2B and 4.2C show the dark-field optical image of the wire and the resulting PL image after photoetching. These show that the photoluminescence intensity is uniform along the length of the wire. The maximum of the photoemission of the as-grown wire is noticeably blueshifted (59 meV) with respect to that of a bulk InP:Se crystal recorded with the same apparatus. After photoetching the maximum is further blue-shifted by 40 meV. We should note here that the diameter of the wire was about 50 nm, excluding quantum confinement as the origin of the blue-shifts. Another striking feature is that the emission spectra of the wire are considerably broader (FWHM= 107 meV ($4k_bT$) than that of a macroscopic InP crystal (FWHM= 58 meV), where broadening is caused by electron-phonon interactions and shallow defects. Spectra measured on at least 50 other wires, with diameters over 40 nanometers, also showed the blueshift and the broadening of the photoemission. We attribute the additional

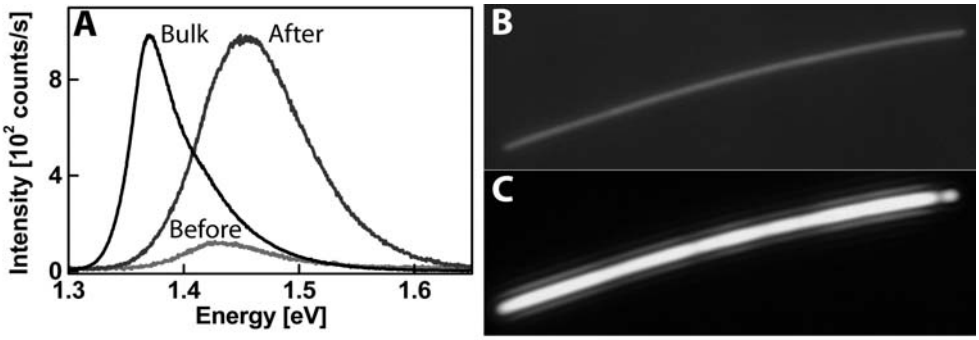

Figure 4.2 (A) Photoluminescence spectra of a single nanowire before and after photoetching with defocused laserlight (442 W/cm^2) for 25 minutes in a 0.1% HF / 5 g/l TOPO/butanol solution. For comparison, the normalized PL spectrum of a macroscopic InP:Se crystal is plotted. Figures (B) and (C) show the dark-field optical and photoluminescence images of this wire, respectively.

broadening with respect to a macroscopic crystal and the blue-shift of the PL spectra of the nanowires to Coulomb interactions of the exciton electron and hole with (fractional) charges or dipoles distributed on the surface of the nanowire. This conclusion is based on theoretical work by Franceschetti and Zunger, who showed that the sum of the Coulomb interactions between a given spectator charge and the electron and hole of the exciton is non-zero.[17] As a result, a blue or red shift of the exciton energy can occur depending on the effective masses of the electron and hole. In the case of InP dots, the hole is more localized than the electron; the blue-shift of the spectra is explained by the presence of an effective positive charge density on the surface of the InP nanowires. The broadening of the spectra of the wires with respect to those of macroscopic single crystals is then explained by (temporal or stationary) spatial inhomogeneities in the effective charge density on the surface of the wire. Excitons at different positions in the wire experience a variable Coulomb potential leading to a variation in the energy of the emitted photons. We remark that, broadening of the spectra of CdSe nanorods and concomitant red-shifts have been reported recently, and have been explained in a similar way.[18]

4.3.2 Photo-assisted surface passivation of InP nanowires in butanol solutions of HF/TOPO

We used a procedure for light-stimulated surface passivation of InP nanowires which is very similar to that used by Talapin *et al.*[11] for the photoetching and passivation of colloidal InP quantum dots (see figure 4. 3). We recorded the PL spectra of 25 individual nanowires before any (chemical) treatment. The wires were dispersed onto a Si/SiO_2 substrate. The as-grown wires were covered with a thin native oxide layer which forms due to contact with air. Another part of the as-grown nanowires was transferred from the growth substrate into a transparent vial containing a 0.1% HF/butanol solution. After 20 mins, this solution was diluted with butanol and TOPO was added to give a final concentration of 0.01% HF and 50 g/l TOPO. This procedure ensured that the surface oxide was chemically etched away before the photoetching began. The solution was stirred and illuminated by a 300 Watt mercury/xenon lamp in ambient for 6 hours. The solution was then dropcast onto a Si/SiO_2 substrate, washed with methanol and dried. PL spectra of 25 randomly chosen nanowires were recorded under precisely the same conditions of focused laser light intensity as for the as-grown wires.

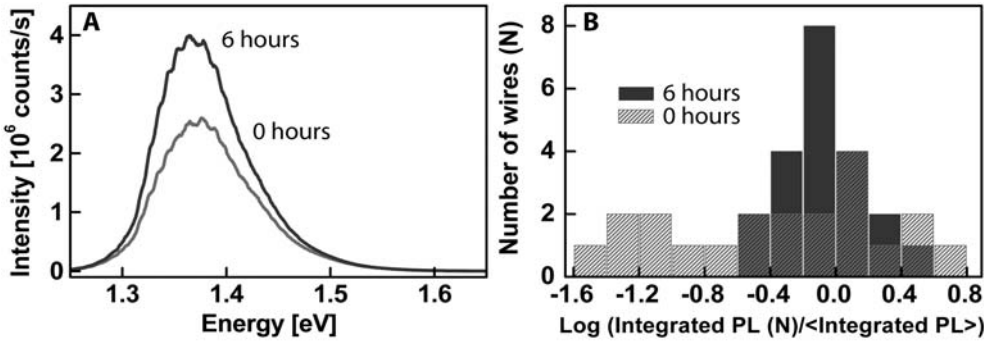

Figure 4.3 (A) Averaged photoluminescence intensity of an ensemble of individually measured nanowires before and after 6 hours of photoetching in a 0.01 % HF/ 50 g/l TOPO/butanol solution under illumination of a 300W mercury/xenon lamp. 25 wires were measured. The two highest and lowest intensities were disregarded. (B) A histogram of the luminescence intensity of individual wires: on the x-axis, the logarithm of the integrated luminescence intensity normalized to the ensemble average is used.

The shape of the emission spectra of individual InP wires is very similar for all wires (see section 4.3.1). However, the absolute photoluminescence intensity varies strongly from wire to wire (see fig. 4.3B). This is very typical, both for the as-grown and for the photoetched wires, although the dispersion in luminescence intensity is smaller for the etched wires. We have estimated the PL Quantum Yield of the single untreated wires, by comparison of the emission intensity with that of an InP single crystal. We found that the PL QY of the single wires varied between 0.01% and 1 % typically when the QY of the InP single crystal was taken as 100%.
In order to check whether photoetching has led to an improved photoluminescence we took the average (after removal of the two highest and lowest PL intensities) of the photoluminescence spectra of 25 nanowires before and after photoetching, see figure 4.3B. We etched several labeled InP nanowires ranging in diameter from 26 nm to 50 nm with the same setup for 6 hours using the same etching solutions and found no appreciable reduction of the diameter of the wire from TEM analysis (see fig. 4.4). This is in line with the results of Talapin *et al.* with InP quantum dots which show that the removal of semiconductor material in this solution is very slow. On average, there is an increase in the luminescence intensity (under the same excitation intensity) by a factor of 1.5 after 6 hours of photoetching. We repeated this experiment with a series of wires from another growth run and found a similar increase in the

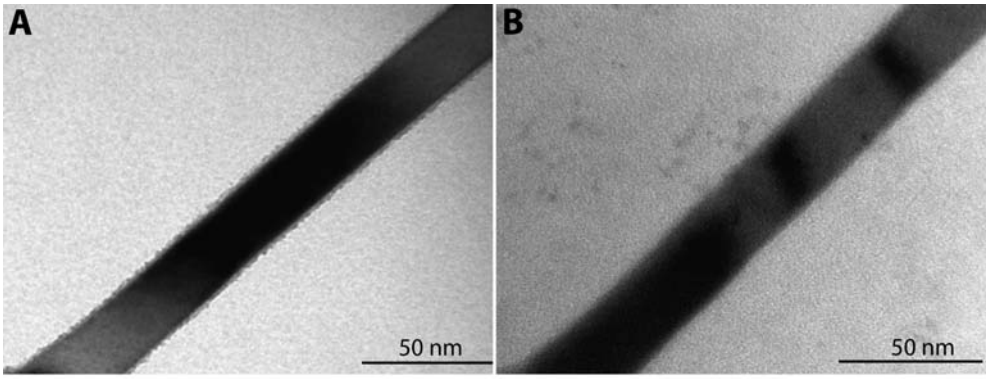

Figure 4.4 TEM images of a nanowire (A) before (d=27.8±0.9 nm) and (B) after (d =27.1±0.2 nm) 6 hours of illumination with a 300 W mercury/xenon lamp in a 0.01% HF/50 g/l TOPO/butanol solution.

luminescence intensity: the intensity increased with a factor of three, averaged over 25 nanowires (see figure 4.5). Thus, prolonged photoetching with very low HF concentrations leads to a moderate increase in the averaged photoluminescence efficiency without the noticeable removal of the semiconductor material.

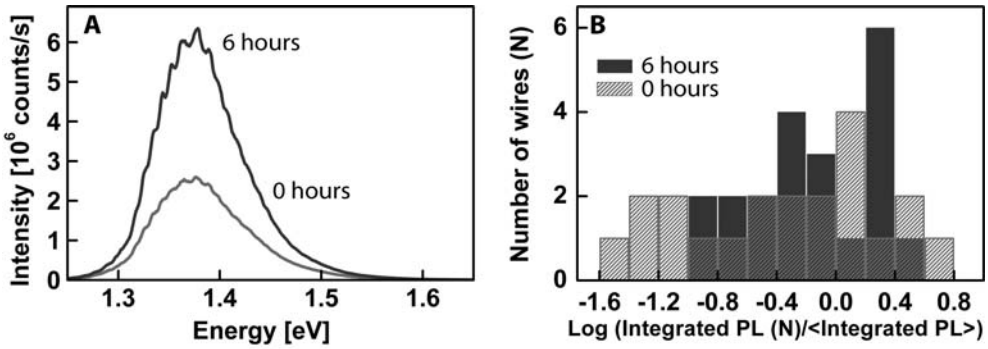

Figure 4.5 (A) Averaged photoluminescence intensity of an ensemble of individually measured nanowires before and after 6 hours of photoetching in a 0.01 % HF/ 50 g/l TOPO/butanol solution under illumination of a 300W mercury/xenon lamp. 25 wires were measured. The two highest and lowest intensities were disregarded. (B) A histogram of the luminescence intensity of individual wires: on the x-axis, the logarithm of the integrated luminescence intensity normalized to the ensemble average is used.

4 3.3 Photoselectivity of etching and surface passivation

We have further checked the nature of the processes (photochemical or chemical ?) that occur when an etching solution is applied to InP wires, by comparing wires kept in the etching solution under focused laser light with wires in the dark. The as-grown nanowires are covered with an In_2O_3 and/or a mixed In/P oxide that has to be removed before InP is etched and TOPO chemisorption can take place. Oxide removal occurs by chemical HF etching in the dark. In order to be able to see changes within a reasonable measurement time, we used focused laser light and increased the HF concentration of the etching solution to between 0.1 and 20 % HF in TOPO/butanol.

Figure 4.6A shows a low magnification dark-field optical image of two InP nanowires in 20% HF/butanol solution on an APTES-covered SiO_2 substrate. Only wire I was exposed to the focused laser spot (15.9 kW/cm^2).

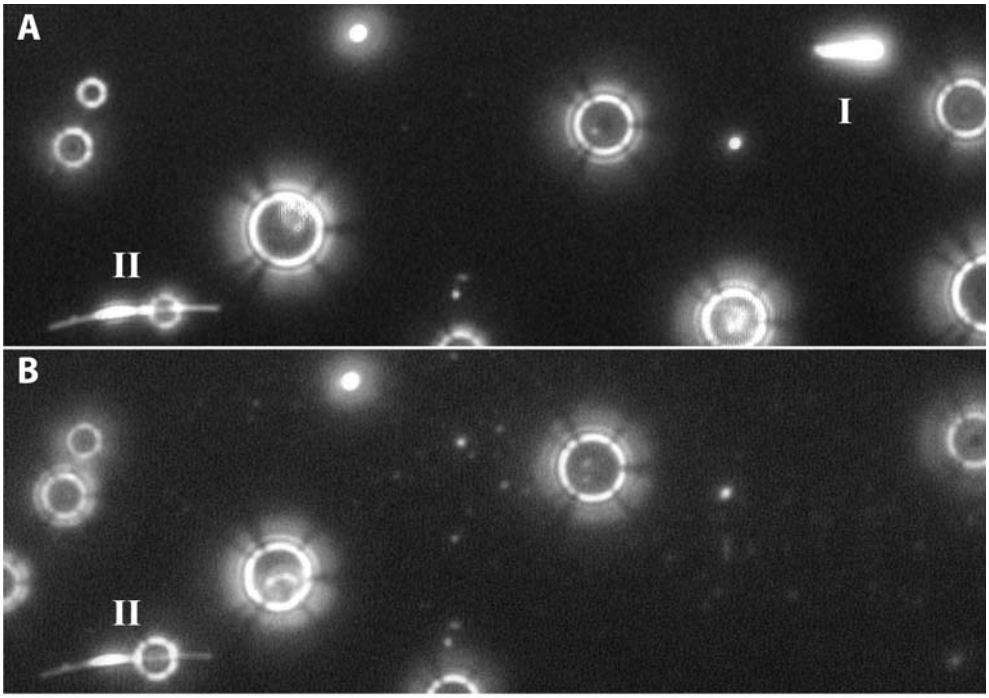

Figure 4.6 (A) Optical dark-field image of two nanowires on an APTES covered SiO_2 substrate immersed in a 20% HF/butanol solution. (B) After illuminating the upper wire with a focused laser beam (15.9 kW/cm^2) for 3 minutes. The bright circles in the pictures are caused by gas bubbles in the solution.

As can be seen in figure 4.6B, after three minutes of illumination, wire I was etched away completely whilst wire II remained unchanged in the dark. This clearly demonstrates that within the time-frame of the experiment InP wires do not etch in HF/butanol solutions in the dark, but that photogenerated holes are required to dissolve the wire. This agrees with the observation of Talapin *et al*. who reported that the etching of colloidal InP quantum dots in a HF/TOPO/butanol solution is photochemical. Thus, photogenerated conduction electrons are scavenged by oxygen present in the solution under ambient conditions, while the holes are consumed in oxidative dissolution of InP:

$$6\hbar\nu \rightarrow 6\ h^+ + 6\ e^- \qquad (1a)$$

$$InP_{surf} + 6\ h^+ \rightarrow In(III)_{sol} + P(III)_{sol} \qquad (1b)$$

$$3/2\ O_2 + 6\ H^+ + 6\ e^- \rightarrow 3\ H_2O \qquad (1c)$$

Photoetch experiments have shown that the intensity of the photoemission of the InP wire did not increase in oxygen-free etch solutions; instead the emission intensity decreased, probably due to the chemical dissolution of the surface oxide layer. The photoetching was enhanced by adding H_2O_2 as an electron scavenger to the solution. This shows that photogenerated conduction electrons must be scavenged fast enough to prevent electron-hole recombination. Furthermore, illumination of an individual nanowire in a butanol solution without HF or without TOPO had no effect or a negative effect on the photoluminescence intensity, showing that HF and TOPO are essential ingredients for photo-assisted surface passivation.

4.3.4 Polarization anisotropy of etching and surface passivation

The absorption and emission of light by sub 100 nm diameter InP nanowires is strongly anisotropic;[14] photons polarized with their electric field vector parallel to the long axis of the wire are preferentially absorbed or emitted. Figure 4.7A shows an optical dark-field image two InP nanowires mutually oriented at almost ninety degrees. If the wires are excited with supra-bandgap laser light which has its polarization at 45 degrees to the long axis of each wire, both wires luminesce equally (figure 4.7B). If however the excitation polarization is parallel to the lower wire (figure 4.7C) this wire luminesces maximally while the upper (bent) nanowire only shows luminescence in the part that still has an orientation

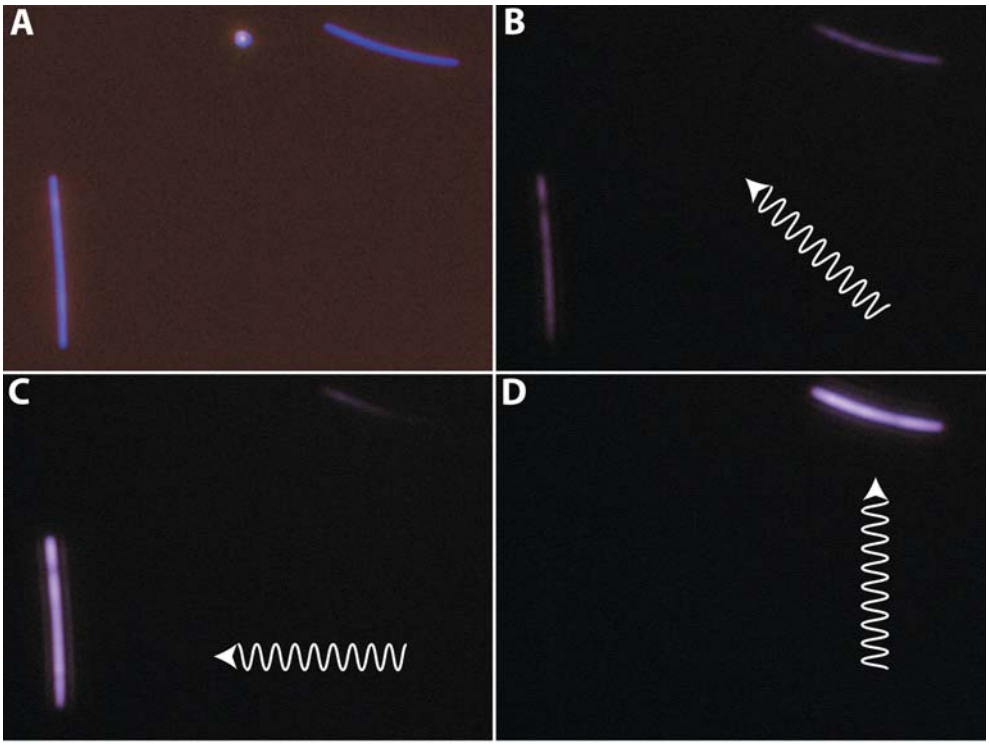

Figure 4.7 (A) Optical dark-field image of two perpendicularly oriented InP nanowires. (B-C) Photoluminescence images of the nanowires shown in panel A with the excitation polarization (white arrow) at 45 degrees to each nanowire's long axis (B), with the excitation polarization parallel to the lower nanowire (C) and with the excitation polarization parallel to the upper nanowire (D).

component in the direction of the polarization. With the excitation polarization parallel to the upper wire (figure 4.7D), only this wire luminesces. The detection in this experiment was insensitive to polarization so that this experiment shows that significantly less excited electrons and holes are created inside a nanowire for excitation with the polarization perpendicular to the nanowire long axis.

This anisotropy can be exploited in the photoetching process. In figure 4.8A, two wires are shown; wire I is oriented nearly perpendicular to

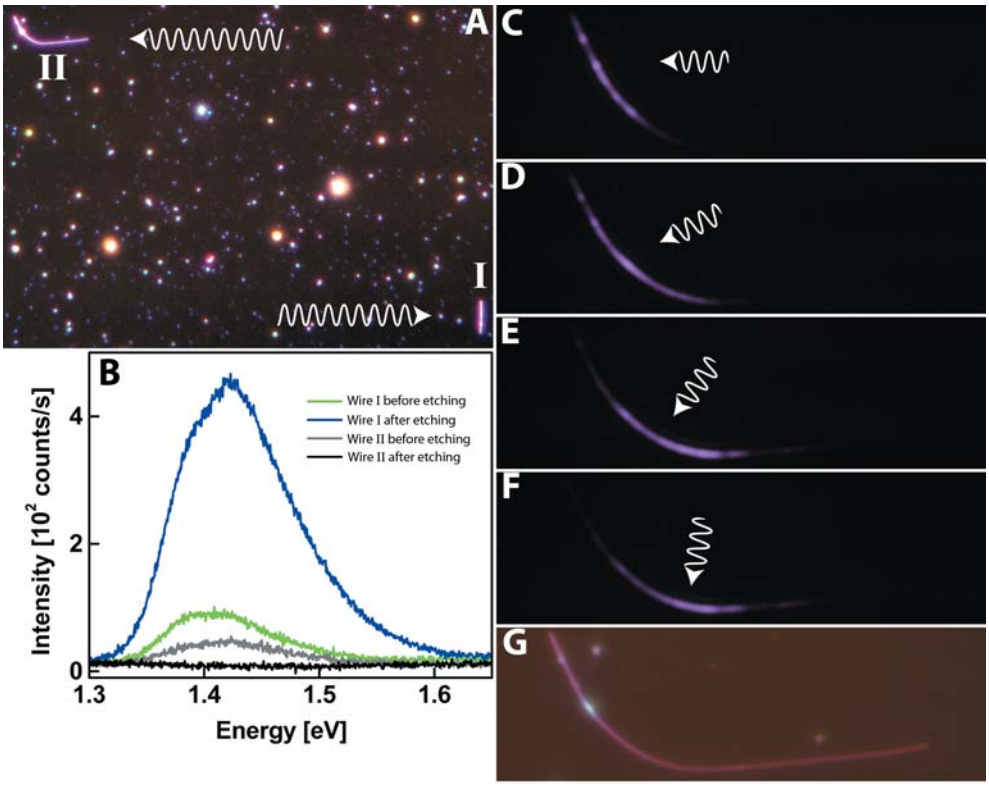

Figure 4.8 (A) Photoluminescence spectra of wire I and II before (green and grey line respectively) and after (blue and black line respectively) photoetching by a defocussed laser spot (442 W/cm^2) with the electric field vector parallel to wire I. The spectra were acquired with excitation polarization parallel to each wire axis. (B): Dark- field optical image of the two perpendicularly oriented nanowires. (C-F): Photoluminescence images of wire II after photoetching, showing only light emission from the bent part of the wire which could absorb the polarized light during photoetching. (Compare with the dark-field image G). For images C to F the excitation polarizationis as indicated by the arrows. Excitation with horizontal polarization resulted in no detectable light emission.

wire II which has a bent part. Before starting the photoetching, luminescence spectra of both wires were taken with the electric-field vector of the incident laser light parallel to the principal axis of the wire. The photoetching was carried out in a 0.1% HF/5 g/l TOPO/butanol solution with a defocused laser spot (442 W/cm^2) that illuminated both wires. During photoetching, the electric field vector was parallel to wire I. After 25 minutes of illumination, the sample was rinsed with butanol and dried. The spectra of the individual nanowires were taken, again with the light polarized parallel to the wire's long axis (figure 4.8B). The photoluminescence intensity of wire I is increased with a factor of five due to photoetching. In contrast, the photoluminescence of wire II, which was illuminated with light perpendicular to the wire axis, has not improved. Only the bent part of the wire, which could absorb light during the photoetching, luminesces (figures 4.8C-F). The degradation of the photoluminescence is probably due to chemical removal of the surface oxide which passivates the surface to some extent. Hence, the anisotropic light absorption enables the selective etching and passivation of a wire by a proper choice of the polarization of the incident light.

4.3.5 Time-evolution of the photoluminescence of individual wires during photoetching

In an attempt to get more insight into the mechanism of photo-assisted surface passivation and etching and the observed variation in photoluminescence properties we followed the photoetching of individual InP nanowires in-situ. To enable direct PL measurement and imaging of the same wire before, during and after photoetching we deposited the as-grown nanowires on an APTES-covered SiO_2 substrate. This protected the SiO_2 substrate from HF attack and prevented the wires from drifting. Figure 4.9A-B shows the time traces of the PL intensity of two nanowires being photoetched. In both cases the intensity shows an initial decrease. In the case shown in figure 4.9A this decrease was by a factor of 10 between 0 and 400 s, after which the PL intensity remained low for a considerable time between 400 and 1100 s. Remarkably, after 1100 s of photoetching, the photoluminescence increased suddenly by over three orders of magnitude with respect to the initial intensity and then slowly decayed to an intensity, which is still two orders of magnitude higher than that of the initial situation. We attribute the initial decrease of the photoluminescence to the removal of the passivating oxide layer leaving a poorly passivated surface.

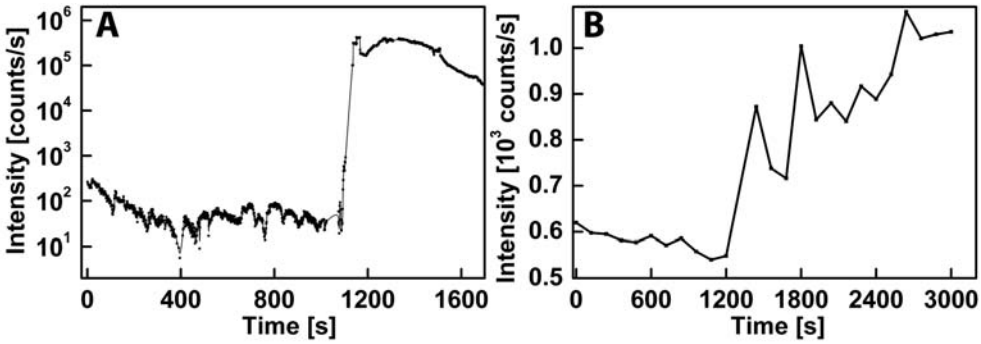

Figure 4.9 (A) Time evolution of the photoluminescence from a single nanowire during photoetching with a focused laserspot (15.9 kW/cm²) in a 2.5% HF 0.3 g/l TOPO/butanol solution, (B) during photoetching with a focused laserspot (795 W/cm²) in a 0,01% HF 0,01% H_2O_2 6,6 g/l TOPO/butanol solution.

This experiment was repeated with other wires and all showed the characteristic initial decrease and subsequent increase in luminescence intensity; an example with a small increase in the PL intensity is shown in figure 4.9B. Additionally we found that the maximum of the luminescence spectrum was blue-shifted by some tens of meV simultaneously with the increase of the photoluminescence. We studied the stability of the luminescence of wires, which showed a considerable increase in their photoluminescence after the photoetching under intense illumination (laser spot 15.9 kW/cm²). We measured the time evolution of the photoluminescence of photo-passivated wires after washing and drying under ambient conditions. It was commonly found that the luminescence slowly decreased initially, but became constant at relatively low luminescence intensity. Further research is needed to investigate the origin of this moderate degradation. We observed remarkable photoluminescence intensity fluctuations from single wires on the seconds time scale (figure 4.10). We note that these fluctuations were only observed with photoetched wires; a typical time trace of a non-etched wire is also show in figure 4.10 (black trace). The fluctuations in the intensity were correlated to shifts in the peak position. The photoluminescence did not jump between the "off" and "on" state as observed with individual quantum dots, but the amplitude of the jumps varied between 0 and 50 % of the total intensity . This implies that a non-radiative surface centre influences a part of the wire (within the exciton diffusion length). Excitons generated in this part recombine non-radiatively, while the excitons generated in another region lead to luminescence. In this view, the fluctuations in the luminescence

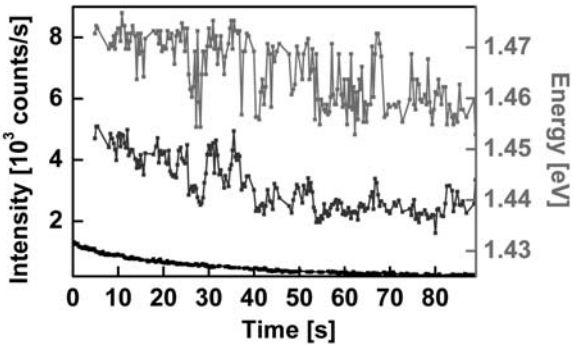

Figure 4.10 Fluctuations of the PL intensity (upper curve) and the peak position (middle curve) of a photoetched nanowire measured under excitation with focused laser light in ambient. For comparison, the PL intensity evolution of an unetched wire is also plotted (lower curve).

intensity reflect the spatially random generation/recombination of excitons. Another possibility is that, under intense laser illumination, defects are randomly generated and annealed.

4.4 Conclusions

In this chapter it has been shown that InP nanowires can be passivated by a photoetching process to considerably increase the luminescence efficiency. The enhancement of the photoluminescence varies strongly from wire to wire, but enhancement by one order of magnitude can often be achieved. The process can be tuned, such that the surface is passivated with improved photoluminescence without a noticeable reduction of the wire diameter or the wire can be etched away completely. Moreover, by the use of polarized light, wires can be photoetched and passivated selectively by proper orientation of the polarization vector. For instance, this could be used to remove wires with an undesirable orientation for device applications. Photoetched wires that are passivated with TOPO-ligands do not show a completely stable luminescence under intense excitation in ambient. The time traces show interesting fluctuations in intensity similar to the on-off fluctuations observed with quantum dots.

References

[1] K. Hiruma, M. Yazawa, T. Katsuyama, K. Ogawa, K. Haraguchi, M. Koguchi, and H. Kakibayashi, Mocvd, *J. Appl. Phys.* **77** (1995), p. 447.

[2] X. Duan, Y. Huang, Y. Cui, J. Wang, and C. M. Lieber, Indium phosphide nanowires as building blocks for nanoscaleelectronic and optoelectronic devices, *Nature* **409** (2001), p. 66-69.

[3] M. S. Gudiksen, L. J. Lauhon, J. Wang, D. C. Smith, and C. M. Lieber, Growth of nanowire superlattice structures for nanoscale photonics and electronics, *Nature* **415** (2002), p. 617-620.

[4] S. J. Tans, A. R. M. Verschueren, and C. Dekker, Room-temperature transistor based on a single carbon nanotube, *Nature* **393** (1998), p. 49-52.

[5] M. T. Björk, B. J. Ohlsson, T. Sass, A. I. Persson, C. Thelander, M. H. Magnusson, K. Deppert, L. R. Wallenberg, and L. Samuelson, One-dimensional heterostructures in semiconductor nanowhiskers, *Appl. Phys. Lett.* **80** (2002), p. 1058-1060.

[6] Y. Wu, R. Fan, and P. Yang, Block-by-Block Growth of Single-Crystalline Si/SiGe Superlattice Nanowires, *Nanoletters* **2** (2002), p. 83-86.

[7] U. krishnamachari, *Aplied Physics Letters* **85** (2004), p. 2077-2079.

[8] D. A. Steigerwald, J. C. C. Bhat, D., R. M. Fletcher, M. O. Holcomb, M. J. Ludowise, P. S. Martin, and S. L. Rudaz, Illumination with solid state lighting technology, *IEEE J. Quantum Electron.* **8** (2002), p. 310-320.

[9] V. Parguel, P. N. Favennec, M. Gauneau, Y. Rihet, R. Chaplain, H. L'Haridon, and C. Vaudry, Gold diffusion in InP, *J. Appl. Phys.* **62** (1987), p. 824-827.

[10] O. I. Micic, J. Sprague, Z. Lu, and A. J. Nozik, Highly efficient band-edge emission from InP quantum dots, *Appl. Phys. Lett.* **68** (1996), p. 3150-3152.

[11] D. V. Talapin, N. Gaponik, H. Borchert, A. L. R. Haase, and H. Weller, Etching of Colloidal InP Nanocrystals with Fluorides: Photochemical Nature of the Process Resulting in High Photoluminescence Efficiency, *J. Phys. Chem. B* **106** (2002), p. 12659-12663.

[12] S. Adam, C. McGinley, T. Moller, D. V. Talapin, H. Borchert, M. Haase, and H. Weller, Photoemission study of size selected InP nanocrystals: the relationship between luminescence yield and surface structure, *The european Physical Journal D* **24** (2003), p. 373-376.

[13] M. S. Gudiksen, J. Wang, and C. M. Lieber, Size-Dependent Photoluminescence from Single Indium Phosphide Nanowires, *J. Phys. Chem. B* **106** (2002), p. 4036-4039.

[14] J. Wang, M. S. Gudiksen, X. Duan, Y. Cui, and C. M. Lieber, Highly Polarized Photoluminescence and Photodetection from Single Indium Phosphide Nanowires, *Science* **293** (2001), p. 1455-1457.

[15] C. R. Kagan, C. B. Murray, M. Nirmal, and M. G. Bawendi, Electronic Energy Transfer in CdSe Quantum Dot Solids, *Phys. Rev. Lett.* **76** (1996), p. 1517-1520.

[16] We advise those working with HF solutions to familiarize themselves with its inherent hazards.

[17] A. Franceschetti and A. Zunger, Optical transitions in charged CdSe quantum dots, *Phys. Rev. B* **62** (2000), p. R16 287-R16 290.

[18] J. Müller, J. M. Lupton, A. L. Rogach, J. Feldmann, D. V. Talapin, and H.Weller, Monitoring Surface Charge Movement in Single Elongated Semiconductor Nanocrystals, *Phys. Rev. Lett.* **93** (2004), p. 167402-1.

Chapter 5

Exciton-Polaritons Confined in a ZnO nanowire Cavity

Semiconductor nanowires of high purity and crystallinity hold promise as building blocks for miniaturized opto-electrical devices. Using scanning-excitation single-wire emission spectroscopy, with a laser or electron beam as a spatially resolved excitation source, we observe standing-wave exciton-polaritons in ZnO nanowires at room temperature. The Rabi-splitting between the polariton branches is more than 100 meV indicative for huge light-matter interaction. Our results suggest that the remarkable sub-wavelength guiding in ZnO nanowires, reported before, is mediated by exciton-polaritons. The dispersion curve of 'light' is substantially modified due to strong light-matter interaction; this will have to be taken into account in future nanophotonic circuitry.

5.1 Introduction

Chemically prepared semiconductor nanowires form a class of very promising building blocks for miniaturized optical and electrical devices [1]. They possess a high degree of crystallinity and the lattice orientation is often well defined with respect to the nanowire geometry [2]. Semiconductor nanowires offer the possibility of photon–exciton conversion and interaction: a key aspect in quantum optics and opto-electrical applications. Strong exciton-photon interaction is complementary to surface plasmon-photon interaction, which has been studied extensively in view of sub-wavelength optics. For instance, light-emitting diodes based on crossed p-type and n-type nanowires [3] and wire-integrated p-n junctions have been reported[4], as well as nanowire lasers [5] and field-selective photon detectors.[6] It is well known that optical properties can be affected by the enhanced electromagnetic field due to standing waves in optical resonators. In semiconductor microcavities containing a quantum dot, strong exciton-photon coupling, leading to exciton-polaritons with an avoided crossing of the photon and exciton dispersion curves, has been reported.[7,8,9] The normal-mode cavity splitting, in this field commonly referred to as the Rabi splitting, was at most 10 meV.

Crystalline ZnO forms an intriguing system with regard to the interaction between excitons and photons. In Wurtzite ZnO (symmetry group C_{6v}) the valence band is split into three due to the crystal field and spin orbit coupling [10,11]. The three resulting excitons are labeled A, B and C and have at cryogenic temperatures energies and transverse-longitudinal splittings of 3.375eV (1.5-2 meV), 3.385eV (10-12 meV) and 3.425eV (10-12 meV) respectively [12,13,14,15] The bandgap continuum amounts to 3.437 eV which leads to exciton binding energies of 62, 52 and 12 meV for the A, B and C excitons respectively [10,12] . The symmetry of the valence bands is still under debate and is either A-Γ_9, B-Γ_7, C- Γ_7 [12,10,16] like in other C_{6v} semiconductors such as CdS or is A-Γ_7, B-Γ_9, C-Γ_7 [17,18,19, 20] while the conduction band has Γ_7 symmetry [11]. Either way, the symmetry of the excitons is not important in our experiment due to the complicated nature of the modes present in the nanowire, interacting with these excitons. (e.g. TM or HE modes, also see chapter 2) and the fact that we use non-resonant excitation.

The high exciton binding energies lead to the stability of the A and B excitons at room temperature, which is needed for strong light-matter interaction. Furthermore, the exciton transitions have a large oscillator

strength, as evidenced by their large transverse-longitudinal splitting, which should favor light-matter interaction. Unfortunately, due to the severe broadening of the resonances and interaction with phonons at room-temperature, no data exists on the energetic positions of the resonances at room temperature. To obtain the room temperature resonance energies, the resonance energies are shifted by the same amount as the shift of the bandgap from 3.437eV at 4K to 3.370 eV at room temperature. Hence, we estimate that the A, B and C resonances at room-temperature are at 3.309 eV, 3.315 eV and 3.355 eV respectively. Figure 5.1 shows the normalized room-temperature photoluminescence spectra of a non-oriented array of ZnO nanowires. Two emissions can be seen: a broad emission in the green spectral range caused by a transition from the conduction band to a deep hole trap [21] and secondly a more narrow emission in the UV spectral range which is exciton related [19]. The peak in the excitation spectrum of the green emission (black line) shows that indeed excitons exist at room-temperature at 3.31 eV or 60 meV below the band edge at 3.37 eV.

Exciton-photon coupling has been shown to affect the light dispersion relation in macroscopic bulk ZnO [22]. This has led to a strong interest in the optical properties of ZnO up to date. The longitudinal-transverse splitting in macroscopic ZnO is two orders of magnitude larger than in GaAs [15], presently the material of choice for the study of strong light-matter interaction. On thin films of ZnO, exciton-polaritons have been studied by their photoluminescence spectrum up to 250 K [14]. It was anticipated that strong-light matter interaction should prevail in ZnO photonic nanostructures due to a combination of photon confinement and strong exciton absorption [23,24]. In this chapter we report extremely strong exciton-photon coupling in ZnO nanowires at room temperature. We collect emission spectra of single wires upon scanning a focused laser or electron excitation spot along the wire. We report considerably enhanced

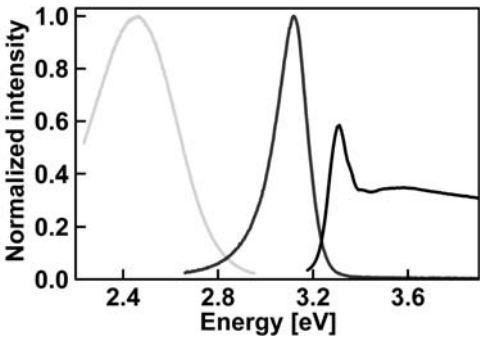

Figure 5.1 Room temperature normalized emission and excitation spectra of a non-oriented array of ZnO nanowires showing defect related emission in the green spectral region and exciton related emission in the UV spectral region. The solid black line is the excitation spectrum of the green emission showing the excistance of excitons at room temperature as a peak at 60 meV below the bandgap of 3.37 eV.

excitation probabilities at the wire ends for two groups of polariton modes, separated by a gap between 60 – 164 meV, depending on the wire. Our results thus provide strong evidence for a giant Rabi-splitting. This strong exciton-photon interaction determines the polaritonic dispersion curve in the near UV and might explain the surprising sub-wavelength guiding that has been reported previously and which is also observed with the wires used in this study (see chapter 1).

5.2 Experimental

The ZnO nanowires were grown on a sapphire substrate with the vapor-liquid-solid method at 920° C using gold as a catalyst [25,26]. Details of the synthesis can be found in chapter 3. After growth, the wires were dispersed onto a 20 nm thick silicon nitride membrane. In order to unravel the mode-like properties of the excitation, single wires with known geometry have to be investigated. We therefore performed two-photon excitation luminescence spectroscopy, Cathodo-Luminescence spectroscopy (CL) and Transmission Electron Microscopy (TEM) on each nanowire under study. About ten ZnO wires of length varying between 1 and 10 μm along the c-axis, and diameter between 100 and 300 nm were investigated.

In scanning-excitation emission spectroscopy, the total single wire emission is detected as a function of the position of the excitation spot on the wire. The experimental setup is shown in figure 5.2A. Near infrared laserlight (Spectra-Physics Tsunami Ti:Saffire Laser, λ=700-950 nm, 100 fs pulse duration, 60 MHz repetition rate) was focused to a diffraction limited laser spot on the sample by a microscope objective (40X, N.A. 1.3). The excitation spot had a spatial resolution of 400 nm due to the use of two-photon excitation and could be scanned over the sample in 50 nm steps. The emission image from the entire sample was collected by the same objective and was split-off by a dichroic mirror. The various wavelengths of the emission image were dispersed by a double prism. A UV-Vis-IR achromatic lens then translated the direction of light to a position on the CCD array. This detection scheme is insensitive to the polarization of the emitted light.

The orientation of the nanowire with respect to the excitation beam is shown in figure 5.2B. The excitation wave vector was mainly perpendicular to the crystal c-axis with only a small component along the c-axis due to the focusing of the laser beam. The E-field vector could be

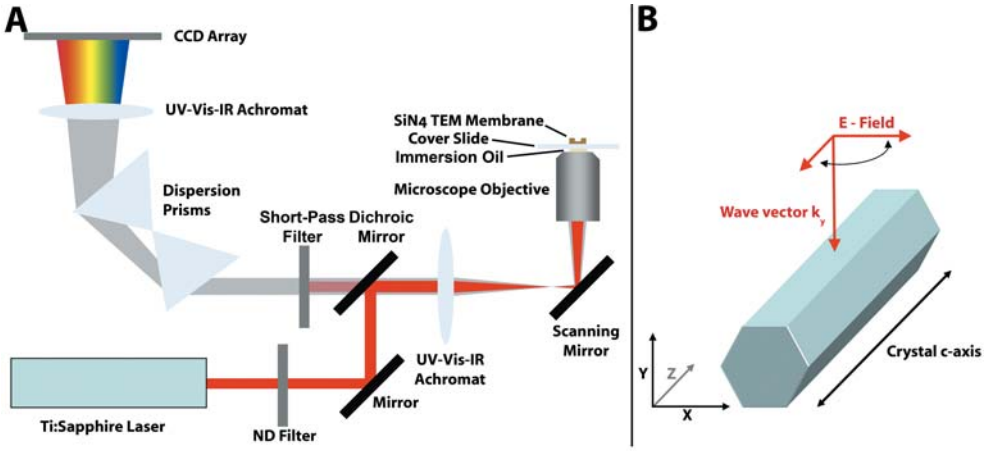

Figure 5.2(A) Scanning-excitation luminescence spectroscopy setup. (B) Experimental geometry. The wire was excited mainly perpendicular to its long axis. The electric field could be rotated so that it was either paralell or perpendicular to the wires long axis.

varied between directions perpendicular and parallel to the crystal c-axis by rotation of the sample.

Cathodo-luminescence experiments were performed at the FOM-Institute for Atomic and Molecular Physics (Amolf) within a FEI SEM fitted with a Gatan CL detection system. The experimental configuration is shown in figure 5.3: A focused electron beam with a spatial resolution of 40 nm is scanned over the wire. A parabolical mirror with a hole for the electron beam collects any emission from the image plane and projects this emission onto the entrance slit of a grating spectrometer fitted with a Photo Multiplier Tube (PMT) for the detection of photons. The orientation of the nanowire with respect to the excitation beam is similar to that in figure 5.2B with the main difference that the electron excitation beam is not polarized so that no effect of the wire orientation on the excitation can be expected.

Figure 5.3 Schematic of the cathodoluminescence setup at Amolf.

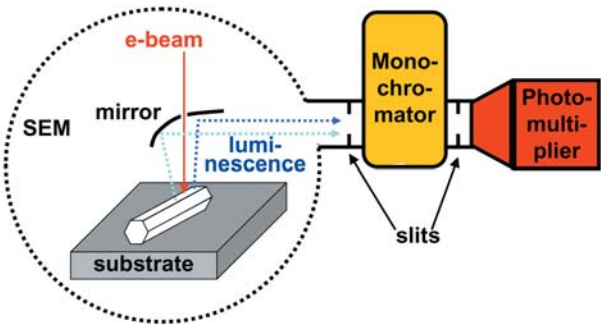

5.3 Results.

5.3.1 Two photon excitation, luminescence and second harmonic generation.

Before spatially resolved data is presented it is useful to discuss the average, spatially unresolved, photon emission properties of individual ZnO nanowires. The data presented in figures 5.4 and 5.5 is spatially averaged by adding all the spectra obtained at each excitation spot and dividing by the number of excitation spot positions. Figure 5.4A shows the emission spectrum of an individual ZnO nanowire which is excited with near infrared photons with an energy of 1.72 eV. The wire shows emission at the doubled excitation energy of 3.44 eV. This peak can be attributed to second harmonic generation [27]. Second order diffraction of the excitation beam in the detection system can be excluded as the source of this peak due to the use of a double prism configuration as the dispersing method. There is also strong luminescence peak at around 3.26 eV which, for bulk ZnO, has been ascribed to exciton related emission [28] or emission from the lower polariton branch [14]. The broad green luminescence peak ($\hbar\omega_e$ < 2.8 eV)

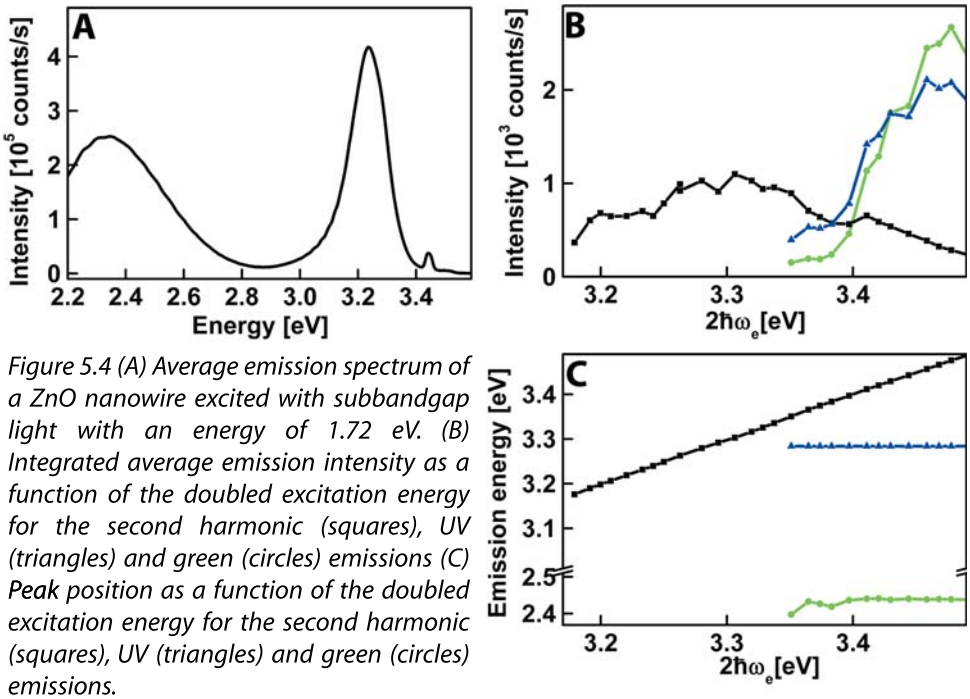

Figure 5.4 (A) Average emission spectrum of a ZnO nanowire excited with subbandgap light with an energy of 1.72 eV. (B) Integrated average emission intensity as a function of the doubled excitation energy for the second harmonic (squares), UV (triangles) and green (circles) emissions (C) Peak position as a function of the doubled excitation energy for the second harmonic (squares), UV (triangles) and green (circles) emissions.

arises from trapping of the excitons in a defect center [21]. The laser used in these experiments can be tuned to variable photon energy (1.36 eV < $\hbar\omega$ < 1.77 eV) i.e. below or above the bandgap of ZnO when using two photon excitation. Figure 5.4B shows the integrated emission intensity for the second harmonic (squares), UV (triangle up) and green (circles) emission as a function the doubled excitation energy $2\hbar\omega$. When $2\hbar\omega$ is below the typical exciton transition energy in a ZnO crystal, around 3.31 eV (also see chapter 2), only SH emission is observed. However, when $2\hbar\omega$ is resonant with, or higher in energy than the exciton transitions, the wire also luminesces in the UV and the green. In addition it can be seen that the second harmonic intensity is maximal in the excitonic region which points to resonance enhanced second harmonic generation [29]. (also see figure 5.5B). From a plot of the emission peak position versus the doubled excitation energy (Figure 5.4C) one can differentiate between luminescence processes and excitation correlated emissions. Upon varying the excitation energy, luminescence processes are expected to remain at fixed energetic positions while any second harmonic emission should follow the doubled excitation energy. It can be seen in Figure 5.4C that the UV and green emissions remain at fixed energetic positions while the second harmonic emission linearly follows the doubled excitation energy.

The SH, UV and green emissions are coupled: their intensity depends strongly and in the same way on the polarization of the excitation beam with respect to the crystal c-axis (long axis) of the ZnO wire (figure 5.5A). The wire was rotated with respect to the laser polarization so that the

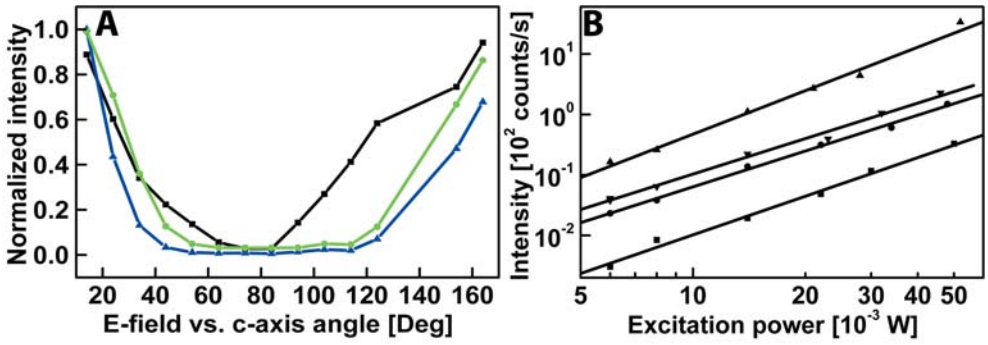

Figure 5.5 (A) Integrated second harmonic (squares), UV (triangles) and green (circles) emission of a ZnO nanowire as a function of the angle between the polarization of the exciting light and the wire's long axis . (B) Integrated second harmonic intensity as a function of the excitation power for excitation with photon energies of 1.77 eV (squares), 1.72 eV (circles), 1.64 eV (triangle up) and1.55 eV (triangle down).

angle between the long axis of the wire and the electric field of the laser beam varied from 20 to 165 degrees. The SH (squares), UV (triangle up) and green (circles) emissions are all maximum at the smallest angles between the E-vector and the wire's long axis and are all nearly minimum at an angle of around 90 degrees. It is known that due to their large length to diameter ratio nanowires interact anisotropically with the electric field of light. (see for instance Chapter 4 section 3.4) [6]. It can be expected that this "antenna effect" also plays a role here although based on the wire diameter used for this measurement (~105 nm) one would not expect such a strong on-off effect as is observed (compared to InP nanowires). An additional effect accounting for the large on-off ratio could be the crystal orientation dependent efficiency of second harmonic generation in ZnO. In bulk ZnO crystals, SH generation is more efficient in the c-axis direction then in other directions due to the presence of dipoles along the c-axis [27]. The intensity of the luminescence emissions decays more steeply with increasing angle than the SH emission. This is consistent with the view that the observed SH is a manifestation of the excitation source and that the observed luminescence is a secondary process involving loss of energy by e.g. phonon emission.

Under resonant excitation the SH emission intensity of a single wire exhibits a power law dependence on the primary excitation intensity with a power markedly above two. In figure 5.5B excitation power dependent SH intensities are plotted for excitation at 1.77 eV (squares), 1.72 eV (circles), 1.64 eV (triangles up) and 1.55 eV (triangles down). While the power dependencies at 1.77eV, 1.72eV and 1.55eV exhibit a slope of nearly 2, as expected for a two photon process, the slope of the power dependency at 1.64eV is 2.48. This indicates an additional non-linearity in the exciton generation via SH reabsorption or direct two-photon absorption [30].

In summery, ZnO wires can be excited by near infrared laser light with $\hbar\omega \geq \frac{1}{2}(E_{exciton})$ resulting in green and UV luminescence and second harmonic generation. The luminescence spectrum is very similar to that obtained with direct UV excitation, or with an electron beam. If $\hbar\omega < \frac{1}{2}(E_{exciton})$, only second harmonic generation is observed which follows the expected quadratic dependence on the intensity of the excitation. The second harmonic has the highest absolute intensity when it is generated at the exciton energy and at that energy it has a power law dependence on the primary excitation intensity with a power markedly above two. The emissions are sensitive to the polarization of the excitation light: Highest emission intensity is obtained for excitation with the exciting electric field parallel to the wire's long axis.

5.3.2 Spatially resolved excitation single-wire emission spectroscopy

In macroscopic crystals and microcavities exciton-polaritons are conventionally studied with angle-dependent reflection or transmission spectroscopy at angles between parallel and perpendicular to the length direction of the crystal or cavity [12,31]. These methods are however not possible with single wires forming cavities of sub-wavelength diameter. In the presented experiment, we collect the emitted spectra of a single nanowire upon scanning with a spatially resolved excitation spot (400 nm spatial resolution, 50 nm steps) in a grid over the wire. The total single-wire emission spectrum was measured for each position of the excitation spot. After acquisition of the data, software allowed for the definition of a line trace along the length of the wire, giving the total wire emission spectrum for each excitation position. It must be stressed that in this manner no spatial information about the emission is obtained and that the detected emission not necessarily originates at he excitation position (also see chapter 1). The difference in excitation energy $2\hbar\omega$ and emitted energy $\hbar\omega_e$ is lost in phonons. We assume that this loss does not depend on the position of excitation. The spatial pattern of the single-wire emission at given emission energy $\hbar\omega_e$ thus represents the spatially resolved probability of exciting modes of energy $\hbar\omega_e$ ± 5 meV (10 meV bandwidth of the detection system) in a given ZnO nanowire.

Such excitation patterns, for $2\hbar\omega$ excitation above the exciton energy and selected emission energies, are presented in figures 5.6B-E&G. Qualitatively similar results on two other wires are shown in figures 5.7B-E &G and 5.8B-D&F. The average emission spectra of these wires are shown by the black lines in figs. 5.6A, 5.7A and 5.8A whereas TEM images of these wires are shown in figures 5.6F, 5.7F and 5.8E. Surprisingly, we observe a strong enhancement of the excitation rate of UV emission (3.25 – 3.40 eV) at the ends of the wire with respect to the centre. The enhancement is also found for light emission at lower energy (2.7 – 3.2 eV) on condition that the two-photon excitation is resonant with or has a higher energy than the exciton transitions.

Trivial causes or experimental artifacts, such as a more favorable in-coupling of the excitation beam at the wire ends, can be excluded for a number of reasons. First, if the two-photon excitation $2\hbar\omega$ is below the exciton transitions, only SH emission is observed, with a single-wire intensity that is independent on the position of the excitation spot. In-coupling effects at the wire ends would have resulted in enhancement of

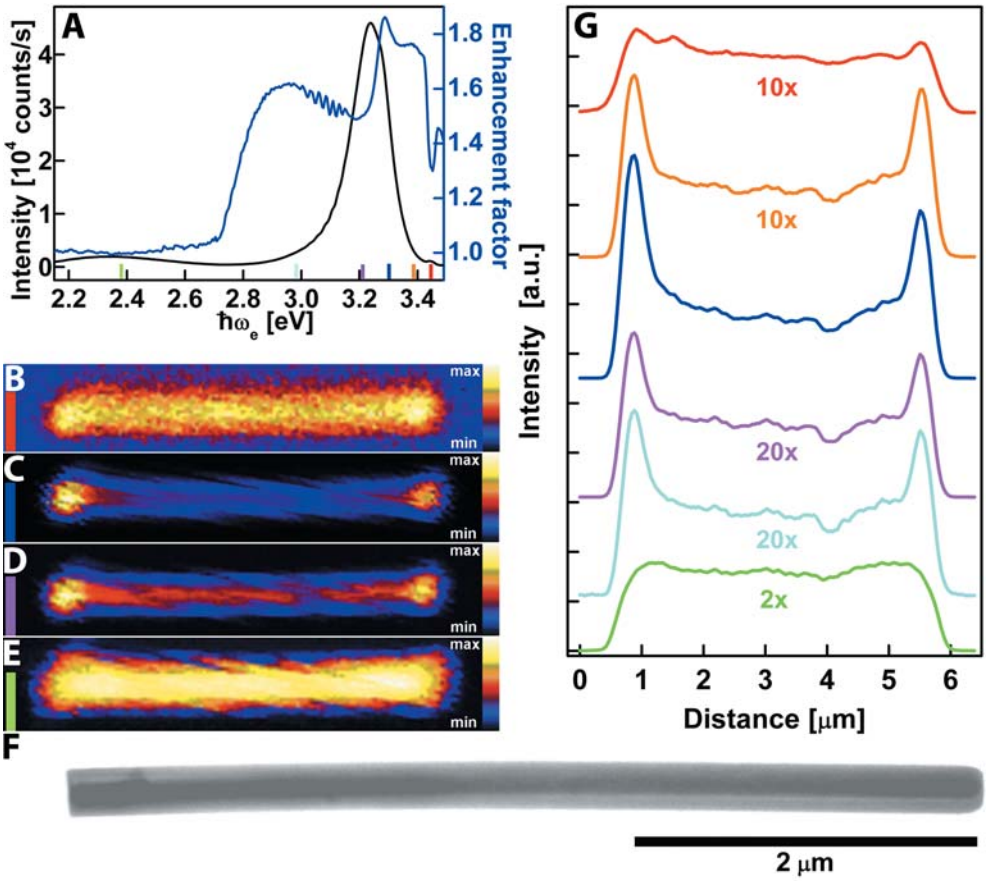

Figure 5.6 (A) (Black line) average photoluminescence spectrum of a ZnO nanowire for excitation with subbandgap light (1.72 eV). (Blue line) enhancement spectrum. (B-E) Spatially resolved excitation images taken at the emission energies indicated in panel (A) by the colored bars. (F) TEM image of the investigated wire. The wire had a length of 5.19 μm and a diameter of 273 nm. (G) Excitation line traces along the length of the wire (c-axis) at emission energies indicated by the colored bars in panel A. The profiles are scaled with the indicated factors for clarity.

the SH as well, which is not observed. A nearly flat excitation pattern is also observed for the SH emission at 3.44 eV, i.e. above exciton transitions (figure 5.6D and 1G red line, figure 5.7D and G black line and figure 5.8B and F, black line).

Second, for excitation with two-photon energy in resonance with or above the exciton transitions, we found that the spatial excitation patterns vanish at high excitation intensity. Figure 5.9 shows the development of the

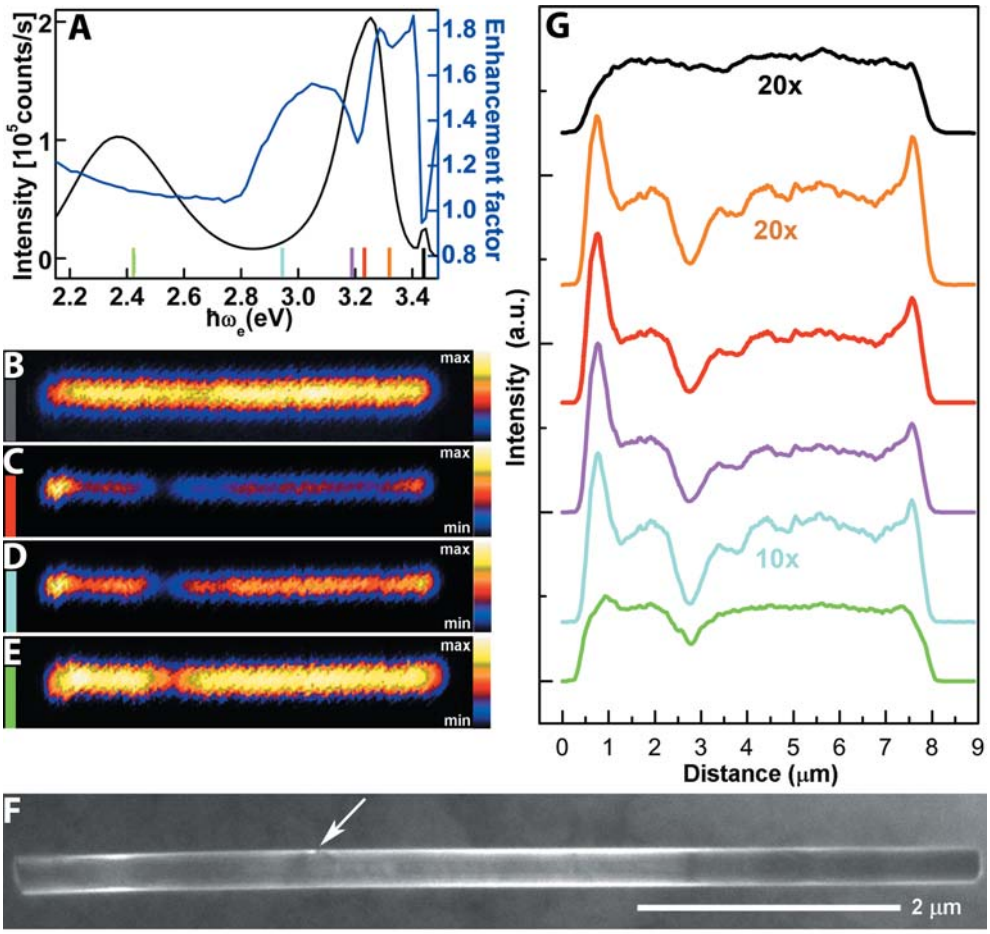

Figure 5.7 (A)(Black line) average photoluminescence spectrum of a ZnO nanowire for excitation with subbandgap light (1.72 eV). (Blue line) enhancement spectrum. (B-E) Spatially resolved excitation images taken at the emission energies indicated in panel (A) by the colored bars. (F) TEM image of the investigated wire. The wire had a length of 7.54 μm and a diameter of 269 nm. The arrow indicates a crystal defect which leads to the availability of non-radiative recombination pathways. The SH generation rate, which at this energy is a purely photonic process, remains unaffected by this electronic defect. This shows that the polaritons have strong excitonic character. (G) Excitation line traces along the length of the wire (c-axis) at emission energies indicated by the colored bars in panel A. The profiles are scaled with the indicated factors for clarity.

ratio of the excitation enhancement at the wire end with respect to the middle part for two emission energies. At low excitation power there is a

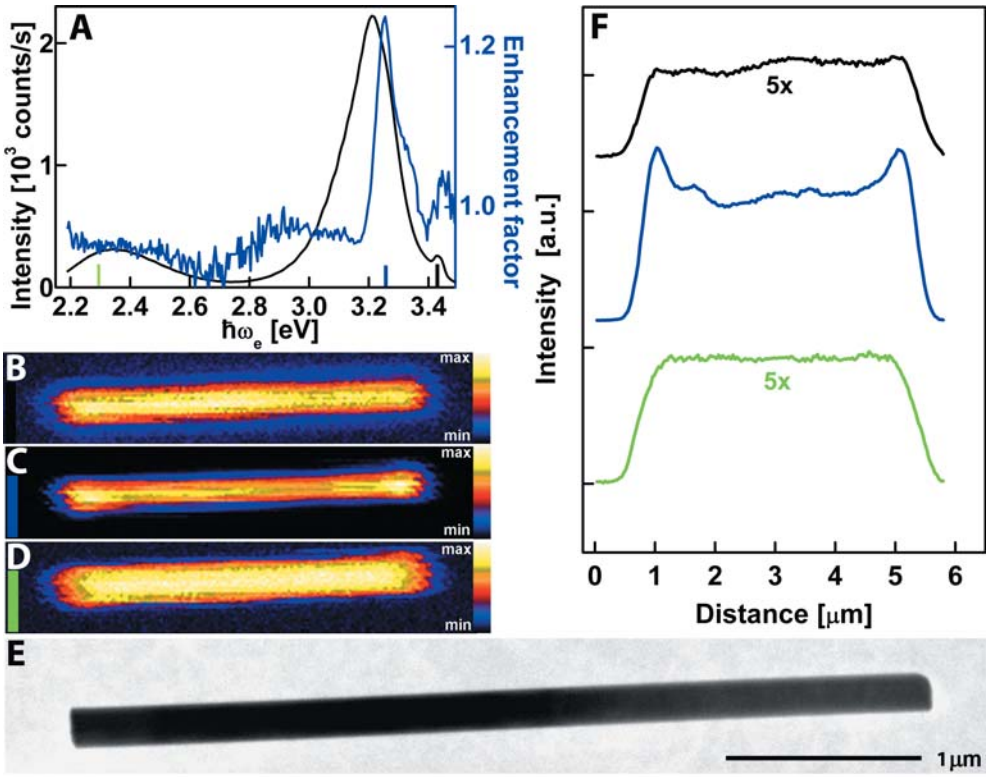

Figure 5.8 (A) (black line) Average photoluminescence spectrum of a ZnO nanowire for excitation with subbandgap light (1.72 eV).(Blue line) enhancement spectrum. (B-D) Spatially resolved excitation images taken at the emission energies indicated in panel (A) by the colored bars. (E) TEM image of the investigated wire. The wire had a length of 4.41 μm and a diameter of 195 nm. (F) Excitation line traces along the length of the wire (c-axis) at emission energies indicated by the colored bars in panel A. The profiles are scaled with the indicated factors for clarity.

large enhancement factor, indicating an excitation profile with a strong peak at the wire end. With increasing excitation power the enhancement factor converges to 1, indicating a homogeneous excitation profile. It is clear that this saturation behavior excludes a simple geometrical optical artifact as the origin of the observed excitation enhancement at the wire ends. On the contrary, it is known that exciton-polaritonic effects decrease at higher excitation intensities due to either weakening of the electron-hole attraction energy by free carrier screening, increased exciton-exciton scattering or heating [32,33]. Third, very similar features of the line traces have been measured in an independent cathodo-luminescence experiment, the results of which will be shown in the next section.

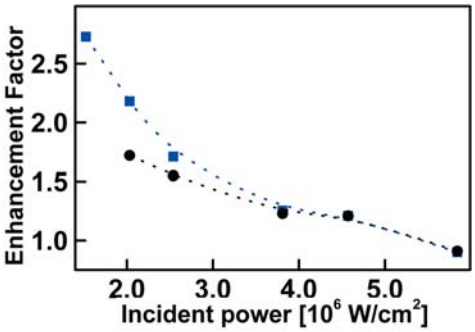

Figure 5.9 Excitation power dependency of the ratio of the excitation intensity at the wire end divided by the average excitation intensity in the middle part of the wire (enhancement factor) for the emission energies of 3.28 eV (squares) and 3.37 eV (circles).

5.3.3 Cathodo-luminescence excitation patterns

Exciton luminescence in ZnO nanowires can be generated by excitation with an electron beam. [21] Since an electron beam offers an excellent spatial resolution (<30 nm), we also measured the spatial excitation patterns of single-wire cathodo- luminescence (figure 5.10). The cathode luminescence spectrum of a single ZnO nanowire is very similar to that observed with two-photon excitation (figure 5.10A). Figure 5.10C shows that for single-wire light emission in the exciton region non-uniform excitation patterns are observed with strongly enhanced excitation rates at both wire ends. It can be seen that the enhanced excitation at the wire ends nearly vanishes for emission modes below the exciton transitions (cyan, magenta and green traces). We have investigated tens of ZnO nanowires with lengths between 0.5 and 5 μm. In about 60% of the wires similar excitation patterns as those in figure 5.10 were observed. The spatial excitation patterns observed with electron-beam excitation depend in a similar way on the emission photon energy $\hbar\omega_e$ as those observed by two-photon excitation. It is clear that these observations, with photons or electrons as excitation source, exclude experimental artifacts as the cause of the observed excitation patterns and reflect the same underlying physics.

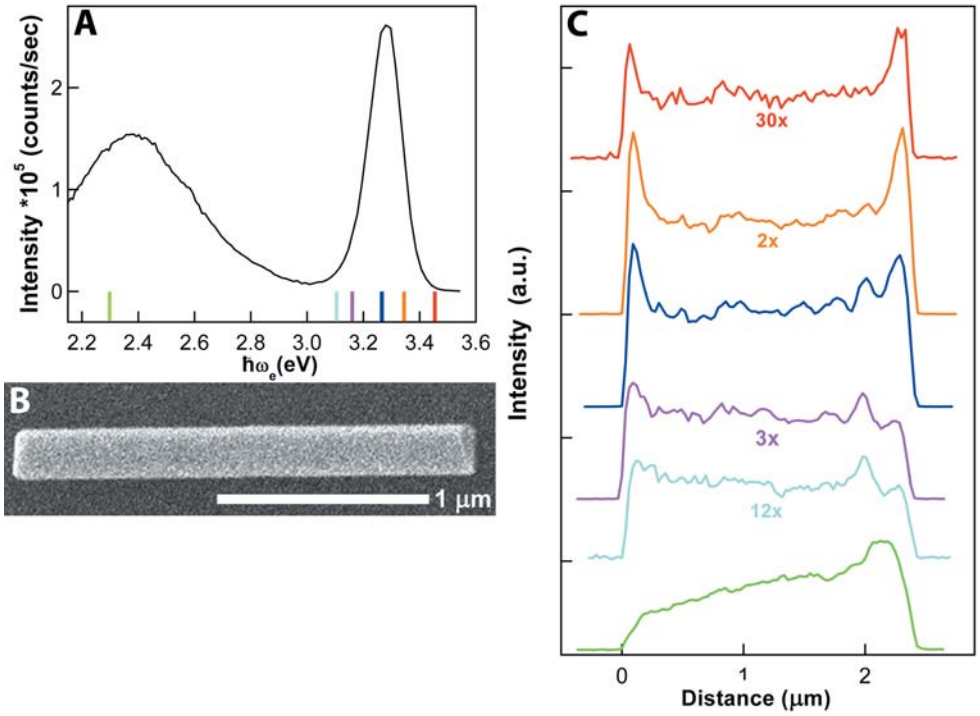

Figure 5.10 (A) Spatially averaged cathodo-luminescence (CL) spectrum of a ZnO nanowire for excitation with a 20 keV electron beam showing green and UV photoluminescence. (B) Scanning Electron Microscopy (SEM) image of the wire with a length of 2.26 μm and a diameter of 235 nm. (C) Excitation line traces along the length of the wire at emission energies indicated by the colored bars in panel A. The profiles are scaled with the indicated factors for clarity.

5.4 A model to understand excitation enhancement at the wire ends

5.4.1 Standing wave exciton-polariton modes

From the preceding sections it is clear that exciton formation is a prerequisite for the spatial patterns observed in the excitation rate along a ZnO nanowire. Since the spatial extension of excitons in ZnO is typically four orders of magnitude smaller then the observed excitation patterns [23]they must, therefore, result from strong coupling of optical cavity modes with the exciton dipoles, i.e. exciton-polariton generation. Exciton-photon coupling in macroscopic ZnO crystals was anticipated in an early paper [34]. In single-crystalline ZnO samples, exciton-polaritons were studied by absorption spectroscopy: the observation of two peaks in the optical absorption, just above and below the exciton transition is a signature of polariton formation by strong exciton-photon coupling [22]. The enhanced excitation rate that we observe at the ends of the ZnO nanowires with respect to the centre part can be understood by considering that, at a given emission energy $\hbar\omega_e$, the single-wire emission intensity is determined by all the modes detected within the bandwidth of the monochromator (10 meV). These modes at different energy interfere which leads to temporal oscillations in the intensity decaying with a time constant $2\pi/\Delta\omega$. Since all relevant timescales in the experiment (CCD response and integration time, repetition rate of the laser) are much longer than $2\pi/\Delta\omega$, the effects of interference in the measured single-wire luminescence intensity are cancelled out. Therefore, it is reasonable to assume that the detected emission is proportional to the number of modes excited at the excitation spot.

In order to calculate the excitation probability of distinct modes along the wire we consider simplified polariton eigenfunctions in the nanowire, $E_{pol} \propto \sin(m_z z/L)$, with the mode number $m_z = 1, 2, 3, \ldots$ and the wire length L (see figure 5.11A). The spatial excitation probability of such a polariton eigenfunction is proportional to its amplitude (similar as in classical mechanics: the lowest vibrational mode of a string, fixed at both ends, is most effectively excited in the middle). Since the laser excitation spot has a certain radius (200 nm) one has to consider that wave maxima and minima may be excited at the same time with the same phase which leads to cancellation. We therefore convolute the laser spot profile (figure 5.11B) with the polariton eigenfunctions. The result is a convoluted

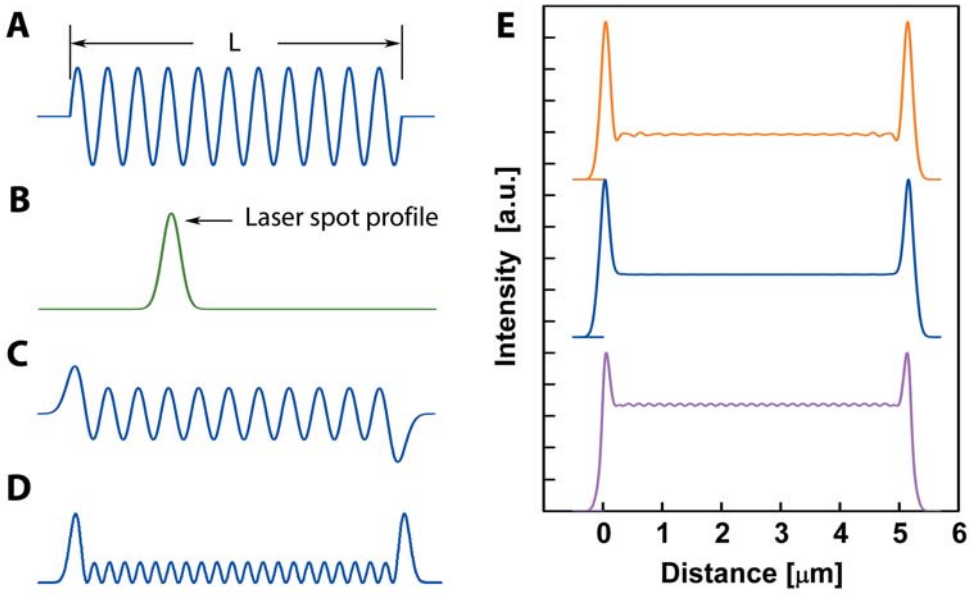

Figure 5.11 (A) Electric field distribution for a standing wave mode with mode number m_z=22. (B) Spatial profile of the laser spot. (C) Convolution of the electric field of the mode with the spatial profile of the laser spot. (D) Intensity of the convolution of the electric field of the mode with the spatial profile of the laser spot. (E) Resulting line traces after summation over a number of profiles shown in panel D and the addition of an incoherent background, showing different excitation enhancement at the wire ends for the detection energy intervals of 3.39 eV+/- 5 meV (upper line), 3.29 eV+/- 5 meV(middle line) and 3.21 eV+/- 5 meV (lower line) (also see figures 5.6G, 5.7G and 5.8F).

eigenfunction as shown in figure 5.11C, which has an increased amplitude close to the wire ends. The intensity of this convoluted eigenfunction is shown in figure 5.11D. This intensity pattern for one mode looks already remarkably similar to the observed patterns but in principle several modes could be detected at the same time. Therefore a summation needs to be made over all the modes present in the detection energy interval. The (photon or exciton-polariton) dispersion relation tells us how many modes and which modes have to be taken into account in the excitation profile. As a last step, a constant background per energy interval is added to the result of the summation to account for any luminescence which is not related to the longitudinal modes (for instance with the wavevector perpendicular to the wire's long axis.)

With prior knowledge of the dispersion relation (see figure 5.13) one can make the summation for different detection energy intervals.

Figure 5.11E shows the resulting profiles for three detection energy intervals: 3.39 eV+/- 5 meV (upper line), 3.29 eV+/- 5 meV (middle line) and 3.21 eV+/- 5 meV (lower line). For now, it is sufficient to appreciate that for different detection energy regions, the result of the summation yields a different ratio of the excitation rate at the wire ends with respect to the average intensity in the middle part of the wire.

5.4.2 Enhancement spectrum and dispersion relation

To further investigate the dispersion properties of the polariton modes in a given nanowire, we studied the spatial excitation patterns as a function of the mode energy $\hbar\omega_e$ of the emitted light. We quantified the enhancement of the mode generation rate at each wire end by the enhancement factor EF($\hbar\omega_e$), defined as the single-wire emission intensity at $\hbar\omega_e$ for excitation at a wire-end divided by the single-wire emission for excitation at the centre (spatially averaged over a few μm). Spectra of EF($\hbar\omega_e$) measured on four different wires are presented in figures 5.6A ,5.7A, 5.8A and 5.12 (blue lines) together with the emission spectra of the wires, averaged for excitation over the entire wire (black lines). The enhancement spectra of these four and other wires are very similar. For the discussion we focus on the spectrum shown in Figure 5.6A which, for convenience, is repeated in figure 5.13A. Below a certain cut-off energy (at 2.71 eV), EF($\hbar\omega_e$) is unity. There is a broad enhancement peak in the transparent region between the cut-off energy and 3.2 eV, with reproducible modulations due to Fabry-Pérot interference in the ZnO nanowire cavity. Several authors have attributed the decrease in free spectral range between the interference peaks to strong exciton-photon interaction resulting in a decreased slope of

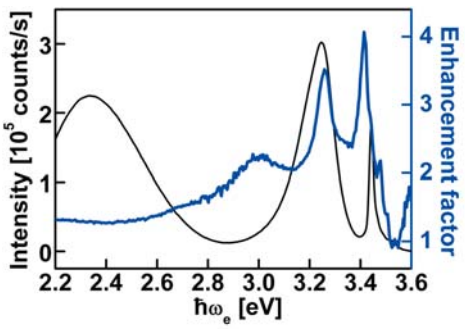

Figure 5.12 Average spectrum (black line) and enhancement spectrum (blue line) of a wire excited with 1.72 eV light. The enhancement spectrum shows a peak splitting of 160 meV near the exciton resonances. The wire had a length of 6.47 μm and a diameter of 319 nm.

the dispersion [35-37,38] From the width of the interference peaks we determine a Q-factor of the cavity of 256, in agreement with calculations [39]. This value only holds for the optical part between 2.7 and 3.0 eV. The most prominent features of the enhancement spectrum EF($\hbar\omega_e$) are the two peaks in the exciton energy region between 3.2 and 3.5 eV. The low-energy peak at around 3.28 eV coincides with the high-energy side of the exciton luminescence peak. The second peak in the enhancement spectrum is centered at 3.38 eV; note that the exciton luminescence intensity is very low at this energy.

We calculated the enhancement spectrum EF($\hbar\omega_e$) from the exciton-polariton dispersion curve for a ZnO nanowire with the same length as in Figures 5.6 and 5.13, we took into account lateral photon confinement and the dispersion relation given by (also see chapter 2) [15, 11]:

$$\varepsilon(\omega,k)=\varepsilon_\infty\left(1+\sum_{j=A,B,C}\Omega_j\frac{\omega_{j,L}^2-\omega_{j,T}^2}{\omega_{j,T}^2-\omega^2-i\omega\gamma_j}\right)=\frac{c^2k^2}{\omega^2} \qquad (1)$$

with the background dielectric constant ε_∞, the transverse ($\omega_{j,T}$) and longitudinal ($\omega_{j,L}$) resonance frequencies, the damping constants γ_j, the speed of light c and a pre-factor Ω_j as defined in ref. [15]. The damping and the resonant frequencies (for A, B and C excitons) were taken as for a macroscopic ZnO crystal [12] with the resonance frequencies shifted to room-temperature. This calculated dispersion relation (without strongly damped modes) is shown in figure 5.13B. From this dispersion relation we have calculated the excitation profiles between 2.5 and 3.5 eV and the ensuing enhancement spectrum (figure5.13C). We collect the modes present in each energy window $\hbar\omega_e \pm 5$ meV according to the polariton dispersion curve, convoluted the field of each standing wave polariton mode with the laser profile, calculated the intensity, made the summation and added a background to account for all excitations which are not proper polaritons. We made the reasonable assumption that this background is independent of the position along the wire and the emission energy. From these excitation profiles along the wire, we obtained EF($\hbar\omega_e$); the resulting spectrum is shown in Figure 5.13C.

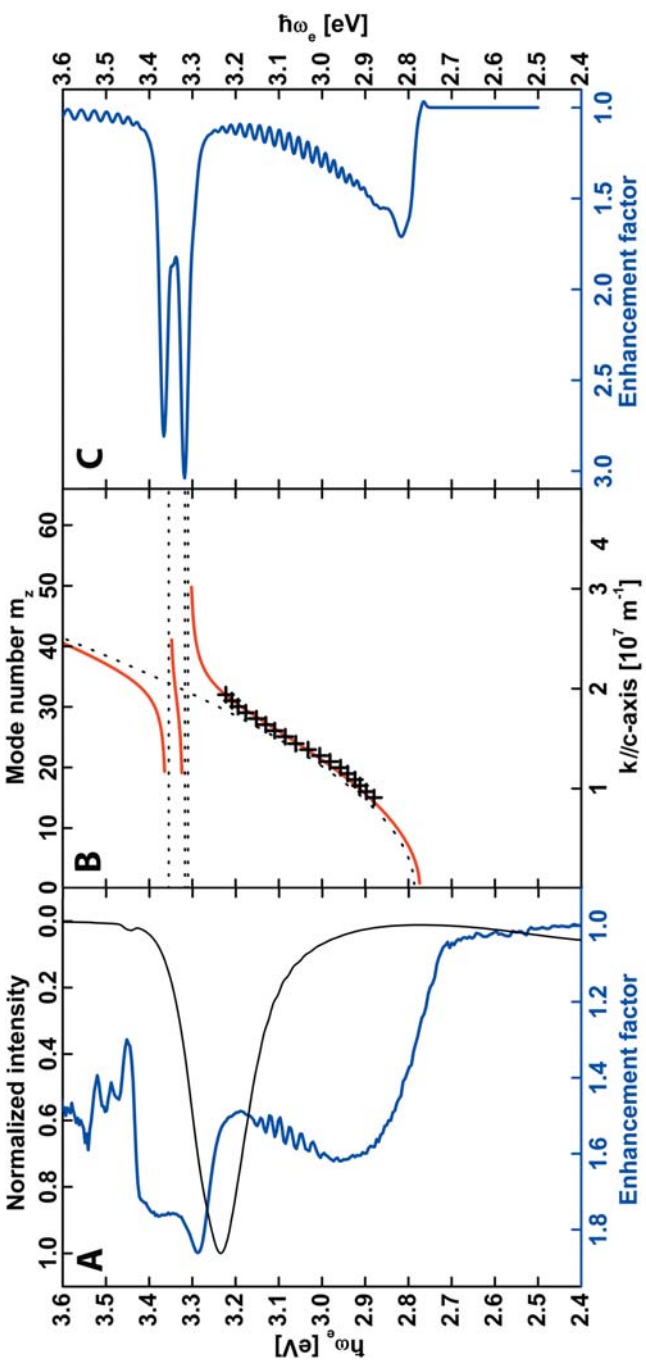

Figure 5.13 (A) Average spectrum (black line) and enhancement spectrum (blue line) of a wire excited with light of energy 1.72 eV. The enhancement spectrum shows a peak splitting of 102 meV near the exciton resonances and modulations due to Fabry-Pérot interference in the transparent region (2.7-3.2 eV). (B) Exciton-polariton dispersion (red lines) calculated with equation (1) from the resonances of the A-(3.309 eV), B-(3.315 eV) and C-(3.355 eV) excitons (dotted horizontal lines) and a photon mode confined in the nanowire cavity (dotted curve). For clarity, the strongly damped modes in the anti-crossing energy- gap are not shown. The crosses indicate the energetic peak positions obtained from the Fabry-Pérot maxima of the enhancement spectrum shown in panel B. These maxima are equidistantly spaced at $m_z^*(\pi/L)$ in k-space (L= the length of the wire=5.19 µm) and give the slope of the exciton-polariton dispersion between 2.7 and 3.2 eV. (C) Calculated enhancement resulting from the dispersion curve shown in panel C.

5.5 Discussion

The essential features of the experimental enhancement spectrum i.e. the broad enhancement peak with Fabry-Pérot oscillations in the blue region, the cut-off energy and, importantly, the two peaks in the exciton region, are well reproduced by the calculation. The enhancement in the energy range between the cut-off energy and 3.2 eV is due to standing wave polariton modes with a strong photon character. The oscillations reflect the detection of single modes in the energy interval $\hbar\omega_c \pm 5$ meV. The observation of these oscillations proves that there are discrete modes confined in the length direction of the wire. The observation of a cut-off energy shows that the modes are also discretized by confinement in the lateral dimensions. The two peaks in the exciton region are due to a high energy density of the confined polariton modes i.e. flat parts of the dispersion. In the calculated enhancement spectrum based on the literature values of the three resonances in ZnO, shown in figure 5.13C, the peak separation amounts to 50 meV which is still comparable to the energy separation between the exciton levels. However in the model the peak separation increases with increasing oscillator strength (represented by the longitudinal-transverse splitting, see chapter 2). Figure 5.14 shows the effect of increased oscillator strength on the enhancement spectrum in the case of three resonances. Alternatively one could argue that because of the low binding energy of the C-exciton (12 meV) and the low oscillator strength of the A-exciton ($\hbar(\omega_L - \omega_T)$= 2 meV), at room-temperature only the B-exciton should be taken into

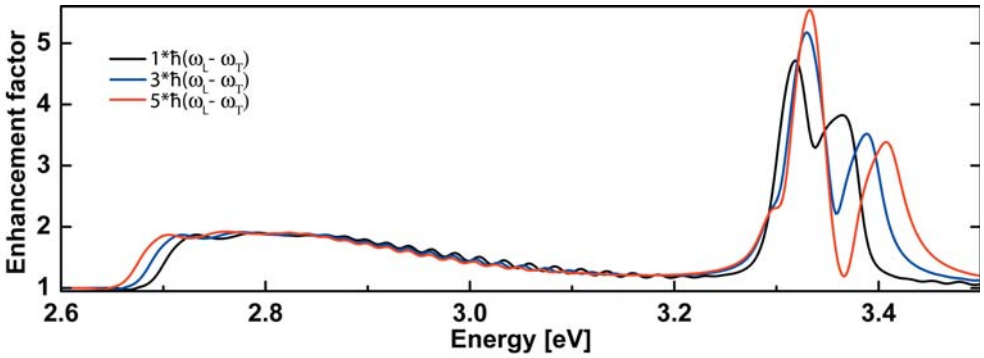

Figure 5.14. Influence of increasing oscillator strength on the enhancement spectra in the case of three resonances. For these plots the literature values of the longitudonal-transverse splitting of 2 meV, 12 meV and 12 meV for the ZnO A-, B- and C-excitons respectively were scaled with a factor of 1 (black line), 3 (blue line) and 5 (red line). Additionally, a wider energy detection interval was used (15 meV) instead of the 10 meV used in figure 5.13C.

account. The effect of increased oscillator strength on the enhancement spectrum in such a single resonance model is shown in figure 5.15. For $\hbar(\omega_L-\omega_T)$= 2 meV, no peak splitting is observed. The literature value of $\hbar(\omega_L-\omega_T)$= 12 meV results in a peak splitting of 81 meV while the largest experimentally observed peak splitting of 160 meV (fig. 5.12) corresponds to a value of $\hbar(\omega_L-\omega_T)$= 28 meV, or approximately twice the literature value. The intensity ratio of the two peaks looks different than in the experiment but one should consider that in the model the polariton mode lifetime and occupation are not taken into account. This could change the intensity ratio of the peaks considerably.

We propose that the measured gap between both groups of polariton modes (between 60 and 164 meV) is hence the result of increased exciton-photon coupling in the wires. The energy difference between the two groups of polariton modes forms a lower limit for the Rabi-splitting, a measure of the strength of the exciton-photon coupling. In Figure 5.13A we observe a splitting of about 100 meV. Several other wires have shown an even larger splitting up to 164 meV (see figure 5.12). We note that the energy separation between the two groups of polariton modes is considerably larger than the energy difference between the A, B and C excitons in bulk ZnO of about 50 meV [19]. Our results indicate increased strong light-matter interaction confined in ZnO nanowire cavities. The fact that for different wires we observe different Rabi-splittings points to an influence of the wire morphology (thickness, length, end facet quality) on

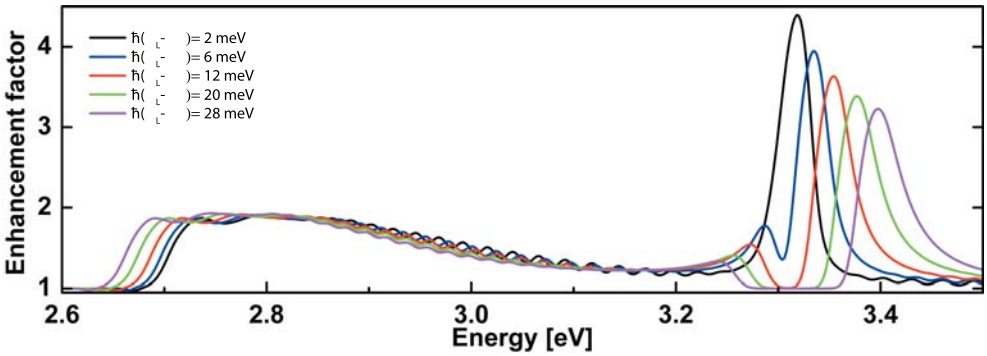

Figure 5.15. Influence of increasing oscillator strength (longitudonal-transverse splitting) on the enhancement spectra in the case of a single resonance. The literature value of a longitudonal-transverse splitting of 12 meV for the ZnO B-exciton results in a peak splitting of 81 meV. A longitudonal-transverse splitting of 28 meV results in a peak splitting of 160 meV. Additionally, a wider energy detection interval was used (15 meV) instead of the 10 meV used in figure 5.13C.

the observed large Rabi-splittings.

The magnitude of the Rabi-splitting depends generally on the ratio of the oscillator strength to the mode volume [23, 24, 31]. A smaller structure with higher reflectivity on its boundaries leads to a smaller mode volume which leads to a larger Rabi-splitting due to the increased electric field strength inside the structure. A way to increase the oscillator strength of an exciton in a semiconductor is to electronically confine the exciton i.e. a quantum dot or quantum well [40]. Not surprisingly, the first observation of a Rabi-splitting in a semiconductor was achieved in a microcavity fitted with high reflectivity Distributed Bragg Mirrors (DBR) and a GaAs quantum well [7]. The oscillator strength and hence the Rabi-Splitting could be further increased by placing multiple quantum dots at antinodes, coupling to the same mode of the cavity. The largest Rabi-Splitting that could be achieved with quantum dots and microcavities was 10 meV.

A recent development entails the use of a microcavity which totally exists of semiconductor material fitted with DBR's [41]. These bulk microcavities do not use exciton confinement to enhance the oscillator strength but rather allow for multiple excitons to behave as one "giant " exciton with a very large oscillator strength [23]. Additionally, because the microcavity is formed by the active material a much better overlap between the exciton and photon wavefunctions is obtained resulting in an increased Rabi-splitting. For instance, it was reported that bulk GaN microcavities show two resonance peaks in the reflection spectra, with a Rabi-splitting of about 50 meV [42]. We remark that an even larger Rabi-splitting has been observed in an organic system which can be mainly attributed to a large oscillator strength of the electronic transition [43].

We believe that the combination of photon confinement in a small cavity and the use of a cavity where the electronic transitions occur over the entire length between the mirrors results in our observed large Rabi-splittings. A Rabi-splitting of 120 meV was predicted for a ZnO λ cavity with distributed Bragg mirrors [24]. Our results provide the first strong evidence that such a large splitting can be reached, even in a simple nanowire geometry.

It is known that exciton-polaritons exist in bulk ZnO and it is therefore hardly surprising to find that exciton-polaritons exist in ZnO nanowires. However, it is the extremely large exciton-photon coupling and its macroscopic manifestation that are surprising. If the exciton(-polariton) is delocalized over the entire wire by virtue of its photonic component one could expect efficient energy transfer from one end of the wire to the other

if excitation occurs at one end. Another intriguing question pertains to the confinement of energy inside a nanowire. A photon can leak out of a dielectric structure for a considerable distance, at least for the distance between optical components in future nanoscale photonic devices (<100nm). An electron on the other hand is tightly confined to the nanowire (<1nm) and does to a much lesser extent suffer from crosstalk between neighboring components. Interesting new options for the further miniaturization of photonic devices could be reached if an energy-wavevector regime can be found where simultaneously the long distance properties of photons (delocalization) and the tight confinement of electrons can be exploited.

Finally it is informative to place our findings in the the field of sub-wavelength optics. Presently Surface Plasmon-Polaritons (SPP), where light is coupled to collective electron waves in sub 100nm metal stripes, are extensively investigated to circumvent the diffraction limit of light.[44] The integration with electronics has however not yet been made. Semiconductor nanowires on the other hand have proven to offer electron to photon conversion and can be much more easily integrated into opto-electronic devices. It is this flexibility combined with the prospect of subwavelength optics that make semiconducting nanowires so promising for future nanophotonic circuitry.

5.6 Conclusions

Since both the electron-hole binding energy (60 meV) and the Rabi splitting are considerable larger than kT, exciton-photon coupling plays an important role in the optical properties of ZnO nanowires at room temperature. The strongly modified light dispersion curve (Figure 5.13B) should be taken into account if ZnO nanowires are applied in photonic circuits. Impressive sub-wavelength guiding has been reported in ZnO nanowires [45]; we observed similar guiding in our experiments (see chapter 1). We propose that this guiding is mediated by the transverse exciton-polaritons (lower branch at around 3.28 eV). The observed delocalization of polaritons with high wave numbers over the entire wire length is paramount to waveguiding with small losses. The possibility of generating polariton modes at room temperature, which strongly vary in their wave properties for small changes in energy, could be of huge importance for nanophotonic circuitry.

References

1 Y. Xia, P. Yang, Y. Sun, Y. Wu, B. Mayers, B. Gates, Y. Yin, F. Kim, and H. Yan, One-Dimensional Nanostructures: Synthesis, Characterization, and Applications, *Adv.Mater.* **15** (2003), p. 353-389.

2 B. A. Wacaser, K. Deppert, L. S. Karlsson, L. Samuelson, and W. Seifert, Growth and characterization of defect free GaAs nanowires, *J.Cryst.Growth* **287** (2006), p. 504-508.

3 X. Duan, Y. Huang, Y. Cui, J. Wang, and C. M. Lieber, Indium phosphide nanowires as building blocks for nanoscaleelectronic and optoelectronic devices, *Nature* **409** (2001), p. 66-69.

4 M. S. Gudiksen, L. J. Lauhon, J. Wang, D. C. Smith, and C. M. Lieber, Growth of nanowire superlattice structures for nanoscale photonics and electronics, *Nature* **415** (2002), p. 617-620.

5 M. H. Huang, S. Mao, H. Feick, H. Yan, Y. Wu, H. Kind, E. Weber, R. Russo, and P. Yang, Room-Temperature Ultraviolet Nanowire Nanolasers, *Science* **292** (2001), p. 1897-1899.

6 J. Wang, M. S. Gudiksen, X. Duan, Y. Cui, and C. M. Lieber, Highly Polarized Photoluminescence and Photodetection from Single Indium Phosphide Nanowires, *Science* **293** (2001), p. 1455-1457.

7 C. Weisbuch, M. Nishioka, A. Ishikawa, and Y. Arakawa, Observation of the coupled exciton-photon mode splitting in a semiconductor quantum microcavity, *Phys.Rev.Lett.* **69** (1992), p. 3314-3317.

8 J. P. Reithmaier, G. Sek, A. Löffler, C. Hofmann, S. Kuhn, S. Reitzenstein, L. V. Keldysh, V. D. Kulakovskii, T. L. Reinecke, and A. Forchel, Strong coupling in a single quantum dot–semiconductor microcavity system, *Nature* **432** (2004), p. 197-200.

9 T. Yoshie, A. Scherer, J. Hendrickson, G. Khitrova, H. M. Gibbs, G. Rupper, C. Ell, O. B. Shchekin, and D. G. Deppe, Vacuum Rabi splitting with a single quantum dot in a photonic crystal nanocavity, *Nature* **432** (2004), p. 200-203.

10 D. C. Reynolds, D. C. Look, B. Jogai, C. W. Litton, G. Cantwell, and W. C. Harsch, Valence-band ordering in ZnO, *Phys.Rev.B* **60** (1999), p. 2340-2344.

11 C. F. Klingshirn, *Semiconductor Optics* (Springer-Verlag, Berlin-Heidelberg-New York, 1997).

12 S. F. Chichibu, T. Sota, G. Cantwell, D. B. Eason, and C. W. Litton, Polarized photoreflectance spectra of excitonic polaritons in a ZnO single crystal, *J.Appl.Phys.* **93** (2003), p. 756-758.

13 E. McGlynn, J. Fryar, M. O. Henry, J.-P. Mosnier, J. G. Lunney, D. O. Mahony, and E. dePosada, Exciton–polariton behaviour in bulk and polycrystalline ZnO, *Physica B* **340-342** (2003), p. 230-234.

14 A. A. Toropov, O. V. Nekrutkina, T. V. Shubina, T. Gruber, C. Kirchner, A. Waag, K. F. Karlsson, P. O. Holtz, and B. Monemar, Temperature-dependent exciton polariton photoluminescence in ZnO films, *Phys.Rev.B* **69** (2004), p. 165205/1-165205/4.

15 J. Lagois, Depth dependent eigen energies and damping of excitonic polaritons near a semiconductor surface, *Phys.Rev.B* **23** (1981), p. 5511-5520.

16 B. Gil, Oscillator strengths of A, B, and C excitons in ZnO films, *Phys.Rev.B* **64** (2001), p. 201310/1-201310/3.

17 A. V. Rodina, M. Strassburg, M. Dworzak, U. Haboek, A. Hoffman, A. Zeuner, H. R. Alves, D. M. Hofmann, and B. K. Meyer, Magneto-optical properties of bound excitons in ZnO, *Phys.Rev.B* **69** (2004), p. 125206/1-125206/9.

18 W. R. L. Lambrecht, A. V. Rodina, S. Limpijumnong, B. Segall, and B. K. Meyer, Valence-band ordering and magneto-optic exciton fine structure in ZnO, *Phys.Rev.B* **65** (2002), p. 075207/1-075207/12.

19 D. G. Thomas, The exciton spectrum of Zinc Oxide, *J.Phys.Chem.Sol.* **15** (1960), p. 86-96.

20 J. J. Hopfield, ?, *J.Phys.Chem.Sol.* **15** (1960), p. 97.

21 A. v. Dijken, E. A. Meulenkamp, D. Vanmaekelbergh, and A. Meijerink, Identification of the transition responsible for the visible emission in ZnO using quantum size effects, *J.Lumin.* **90** (2000), p. 123-128.

22 J. J. Hopfield and D. G. Thomas, Polariton Absorption Lines, *Phys.Rev.Lett.* **15** (1965), p. 22-25.

23 B. Gil and A. V. Kavokin, Giant exciton-light coupling in ZnO quantum dots, *Appl.Phys.Lett.* **81** (2002), p. 748-750.

24 M. Zamfirescu, A. Kavokin, B. Gil, G. Malpuech, and M. Kaliteevski, ZnO as a material mostly adapted for the realization of room-temperature polariton lasers, *Phys.Rev.B* **65** (2002), p. 161205/1-161205/4.

[25] M. H. Huang, Y. Wu, H. Feick, N. Tran, E. Weber, and P. Yang, Catalytic Growth of Zinc Oxide Nanowires by Vapor Transport, *Adv.Mater.* **13** (2001), p. 113-116.

[26] R. Prasanth, L. K. v. Vugt, D. Vanmaekelbergh, and H. C. Gerritsen, Resonance enhancement of optical second harmonic generation in a ZnO nanowire, *Appl.Phys.Lett.* **88** (2006), p. 181501/1-181501/4.

[27] B. F. Levine, A New Contribution to the Nonlinear Optical Susceptibilityi Arising from Unequal Atomic Radii, *Phys.Rev.Lett.* **25** (1970), p. 440-443.

[28] A. Teke, Ü. Özgür, S. Dogan, X. Gu, H. Morkoç, B. Nemeth, J. Nause, and H. O. Everitt, Excitonic fine structure and recombination dynamics in single-crystalline ZnO, *Phys.Rev.B* **70** (2004), p. 195207/1-195207/10.

[29] X. Q. Zhang, Z. K. Tang, M. Kawasaki, A. Ohtomo, and H. Koinuma, Resonant exciton second-harmonic generation in self-assembled ZnO microcrystallite thin films, *J.Phys: Condens.Matter* **15** (2003), p. 5191-5196.

[30] T. Tritschler, O. D. Mücke, M. Wegener, U. Morgner, and F. X. Kärtner, Evidence for third-harmonic generation in disguise of second-harmonic generation in extreme nonlinear optics, *Phys.Rev.Lett.* **90** (2003), p. 217404.

[31] M. Bayer, A. Forchel, T. L. Reinecke, P. A. Knipp, and S. Rudin, Confinement of Light in Microresonators for Controlling Light–Matter Interaction, *Phys.Status Sol.A* **191** (2002), p. 3-32.

[32] R. Houdré, J. L. Gibernon, P. Pellandini, R. P. Stanley, U. Oesterle, C. Weisbuch, J. O'Gorman, B. Roycroft, and M. Ilegems, Saturation of the strong-coupling regime in a semiconductor microcavity: Free-carrier bleaching of cavity polaritons, *Phys.Rev.B* **52** (1995), p. 7810-7813.

[33] A. I. Tartakovskii, V. D. Kulakovski, Y. I. Koval, T. B. Borzenko, A. Forchel, and J. P. Reithmaier Exciton-photon interaction in low-dimensional semiconductor microcavities, *J.Exp.Th. Phys.* **87** (1998), p. 723-730.

[34] J. J. Hopfield, Theory of the contribution of Excitons to the Complex Dielectric Constant of Crystals, *Phys.Rev.* **112** (1958), p. 1555-1567.

[35] C. Boemare, Observation of Fabry-Pérot modes in the upper branch of the polariton in ZnSe-GaAs epilayers, *Phys.Rev.B* **51** (1995), p. 7954-7957.

[36] V. A. Kiselev, B. S. Razbirin, and I. N. Uraltsev, Additional Waves and Fabry-Perot Interference of Photoexcitons (Polaritons) in Thin II-VI Crystals, *Phys.Status Solidi B* **72** (1975), p. 161-172.

[37] I. V. Makarenko, I. N. Uraltsev, and V. A. Kiselev, Additional waves and Polariton Dispersion in CdS Crystals, *Phys.Status Solidi B* **98** (1980), p. 773-779.

[38] T. Mita and N. Nagasawa, Anomalous Wave Interference At Z3-Exciton Resonance of CuCl, *Sol. Stat.Comm.* **44** (1982), p. 1003-1006.

[39] A. V. Maslov and C. Z. Ning, Reflection of guided modes in a semiconductor nanowire laser, *Appl. Phys.Lett.* **83** (2003), p. 1237-1239.

[40] C. Weisbuch, H. Benisty, and R. Houdre, Overview of fundamentals and applications of electrons, excitons and photons in confined structures, *J.Lumin.* **85** (2000), p. 271-293.

[41] Y. Chen, A. Tredicucci, and F. Bassani, Bulk exciton polaritons in GaAs microcavities, *Phys.Rev.B* **52** (1995), p. 1800-1805.

[42] I. R. Sellers, F. Semond, M. Leroux, J. Massies, P. Disseix, A.-L. Henneghien, J. Leymarie, and A. Vasson, Strong coupling of light with A and B excitons in GaN microcavities grown on silicon, *Phys. Rev.B* **73** (2006), p. 033304/1-033304/4.

[43] D. G. Lidzey, D. D. C. Bradley, M. S. Skolnick, T. Virgili, S. Walker, and D. M. Whittaker, Strong exciton-photon coupling in an organic semiconductor microcavity, *Nature* **395** (1998), p. 53-55.

[44] W. L. Barnes, A. Dereux, and T. W. Ebbesen, Surface plasmon subwavelength optics, *Nature* **424** (1996), p. 824-830.

[45] M. Law, D. J. Sirbuly, J. C. Johnson, J. Goldberger, R. J. Saykally, and P. Yang, Nanoribbon Waveguides for Subwavelength Photonics Integration, *Science* **305** (2004), p. 1269-1273.

Chapter 6

Phase-correlated non-directional laser emission from ZnO nanowires

In this chapter the laser emission from individual ZnO nanowires is investigated. The energy spacing between sharp lasing modes scales with the reciprocal length of the nanowire; thus, laser emission peaks correspond to longitudinal Fabry-Pérot modes of the nanowire cavity. An interference pattern due to coherent laser emission from the wire end facets is observed. Comparison with numerical simulations shows that the laser light is emitted nearly spherically from the wire ends, with a zero or fixed phase difference.

61 Introduction

Semiconductor nanowires show extraordinary optical properties such as wave guiding [1-3] and lasing [4-10] and, thus, form a class of very promising building blocks for novel miniaturized optical and opto-electronic devices.[11, 12] Nanowires are currently among the smallest known lasing devices with lengths between 1 – 50 μm and diameters which can be significantly smaller than the emission wavelength in vacuum. In contrast to microcavities with distributed Bragg reflectors,[13] nanowires form an optical cavity due to the refractive index difference with its surrounding.[4, 10, 14-16] At high excitation intensities sharp laser peaks appear in the luminescence spectrum and a highly nonlinear input-output characteristic has been observed from GaN,[4] ZnO,[5] CdS,[6] ZnS[7] and GaSb[8] nanowires. Such nanolasers are usually pumped optically but also electrically driven lasers have been demonstrated.[9] The development of coherent light sources on the nanoscale opens the door towards miniaturized spectroscopic systems and photonic circuits. On the other hand extended research is required to investigate novel effects due to the small diameter of the nanolaser cavity,[17] which is often beyond the diffraction limit of the emitted light. In this chapter the optical properties of highly excited ZnO nanowires are studied. We observe laser emission from the nanowire end facets with diameters ranging from 200 – 400 nm, but also lasing of thinner wires is known from the literature.[10] While in macroscopic laser systems the emission is highly directional, it is not obvious how the light is emitted from facets with sub-wavelength dimensions. Theoretical investigations of the far field predicts that the angular emission intensity should depend strongly on the mode type (TE, transverse electric, TM, transverse magnetic, or HE, hybrid modes) and could be spread over a large emission angle.[18]

In this chapter evidence is presented for highly non-directional emission from lasing ZnO nanowires. First, in section 6.3.1, the general features of lasing ZnO nanowires are presented. It is shown that the laser emission peaks correlate well with Fabry-Pérot (FP) modes of the nanowire cavity. Then in section 6.3.2 clear interference patterns of two emission sources located at the two nanowire ends are presented. A detailed analysis in section 6.3.3 reveals that the interference pattern depends not only on the emission wavelength and the wire length but also on the optical components of the measurement instrument (microscope).[19] This enabled us to simulate interference patterns for different angular emission

distributions from the wire ends. Comparison with experimentally measured patterns shows that a good agreement with the simulations can only be achieved if the two sources have a fixed phase relation and light waves emitted from the end facets have strong components in side- and backwards direction, i.e. the ends act nearly as point sources.

62 Experimental

ZnO nanowires with diameters ranging from 60 nm to 400nm and lengths of up to 20 μm were grown vertically on oriented sapphire substrates using the carbothermal reduction method.[20] Details of the synthesis can be found in Chapter 3. After growth, the wires were mechanically broken off and dispersed onto SiO_2 covered (500nm) Si substrates, on which gold markers had been defined by electron beam lithography. This enabled us to locate individual wires and to perform optical measurements and scanning electron microscopy (SEM) on the same nanowires. Optical experiments were performed using a pulsed Nd:YLF laser (10ns pulse length) at 349nm with a tunable repetition rate of 2 – 5 kHz, which was weakly focused onto the nanowires using an optical microscope (Zeiss Axioplan 2) with an infinity-corrected objective (100x magnification, NA 0.9). The experimental configuration is shown in figure 6.1. The spot diameter of the laser excitation, approximately 20 μm, was such that the entire volume of the wires was excited. The excitation power was adjusted using different combinations of neutral density filters. The emission was collected by the same objective and the excitation wavelength was filtered by a dichroic mirror and a long pass filter. The emission was either projected onto a CCD camera for imaging or coupled by a multimode fiber into an Acton Research 300spi 0.3 m spectrometer, fitted with a liquid nitrogen cooled Princeton research charge coupled device (CCD) for spectral analysis. The detection system had an energy resolution of ~1.3 meV.

Figure 6.1 Experimental setup.

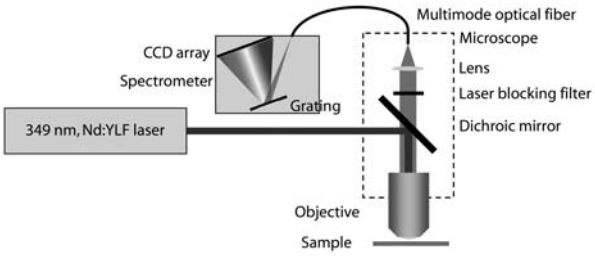

63 Results

631 General ZnO nanowire lasing properties

Highly photo-excited (>10 W/cm²) ZnO nanowires show almost exclusively UV emission while at low excitation intensities a significant amount of the emitted light is in the green spectral range. The UV emission spectra of an individual ZnO nanowire for four different (high) excitation intensities are shown in Figure 6.2 ($\hbar\omega_{excitation}$=3.55 eV). At an excitation intensity of 24 W/cm² (fig. 6.2A) the UV luminescence is broad and at the low energy side of the peak, modulations due to Fabry-Pérot interference along the length of the wire can be seen. The mode spacing of these modulations decreases going from lower energy to 3.28 eV; a manifestation of an increasing refractive index when approaching the exciton resonances from lower energy (also see chapter 5 and figure 5.13C). At the lasing threshold, 93 W/cm² for this wire (fig. 6.2B), the modulations around an emission energy of 3.2 eV deepen and shift to higher energy while the

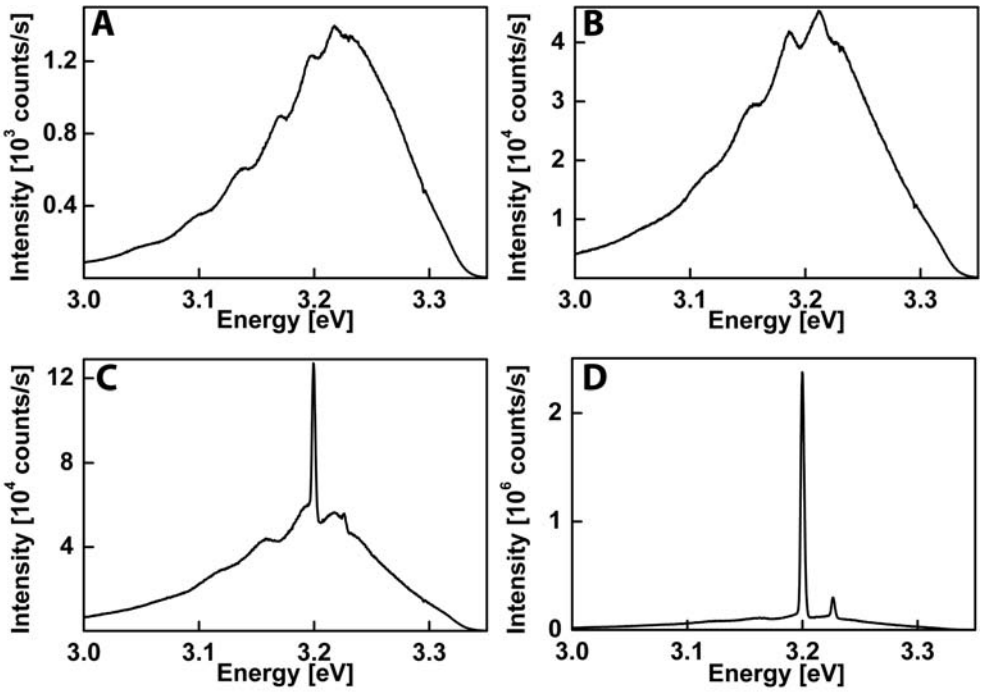

Figure 6.2 Emission spectra of an individual ZnO nanowire excited with an excitation intensity of (A) 24 W/cm², (B) 93 W/cm², (C) 139 W/cm² and (D) 203 W/cm².

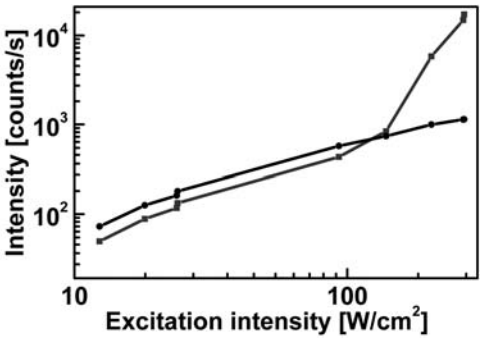

Figure 6.3 Excitation power dependent emission intensity of an individual nanowire for the energy regions of 3.20 eV +/- 5 meV (squares) and 3.21 eV +/- 5 meV (circles).

modulations at lower energy smoothen. The deepening of the modulations is due to a favorable gain for these modes. The smoothing of the modulation at lower energy could be the same effect as is seen in chapter 5; increased scattering renders exciton-polaritons effects less pronounced. Above lasing threshold at an excitation intensity of 139 W/cm^2 (fig 6.2C) the laser emission is clearly distinguished as two pronounced peaks with a full width half maximum of 2.5 meV which is not detection system limited. At an excitation intensity of 203 W/cm^2 (fig. 6.2D) the emission spectrum is dominated by the two emission modes.

Laser emission is further characterized by a non-monotonous input-output characteristic. Figure 6.3 shows the integrated emission intensity for two emission energy ranges (3.20eV± 5 meV, squares and 3.21 eV± 5 meV, circles). The intensity of the lasing emission at 3.20 eV shows a monotonous increase up to an excitation power of 93 W/cm^2. At higher excitation intensities the emission intensity strongly increases with excitation power. The emission intensity of the neighboring energy region around 3.21 eV does not show this increase.

Depending on synthesis batch and sample preparation (method of breaking the nanowires of the substrate) we observe that 10% – 50% of the wires show lasing. The lasing spectra of many nanowire lasers of different diameter and length have been investigated. Generally longer nanowires show multiple lasing peaks while shorter wires (<1.5 μm) only show single peaks, suggesting that the observed modes are longitudinal in nature. A plot of the lasing mode spacing (square data points) versus reciprocal nanowire length (figure 6.4A) yields a linear dependence, showing that the observed lasing peaks are due to longitudinal Fabry-Pérot modes. The spread in mode-spacings of the wires having multiple lasing peaks is mainly caused by the varying refractive index at the energies of these

modes; a higher refractive index causes a decrease of the mode spacing. Also shown in figure 6.4A is data for two wires which did not conform to the linear dependence (round data points) on reciprocal wire length. The emission spectra of these wires with lengths of 4 and 3.7 μm, shown in figures 6.4B and 6.4C respectively, reveal that the emission peaks are split. The splitting amounts to 7 meV in figure 6.4A and 12 meV in figure 6.4C. The main mode peaks in figure 6.4C show an additional shoulder which is not resolved unfortunately. If one assumes that the splittings are due to modes of different character with the same mode number e.g. TE ,TM and HE modes (see chapter 2), the mode spacing between modes of the same character conforms to the linear dependence on reciprocal nanowire length. Further support comes from the increased splitting for the shorter nanowire. Maxwell theory for the modes of a dielectric cylinder predicts an increased splitting with decreasing cylinder dimensions (see chapter 2).

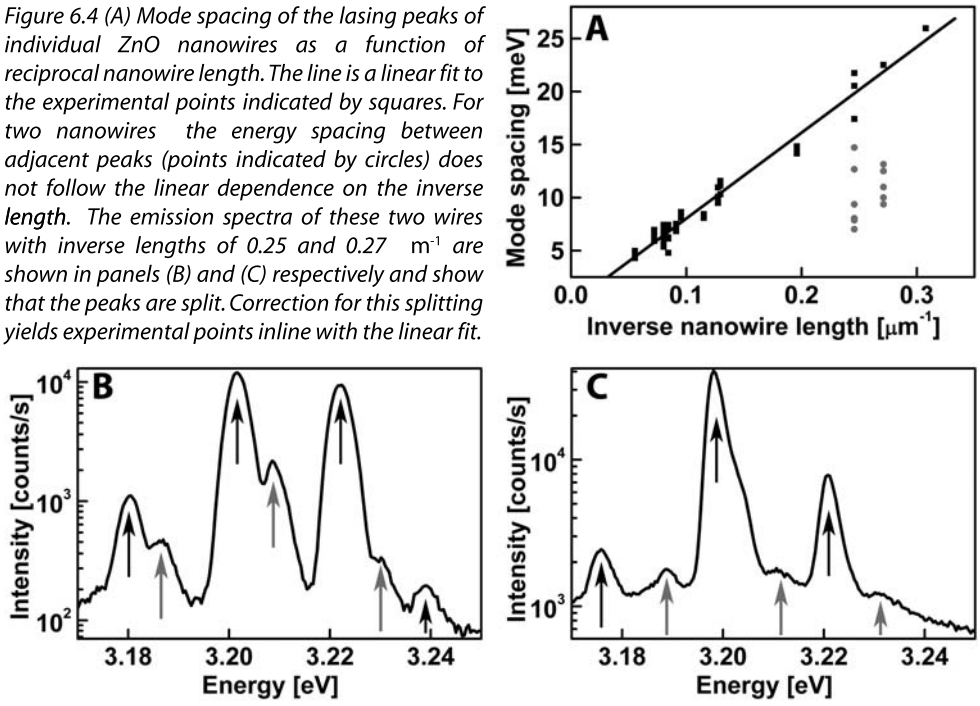

Figure 6.4 (A) Mode spacing of the lasing peaks of individual ZnO nanowires as a function of reciprocal nanowire length. The line is a linear fit to the experimental points indicated by squares. For two nanowires the energy spacing between adjacent peaks (points indicated by circles) does not follow the linear dependence on the inverse length. The emission spectra of these two wires with inverse lengths of 0.25 and 0.27 m^{-1} are shown in panels (B) and (C) respectively and show that the peaks are split. Correction for this splitting yields experimental points inline with the linear fit.

632 Observed interference patte rns from lasing ZnO nanowires

An optical dark field image of a 3.2 µm long ZnO nanowire is shown in figure 6.5A. Panchromatic photoluminescence (PL) images of the same wire under uniform illumination from the Nd:YLF laser are shown in figures 6.5B-E. The excitation power was increased stepwise from below lasing threshold until strong laser emission was observed. At an excitation intensity of 24 W/cm^2 (Fig 6.5B) the luminescence originates mainly from the body of the nanowire with only a slightly enhanced emission at the wire ends. At the lasing threshold (93 W/cm^2, Fig. 6.5C) some interference lines develop at the nanowire end facets. Figures 6.5D-E show the nanowire above the lasing threshold at excitation intensities of 139 and 268 W/cm^2 respectively. In addition to the two bright spots caused by the nanowire end facets an intricate interference pattern can be seen: rings around the end facets and lines on the body of the nanowire, oriented perpendicular to

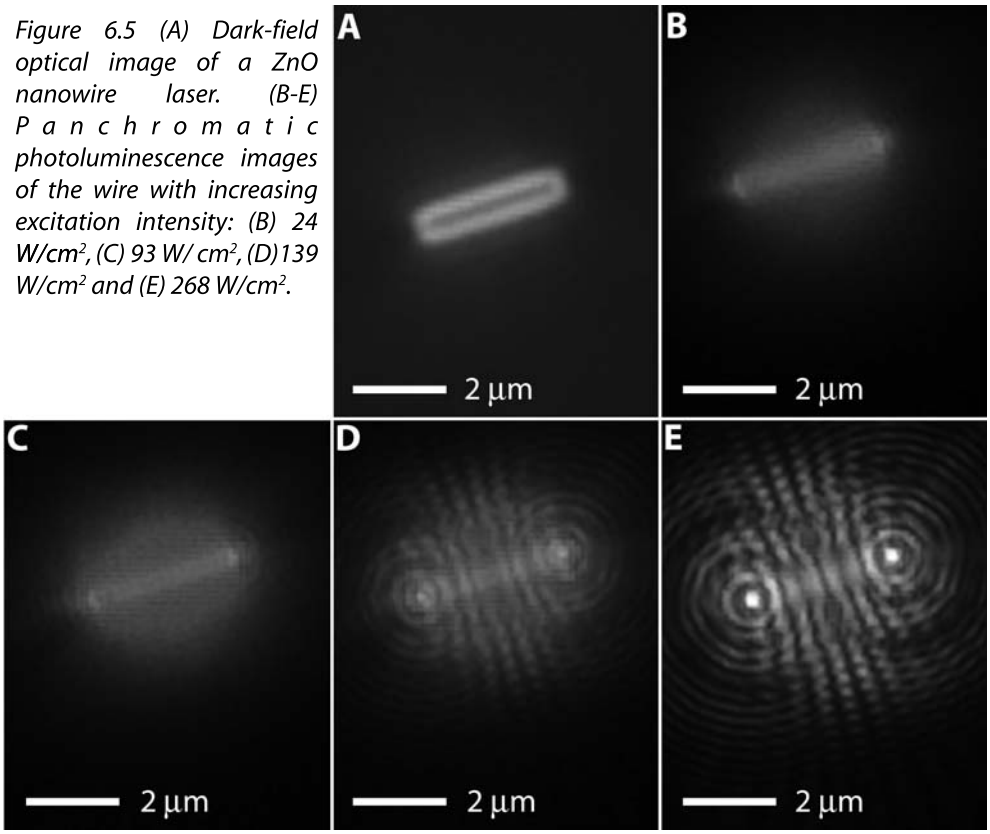

Figure 6.5 (A) Dark-field optical image of a ZnO nanowire laser. (B-E) Panchromatic photoluminescence images of the wire with increasing excitation intensity: (B) 24 W/cm^2, (C) 93 W/ cm^2, (D)139 W/cm^2 and (E) 268 W/cm^2.

the long axis. The emission spectra in figure 6.2 were taken simultaneously with the pictures of figure 6.5. All nanowires which showed the narrow emission peaks characteristic of lasing also showed the interference patterns or on the other hand, below the lasing threshold the interference pattern are never observed.

The length of the nanowire is of influence on the observed pattern. Experimental diffraction patterns of a long (10.2 μm) and a short (2.1 μm) nanowire are presented in figures 6.6A and B. The CCD image of the long nanowire shows characteristic similarities with a diffraction pattern of a round aperture generated by two distinct sources at the nanowire end facets, which are sufficiently far apart such that hardly any interference occurs. Furthermore, one can see weak luminescence from the nanowire itself due to incoherent emission. The short wire (fig. 6.4B), in contrast, shows strong interference between the two emission sources, leading to a ray-like pattern due to the formation of interference maxima and minima.

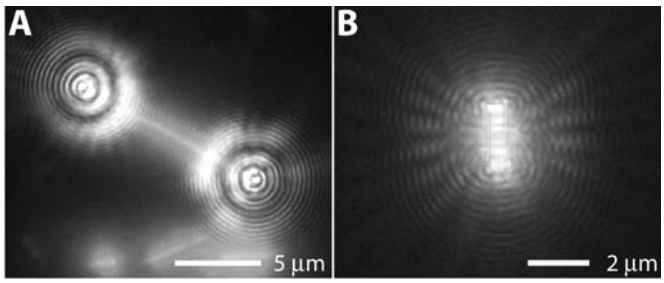

Figure 6.6 Panchromatic PL images of ZnO nanowires excited above lasing threshold. (A) A 10.2 m long nanowire showing no interference between both light sources. (B) A 2.1 m long nanowire showing strong interference between both light sources.

633 Calculated interference patterns

To investigate the directionality of the laser emission we compared the observed diffraction patterns with simulations, calculated for different angular emission profiles from the wire end facets. Figure 6.7A shows the experimental geometry with the nanowire located in the focal plane of an infinity-corrected objective in conjunction with a tube lens. Light emitted from the nanowire in the object plane is collimated by the objective and projected by the tube lens onto a CCD camera. This configuration is widely used in modern microscopes since it allows easy insertion of optical elements such as polarizers, filters, etc. into the parallel light beam between objective and tube lens without further optical corrections. The

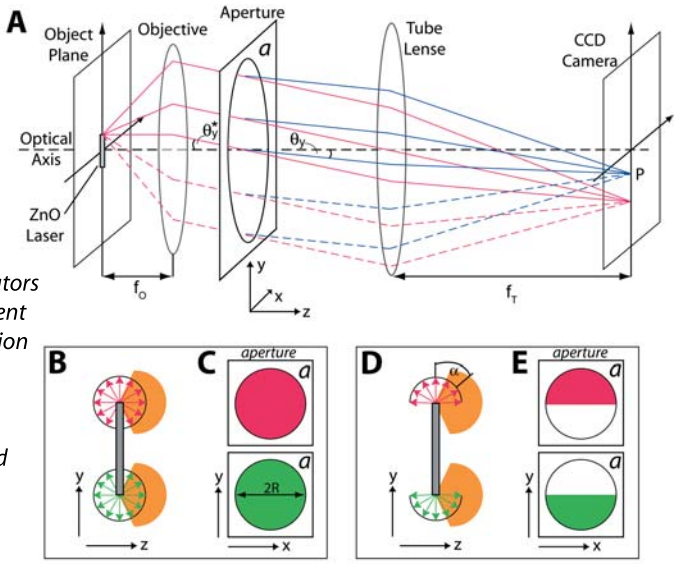

Figure 6.7 (A) Experimental configuration. For simplicity only light emission from the upper end facet is shown. Red solid lines indicate light rays for hemispherical emission while solid and dashed lines together indicate spherical emission. Blue rays show light emitted by the elementary dipole oscillators in the aperture plane in a different direction, leading to the formation of the interference pattern. (B) Schematic spherical laser emission from the upper and lower end facets, depicted as red and green arrows respectively. The orange shape indicates the collection angle of the used objective. (C) Intensity distribution in the aperture, originating from emission of the upper and lower end facets. (D) As (B) for hemispherical emission. (E) Hemispherical emission from the upper facet leads to an intensity contribution in the upper half of the aperture (depicted in red) while emission from the lower end facet gives a constant light intensity in the lower aperture half (depicted in green).

magnification M is determined by $M = f_O/f_T$, where f_O and f_T are the focal length of the objective and tube lens, respectively. Figure 6.7A shows that the beam path inside the microscope is equivalent to that of an experimental configuration to measure Fraunhofer diffraction,[19] where the diffraction pattern of an incident parallel light beam is projected onto a CCD array by the tube lens. The diffraction aperture a is defined by the width of the collimated beam between objective and tube lens. The electric field E at a point P on the CCD array is proportional to the integral of the fields originating from all elementary oscillators within the aperture area a, multiplied by their phase,

$$E_P \propto \iint_A f(x,y)\, e^{\left(-ik_0\left((l^*+l)x+(m^*+m)y\right)\right)} dxdy \qquad (1)$$

The coordinates of P are defined by $l=\sin\theta_x$ and $l=\sin\theta_y$ where θ_x and θ_y are the angles between the beam paths and the x-and y-coordinate axes, respectively. The angles of the incident parallel light beam with respect to the aperture plane are defined by $l^*=\sin\theta^*_x$ and $l^*=\sin\theta^{**}_y$. Figure 3A shows

the experimental geometry for a nanowire in the object plane, aligned parallel to the y-axis. The function *f(x,y)* describes the intensity distribution across the aperture and contains information about the direction of the laser emission from the nanowire. Figures 6.7B and D show a magnification of a nanowire lying in the focal plane of the microscope. To investigate the spatial laser emission from the wire ends we compare uniform emission in all directions (spherical emission, fig. 6.7B) with the case in which light is only emitted in the forward direction such that the intensity is constant for emission angles $|\alpha| \leq 90°$ and zero for $|\alpha| > 90°$ (hemispherical emission, fig. 6.7D). The orange background in figs. 6.7B and D indicates the light collection cone of the microscope objective, defined by its numerical aperture NA (0.9 in air), which corresponds to a collection angle of 128º. For non-directional emission we use an intensity distribution $f(x,y) = 1$ for $x^2+y^2 \leq R^2$ (with the aperture radius R) and $f(x,y) = 0$ elsewhere. Figure 6.7C shows the uniform contributions coming from the upper (red) and lower (green) end facet of the nanowire. We note that the phase factor $e^{(-ik_0(l'x+m'y))}$ is different for the emission from the top and bottom facets, thus leading to different contributions in the diffraction pattern. For a nanowire with hemispherical emission, *f(x,y)* differs not only in its phase but also in its amplitude for the emission from the top and bottom facet. The intensity distributions are shown in fig. 6.7E, which can be understood by considering the light paths shown in fig. 6.7A. For emission from the upper facet the solid rays correspond to an emission angle $|\alpha| \leq 90°$ and the dashed rays to $|\alpha| > 90°$. The difference of the diffraction integral (eq. 1) for spherical and hemispherical emission changes the interference pattern. A comparison of simulations with measured interference patterns enables us to draw conclusions about the spatial laser emission from nanowires.

Simulated patterns for non-directional (spherical) emission are shown in figure 6.8A and B. For the long wire one can see that the ring pattern around the nanowire ends is nicely reproduced in this simulation. Furthermore one can see in the simulations some weak interference between the wire ends, which is not observed in the CCD image, probably due to an insufficient sensitivity of the CCD camera. We note that the simulations do not contain incoherent luminescence so that the nanowire itself is not visible in the simulations. The calculated pattern for the short wire (fig. 6.8B) shows the same type of interference minima between the two lasing sources, which originate from a superposition of the emitted light from both ends with the same phase. Destructive interference can only

be observed if the phase difference between the two emission sources is fixed. The measured CCD image thus provides direct experimental evidence for a zero or fixed phase shift between the emission sources. Calculated diffraction patterns for hemispherical emission are shown in figures 6.8C and D. Neither the ring structure around the lasing sources (fig6.8C) nor the interference pattern (fig. 6.8D) of the measurements is reproduced correctly. Hence, the ring structure around the end facets shows that the emission is spherical. For both wires one observes a pronounced interference pattern along the wire axis, exceeding the wire length, in contrast to that found experimentally. Furthermore one can see that for the short wire the number of interference minima differ in experiment and simulation.

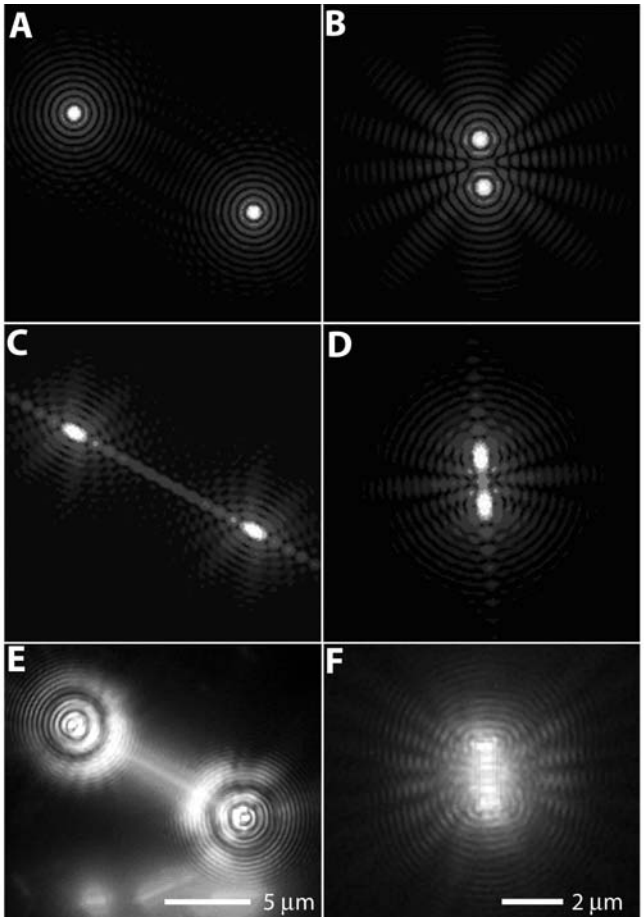

Figure 6.8 (A-B) Calculated interference patterns for spherical emission from the wire ends of a 10.2 µm long and of a 2.1 m long nanowire. (C-D) Calculated interference patterns for hemispherical emission from the wire ends of a 10.2 µm long and of a 2.1 µm long nanowire. (E-F) Experimentally observed interference patterns of a 10.2 µm long and of a 2.1 m long nanowire.

Differences between simulated and measured diffraction patterns like the observed intensity modulation in the ring patterns at the wire ends (fig. 6.6A), which are not present in the simulations (fig. 6.8A), might be caused either by beating of different emission wavelengths (the emission spectrum of this wire shows multiple lasing peaks), which was not included into the calculations, or by a non-directional emission distribution slightly different from the simplified spherical emission. For the short wire the measured interference pattern around the end facets (fig6.6B) differs
slightly from the calculated one (fig. 6.8B); this might be due to the finite wire width, which has also not been included in the simulations (emission from the end facets was approximated by point sources). The overall good agreement between experiments and simulations based on spherical emission and the disagreement with hemispherical emission brings us to the conclusion that spherical emission from ZnO nanowires in the investigated diameter range is a good approximation of the real angular distributed emission. This is in good agreement with theoretical work on the far field of lasing nanowires, which predicts that TM_{01} and TE_{01} modes can emit light in a wide angular range.[18] We furthermore mention that laser light from HE_{11} modes is predicted to be mainly emitted in the direction of the nanowire length axis, and thus might not be detectable in our experimental configuration, where the nanowire is oriented perpendicular to the optical axis of the microscope (see fig. 6.7A).

For novel applications based on nanowire lasers with sub-wavelength diameter the non-directional emission has to be taken into consideration. While this effect might be beneficial for devices such as flat panel displays, where a wide emission angle guaranties good visibility from different observation angles, it might be a drawback for nanosized photonic devices where a well-defined emission direction is required.

64 Conclusions

In conclusion we have shown that interference and diffraction from individual ZnO nanolasers has been observed. Numerical simulations show that good agreement with experiments can be achieved only if non-directional emission from the end facets is assumed in addition to a zero or fixed phase difference at the end facets. Furthermore we have demonstrated that the energy spacing between the main lasing peaks corresponds well to longitudinal Fabry-Pérot modes.

References

[1] M. Law, D. J. Sirbuly, J. C. Johnson, J. Goldberger, R. J. Saykally, and P. Yang, Nanoribbon waveguides for subwavelength photonics integration, *Science* **305** (2004), p. 1269.

[2] A. Pan, R. Liu, Q. Yang, Y. Zhu, G. Yang, B. Zou, and K. Chen, Stimulated emissions in aligned CdS nanowires at room temperature, *J. Phys. Chem. B* **109** (2005), p. 24268.

[3] L. Tong, R. R. Gattass, J. B. Ashcom, S. He, J. Lou, M. Shen, I. Maxwell, and E. Mazur, Subwavelength-diameter silica wires for low-loss optical wave guiding, *Nature* **426** (2003), p. 816.

[4] S. Gradecak, F. Qian, Y. Li, H.-G. Park, and C. M. Lieber, GaN nanowire lasers with low lasing thresholds, *Applied Physics Letters* **87** (2005), p. 173111.

[5] M. H. Huang, S. Mao, H. Feick, H. Yan, Y. Wu, H. Kind, E. Weber, R. Russo, and P. Yang, Room-temperature ultraviolet nanowire nanolasers, *Science* **292** (2001), p. 1897.

[6] R. Agarwal, C. J. Barrelet, and C. M. Lieber, Lasing in single cadmium sulfide nanowire optical cavities, *Nano Letters* **5** (2005), p. 917.

[7] J. X. Ding, J. A. Zapien, W. W. Chen, Y. Lifshitz, S. T. Lee, and X. M. Meng, Lasing in ZnS nanowires grown on anodic aluminum oxide templates, *Appl. Phys. Lett.* **85** (2004), p. 2361.

[8] A. H. Chin, S. Vaddiraju, A. V. Maslov, C. Z. Ning, M. K. Sunkara, and M. Meyyappan, Near-infrared semiconductor subwavelength-wire lasers, *Applied Physics Letters* **88** (2006), p. 163115.

[9] X. Duan, Y. Huang, R. Agarwal, and C. M. Lieber, Single-nanowire electrically driven lasers, *Nature* **421** (2003), p. 241.

[10] J. C. Johnson, H. Yan, P. Yang, and R. J. Saykally, Optical cavity effects in ZnO nanowire lasers and waveguides, *J. Phys. Chem. B* **107** (2003), p. 8816.

[11] H. Pettersson, J. Trägardh, A. I. Persson, L. Landin, D. Hessman, and L. Samuelson, Infrared photodetectors in heterostructure nanowires, *Nano Letters* **6** (2006), p. 229.

[12] Y. Huang, X. Duan, and C. M. Lieber, Nanowires for integrated multicolor nanophotonics, *Small* **1** (2005), p. 142.

[13] M. Bayer, A. Forchel, T. L. Reinecke, P. A. Knipp, and S. Rudin, Confinement of light in microresonators for controlling light-matter interaction, *phys. stat. sol. (a)* **191** (2002), p. 3.

[14] D. Wang, H. W. Seo, C.-C. Tin, M. J. Bozack, J. R. Williams, M. Park, and Y. Tzeng, Lasing in whispering gallery mode in ZnO nanonails, *J. Appl. Phys.* **99** (2006), p. 093112.

[15] T. Nobis, M. Kaidashev, A. Rahm, M. Lorenz, and M. Grundmann, Whispering gallery modes in nanosized dielectric resonators with hexagonal cross section, *Phys. Rev. Letters* **93** (2004), p. 103903-1.

[16] R. Hauschild, H. Lange, H. Priller, C. Klingshirn, R. Kling, A. Waag, H. J. Fan, M. Zacharias, and H. Kalt, Stimulated emission from ZnO nanorods, *phys. stat. sol. (b)* **243** (2006), p. 853.

[17] A. V. Maslov, M. I. Bakunov, and C. Z. Ning, Distribution of optical emission between guided modes and free space in a semiconductor nanowire, *J. Appl. Phys.* **99** (2006), p. 024314.

[18] A. V. Maslov and C. Z. Ning, Far-field emission of a semiconductor nanowire laser, *Optics Letters* **29** (2004), p. 572.

[19] M. Born, *Optik* (Springer-Verlag, Berlin, 1933).

[20] M. H. Huang, Y. Wu, H. Feick, N. Tran, E. Weber, and P. Yang, Catalytic growth of zinc oxide nanowires by vapor transport, *Adv. Materials* **13** (2001), p. 113.

Samenvatting

Nanodraden gemaakt van halfgeleider materialen zoals InP en ZnO, met een diameter kleiner dan 500 nm (1 nm is een miljardste meter) en een lengte tot 100 μm (1 μm is een miljoenste meter) kunnen beschouwd worden als veelbelovende bouwstenen voor toekomstige geminiaturiseerde opto-elektrische circuits. Aangezien de schakelelementen (transistoren) in de huidige "chips" met gebruikmaking van de gevestigde productietechnieken nog behoorlijk verkleind kunnen worden (misschien wel tot fysische limieten bereikt worden) is het echter onwaarschijnlijk dat nanodraad circuits de transistoren in silicium chips zullen vervangen. Bij toepassingen van halfgeleidende nanodraden moet daarom eerder gedacht worden aan (bio)chemische detectie, lichtgeleiding op een schaal kleiner dan de golflengte van het licht of nieuwe concepten van berekening (kwantum rekenen, spintronica).

Halfgeleidende nanodraden worden over het algemeen gesynthetiseerd door middel van een damp-vloeistof-vaste stof reactie. Hierbij wordt gebruik gemaakt van kleine metaaldruppels die halfgeleider damp opnemen tot ze (over)verzadigd zijn waarna er zich vast halfgeleider materiaal afzet. Omdat het energetisch ongunstig is om een tweede vloeistof/vaste stof grens te vormen zal het vaste halfgeleider materiaal zich bij voorkeur aan de bestaande vloeistof/vaste stof grens afzetten zodat het gevormde halfgeleider materiaal de vorm van een draad aanneemt. Het bewijs voor dit mechanisme werd geleverd doordat de metaal deeltjes na de groei aan een uiteinde van de draad terug worden gevonden en de diameter van de nanodraad grotendeels bepaald wordt door de diameter van dit metalen deeltje.

In hoofdstuk drie van dit proefschrift wordt de synthese van eenkristallijne nanodraden van InP (indiumphosphide) en ZnO (zinkoxide) beschreven. Bij de synthese van InP nanodraden (uitgevoerd bij Philips Research, Eindhoven) wordt gebruik gemaakt van laserablatie van geperst halfgeleider poeder als de dampbron. De InP nanodraden, gevormd op siliciumoxide substraten, zijn willekeurig georiënteerd, bezitten een gouddeeltje aan het uiteinde en hebben gemiddeld een diameter van 50 nm bij een lengte van 10 μm. De dampbron bij de synthese van ZnO nanodraden wordt gevormd door de reductie van ZnO poeder door koolstofpoeder bij temperaturen boven 850°C. De gevormde draden hebben de éénkristallijne wurtziet kristalstructuur met een hexagonale

dwarsdoorsnede en met de lengte-as van de draad samenvallend met de c-as van de kristalstruktuur. Indien gebruik wordt gemaakt van siliciumoxide substraten voorzien van een dun laagje goud zijn de draden willekeurig georiënteerd, bezitten ze een gouddeeltje aan het uiteinde en hebben ze een diameter van 50-100 nm bij een lengte tot 50 μm. Wanneer echter gebruik wordt gemaakt van éénkristallijne aluminiumoxide substraten (saffier) voorzien van een dun goudlaagje zijn de gegroeide draden loodrecht op het substraat georiënteerd met de richting van de hexagonale zijfacetten in drie oriëntaties. Dit geeft aan dat de draden kristalrooster aansluitend zijn gegroeid met het c-vlak van het ZnO kristalrooster parallel aan het saffier a-vlak. De draden hebben een lengte van 10 μm en een diameter van 100 tot 300 nm. Opvallend is dat er geen gouddeeltjes aan de draaduiteinden worden gevonden en dat er op plekken waar geen goud was afgezet ook geen draden gegroeid zijn. Dit duidt erop dat deze draden niet via het damp-vloeistof-vaste stof mechanisme zijn gegroeid maar dat de gouddeeltjes wel een katalytische werking hebben.

Als laatste wordt in dit hoofdstuk beschreven hoe de ZnO nanodraden kunnen worden gedoteerd met kobalt ionen wat kan resulteren in halfgeleidende ferromagnetische nanodraden bij kamertemperatuur. Na de gebruikelijke ZnO nanodraad synthese worden de draden ondergedompeld in een kobaltacetaat oplossing en vervolgens gedroogd. Uit metingen blijkt dat na deze procedure het kobalt als een schil om de draad heen zit en dat pas na verwarmen tot 900°C het kobalt homogeen door de draad heen verdeeld is. Uit optische metingen blijkt dat zink ionen gesubstitueerd zijn door kobalt ionen. De gevolgde methode maakt gebruik van de grote oppervlak-tot-inhoud verhouding van de nanodraden en kan in principe ook voor andere nanostructuren, andere halfgeleiders en andere substitutieatomen gebruikt worden.

Door de al eerder genoemde relatief grote oppervlak-tot-inhoud verhouding worden de eigenschappen van nanodraden in hoge mate bepaald door de elektronische structuur van het oppervlak. Dit maakt de nanodraden gevoelig voor hun omgeving wat een voordeel kan zijn in bijvoorbeeld toepassingen als sensor; het kan echter ook nadelig zijn voor toepassingen waarin er in de draad licht wordt opgewekt of getransporteerd. InP nanodraden oxideren snel aan de lucht en hebben daardoor een lage photoluminescentie efficiëntie (belangrijk voor toepassing in licht emitterende diodes), die ook sterk van draad tot draad kan variëren. In hoofdstuk vier wordt beschreven hoe de photoluminescentie efficiëntie van éénkristallijne InP nanodraden kan

worden verhoogd door middel van door licht gestimuleerd nat-chemisch etsen in butanol oplossingen van waterstof fluoride en het indium bindende ligand *tri-octyl-fosfineoxide (TOPO)*. Licht absorptie door de nanodraad in voornoemde oplossingen blijkt cruciaal te zijn om een verhoogde fotoluminescentie efficiency te realiseren. Efficiency verbeteringen tot wel drie ordes van grootte zijn gemeten hoewel het resultaat sterk van draad tot draad verschilt. Tijdsopgeloste metingen aan de gepassiveerde draden met verhoogde luminescentie efficiency laten sterke fluctuaties van de emissie-intensiteit zien. Deze resultaten weerspiegelen de sterke invloed van een of enkele niet-radiatieve recombinatie centra op de luminescentie eigenschappen van de hele nanodraad.

Hoofdstuk vijf laat zien dat de optische eigenschappen van ZnO nanodraden gedomineerd worden door een uitzonderlijk sterke licht-materie koppeling. Door met een laser- of electronenbundel de nanodraad plaatsopgelost aan te slaan en voor elke positie van deze bundel het emissie spectrum te analyseren wordt duidelijk, dat voor bepaalde emissie-energieën de draad het beste aan de uiteinden kan worden aangeslagen terwijl voor andere emissie-energieën een homogeen excitatie profiel gevonden wordt. Door voor elke emissie energie de verhouding tussen de hoeveelheid licht, die verkregen wordt bij excitatie aan het uiteinde van de draad, en de hoeveelheid licht, die verkregen wordt bij excitatie in het midden van de draad, uit te zetten wordt een zogenaamd verhogings spectrum verkregen. Dit spectrum laat twee pieken zien aan weerszijden van de elektron-gat paar (exciton) energie en kan gerelateerd worden aan de energie-golfvector dispersierelatie van drie dimensionaal opgesloten licht-materie composietdeeltjes met een record koppelingssterkte van 160 meV (afhankelijk van de draad). Deze sterke koppeling zorgt ervoor dat "licht" in de nanodraad beschouwd moet worden als composiet deeltjes (exciton-polaritonen) met deels foton eigenschappen en deels exciton eigenschappen. Dit heeft als gevolg dat de golflengte van "licht' in de nanodraad radicaal anders kan zijn dan in een materiaal zonder excitonen of dat de brekingsindex uitzonderlijk hoog kan worden. Met deze bevindingen zal rekening moeten worden gehouden bij toekomstige nanophotonische circuits.

Tenslotte wordt in hoofdstuk zes aangetoond dat de ZnO nanodraden bij hoge excitatie intensiteit laserlicht in het UV energie gebied uitzenden. Bij toenemende excitatie intensiteit worden in het emissie spectrum van een enkele draad enkele zeer smalle pieken geobserveerd met een onderlinge afstand die lineair met de inverse nanodraad lengte

toeneemt. Dit laat zien dat de nanodraad als een optische resonator fungeert waarbij de pieken veroorzaakt worden door longitudinale Fabry-Pérot modes. Tegelijk met het verschijnen van de smalle pieken in het emissiespectrum wordt ook een opmerkelijk interferentie patroon in de afbeelding van de nanodraad emissie geobserveerd. Uit de vergelijking van dit patroon met numerieke simulaties blijkt dat het patroon veroorzaakt wordt door licht dat met een vast of afwezig faseverschil aan beide uiteinden van de nanodraad wordt uitgezonden. Bovendien blijkt dat het licht aan deze uiteinden sferisch wordt uitgezonden en niet in een gerichte bundel zoals bij lasers gebruikelijk is. Dit wordt veroorzaakt doordat de diameter van de draad kleiner is dan de golflengte van het uitgezonden licht in lucht, waardoor het licht bij het verlaten van de draad-uiteinden in alle richtingen gebroken wordt.

Publications and presentations

Publications related to this thesis

- Lambert K. van Vugt, Sandra J. Veen, Erik P. A. M. Bakkers, Aarnoud L. Roest and Daniël Vanmaekelbergh, Increase of the photoluminescence intensity of InP nanowires by photo-assisted surface passivation, *Journal of the American Chemical Society* **127** (2005), p. 12357. Chapter 4.

- Prasanth Ravindran, Lambert K. van Vugt, Daniël Vanmaekelbergh and Hans C. Gerritsen, Resonance enhancement of optical second harmonic generation in a ZnO nanowire, *Applied Physics Letters* **88** (2006), p. 181501. Chapter 5.

- Lambert K. van Vugt, Sven Rühle, Prasanth Ravindran, Hans C. Gerritsen, Laurens Kuipers and Daniel Vanmaekelbergh, Exciton polaritons confined in a ZnO nanowire cavity, *Physical Review Letters* **97** (2006), p. 147401. Chapter 5.

- Lambert K. van Vugt, Sven Rühle, and Daniël Vanmaekelbergh, Phase-Correlated Nondirectional Laser Emission from the End Facets of a ZnO Nanowire**,** *Nano Letters* **6** (2006), p. 2707. Chapter 6.

- Lambert K. van Vugt et al. Cobalt doped ZnO nanowires, manuscript in preparation. Chapter 3.

- Sven Rühle, Lambert K. van Vugt, Laurens Kuipers and Daniël Vanmaekelbergh, Room-Temperature Polariton Lasing from a ZnO Nanowire, Manuscript in preparation. Chapters 5&6.

- Lambert K. van Vugt, Sven Rühle, and Daniël Vanmaekelbergh, Frontlinie: Versterkte licht-materie-interactie in een ZnO-nanodraadresonator, *Nederlands Tijdschrift voor Natuurkunde* **72**(12) (2006), p. 398. Chapter 5.

- Stephan J. M. Zevenhuizen, Lambert K. van Vugt, Dennis H. van Dorp and Daniël Vanmaekelbergh, Ingelijst: Draadnagels, *Nederlands Tijdschrift voor Natuurkunde* **73**(1) (2007), p. 25. Chapter 3.

- Lambert K. van Vugt, Sven Rühle and Daniël Vanmaekelbergh, Ingelijst: Laserdraad, *Nederlands Tijdschrift voor Natuurkunde* **74**(2), p.59. Chapter 6.

Other publication

- Lambert K. van Vugt, A. Floris van Driel, R. Willem Tjerkstra, Lydia Bechger, Willem L. Vos, Daniël Vanmaekelbergh and John J. Kelly, Macroporous germanium by electrochemical deposition, *Chemical Communications* **18** (2002), p. 2054.

Oral presentations

- Photo etching and photoluminescence of single InP nanowires, *Joint meeting of the CW study sections Kristal- en Struktuuronderzoek and Chemie van de Vaste Stof en Materiaalkunde*, Lunteren, March 2004.

- Do exciton-polaritons determine the optical properties of ZnO nanowires ?, *Photon Physics in The Netherlands: Celebrating the 100th Anniversary of the Photon*, Amsterdam, June 2005.

- Exciton-Polaritons Confined in a ZnO nanowire Cavity, *Materials Research Society Fall 2005 meeting*, Boston, November 2005.

- Phase Correlated non-directional laser emission from ZnO nanowires, *Materials Research Society Spring 2007 meeting*, San Francisco, April 2007.

- Strong Light-Matter interaction and lasing in semiconductor nanowires, *Materials Research Society Spring 2007 meeting*, San Francisco, April 2007.

Dankwoord

Het doen van een promotieonderzoek heet een solitaire bezigheid te zijn. Desondanks hebben vele mensen direct of indirect bijgedragen aan de totstandkoming van dit proefschrift en op deze plek wil ik deze mensen daarvoor hartelijk bedanken.

Allereerst wil ik mijn promotor, Daniël Vanmaekelbergh, bedanken voor de begeleiding gedurende de afgelopen jaren. Daniël, je enthousiasme, gedrevenheid en scherpheid zijn een bron van inspiratie geweest. Ik ben je ook erkentelijk voor het vertrouwen dat je in me hebt gesteld en de ruimte die je me hebt geboden om interessante wetenschappelijke richtingen in te slaan. Halfway through my research, the nanowire team was doubled in strength by the addition of Sven Rühle as post-doctoral researcher. Sven, it was not only really great working and discussing with you, also drinking a beer after working hours was thoroughly enjoyable. I think the sum of our collaboration was bigger than the parts and I wish you and Hannah all the best with your new "project".

Ik heb gedurende het onderzoek ook veel samengewerkt met enthousiaste wetenschappers in andere groepen in Nederland. Erik, bedankt voor de InP nanodraden die je bij Philips Research voor mij gemaakt hebt. Ook heb je ervoor gezorgd dat ik een deel van mijn onderzoek in Eindhoven kon doen en er was daarbij nooit een gebrek aan draden en ideeën. Aarnoud en Marcel bedankt voor het groeien en karakteriseren van InP nanodraden in de door mij gefabriceerde mallen. Tevens wil ik Margit en Cees Claassen hartelijk danken voor de gastvrijheid tijdens de overnachtingen in Eindhoven.

De experimenten met de twee-foton microscoop zoals beschreven in hoofdstuk vijf zijn gedaan in samenwerking met de molekulaire biofysica groep van Hans Gerritsen. I would like to thank Jonathan Palero for the extensive "introduction" to the microscope system and Prasanth Ravindran and Hans Gerritsen for the fruitful collaboration on these experiments. Dankzij Hans Meeldijk was de urendurende karakterisatie van de ZnO draden met de hoge resolutie elektronenmicroscoop een aangename bezigheid. Daarnaast, wil ik Kobus Kuipers bedanken voor de discussies over de ZnO polariton resultaten en de hulp bij het schrijven van de artikelen. Timon van Wijngaarden wil ik bedanken voor de eerste proefmetingen met de cathodo-luminescentie opstelling in het Amolf. Astrid van der Horst, Andrew Campbell en Dirk Vossen wil ik bedanken voor de experimenten met de optische pincet.

In ons eigen lab heb ik kunnen rekenen op technische hulp en het goede humeur van Hans Ligthart. Hans, vaak kwam ik bij je langs met een vaag idee voor een cel, adapter of verbindingsstuk en jij wist dat snel en vakkundig (met hulp van de werkplaats) om te zetten in iets dat vaak al gisteren klaar was. Bedankt daarvoor! Stephan Zevenhuizen bedankt voor alle uren die je besteed hebt aan het schieten van elektronenmicroscoopplaatjes van de "monsters". Ook je hulp bij het maken van programma's voor de verwerking van de data en het programmeren van het scan platform van de microscoop stelde ik zeer op prijs. Nico Kuipers, Jan van Eijk, en Johan Keijzer wil ik bedanken voor het verzorgen van de gassen en cryogene vloeistoffen en dankzij het precieze polijstwerk van Peter de Graaf kon ik prachtige mallen maken voor de groei van geordende nanodraden.

Verder ben ik de studenten die ik heb mogen begeleiden dankbaar voor hun bijdragen aan dit proefschrift: Dennis, Sandra, Ilse, Arash en Ruben, bedankt voor jullie inzet. De resultaten van jullie werk vinden jullie verspreid door dit proefschrift.

De overige hoogleraren in onze vakgroep, John Kelly, Andries Meijerink, Cees Ronda en Jan van der Eerden alsook Harold de Wijn wil ik bedanken voor de kennis en wijsheid die ze zowel tijdens als na mijn studie scheikunde gedurende colleges en discussies tentoon hebben gespreid.

Er zijn vele andere mensen in de vakgroep die mijn promotietijd tot een aangename tijd hebben gemaakt. Peter, I enjoyed your sense of humor as well as playing numerous frames of snooker. It was nice traveling with you to my first international conference Ik heb het langst met Harold op één kamer gewerkt. Het was fijn zo'n no-nonsense kamergenoot te hebben die een ironische opmerking mijnerzijds op zijn waarde wist te schatten. Ook mijn andere kamergenoten Marcel, Freek, Jeroen, Dennis, Philipp en René wil ik bedanken voor de prettige sfeer op kamer 168. Op het lab lopen en liepen nog vele karakters rond die je om hulp kon vragen, waar je een potje tafelvoetbal mee kon spelen of een biertje mee kon drinken. Arjan, Rianne, Shuai, Zeger, Alexander, Aarnoud, Linda, Bryan, Thijs, Celso, Jessica, Karin, Peter, Floris, Fiona, Aneliya, Rolf, Sander, François, Laura, Jan, Bob, Stephan, Niek, Ingmar, Volker, Vladimir en Heng-Yu, bedankt.

Het nodige tegenwicht aan alle wetenschappelijke mijmeringen boden ook mijn vrienden en mijn zus. Cobi, het is inspirerend om te zien hoe jij aan jouw weg timmert. Ik eindig dit dankwoord met degenen waarmee het ook allemaal begonnen is, mijn ouders. Met hun steun en vertrouwen hebben ze de basis gelegd waardoor ik me kunnen ontwikkelen tot wie ik ben.

Curriculum Vitae

Lambert Karel van Vugt was born on September 6th 1977 in Utrecht, The Netherlands. In June 1995 he obtained his VWO diploma at the "Niels Stensen College" in Utrecht. In September 1995 he started his study in chemistry at the University of Utrecht resulting in his Master of Science degree in August 2001 ("met genoegen"). His MSc. project was conducted in the condensed matter group under the supervision of Prof. Dr. J. J. Kelly. This project resulted in a publication describing the non-aqueous electrochemical deposition of germanium air-sphere crystals for photonic applications. After graduating in September 2001, he worked as a research assistant on a project which aimed to increase the switching speed of metal hydride mirrors by electrodeposition of palladium hydrogen diffusion channels.

From July 2002 onwards he was employed as a PhD student by the Dutch Foundation for Fundamental Research on Matter (FOM) and performed research in the Condensed Matter and Interfaces group of the Debye Institute at the University of Utrecht under the supervision of Prof. Dr. D. Vanmaekelbergh. Most of the results of this research are described in this thesis, were published in scientific journals and were presented at international conferences.

During this time he also supervised two Master students, one Bachelor student and two students performing research placements at a Master level. Educational tasks further entailed the assistance of first year students during their "exploration in the groups" practical courses as well as assisting second year students during their "measurements in physical chemistry" practical courses. Apart from his research and educational tasks he also took part in a "goal oriented working and planning" course as well as a business orientation course at Nyenrode University.